ELECTRO-OSMOTIC PUMPING AND IONIC CONDUCTANCE MEASUREMENTS IN POROUS MEMBRANES

By

Saumitra K. Vajandar

Dissertation

Submitted to the Faculty of the

Graduate School of Vanderbilt University

in partial fulfillment of the requirements

for the degree of

DOCTOR OF PHILOSOPHY

in

Interdisciplinary Materials Science

December, 2009

Nashville, Tennessee

Approved:

Professor Deyu Li

Professor William Hofmeister

Professor Weng Poo Kang

Professor Haoxiang Luo

Professor Greg Walker

To my beloved parents,

Dr. K. S. Vajandar and Mrs. G. K. Vajandar

ACKNOWLEDGEMENTS

I would firstly like to express my deepest gratitude and appreciation to my advisor Prof. Deyu Li for the continuous support and invaluable guidance he has provided me, not only during the course of my Ph.D. but also in my personal life. Our paths crossed way back in 2004, which was the genesis of a long journey, at the culmination of which I feel extremely honored and fortunate to have completed my Ph.D. dissertation under his supervision. He has, in many ways, led by example on how to approach and solve problems encountered in research. His strong understanding and proficiency in science and technical concepts has helped me resolve many issues related to my research work. Over these past five years, he has been an excellent mentor to me, but above all a great friend. I owe him a lot for all the knowledge and encouragement he has showered on me at an important stage of my career.

My earnest thanks to Prof. William Hofmeister of The University of Tennessee Space Institute for all the technical discussions and valuable inputs that he has provided me over the years related to my doctoral research. His in-depth knowledge of materials science and his ability to resolve fundamental research related conundrums from a practical standpoint has immensely helped me with my research all throughout my Ph.D. work. It was he who introduced me to Prof. Deyu Li and if not for him, this work would not have reached its fruition at all.

I would like to take this opportunity to thank Prof. Kevin Martin, Prof. Greg Book, Gary Spinner and Tran-Vinh Nguyen of the Georgia Institute of Technology for

permitting me to use their cleanroom facility to carry out my microfabrication work. I am deeply indebted to Gary Spinner and Tran-Vinh Nguyen for the numerous discussions that I have had with them on issues pertaining to microfabrication. Without them it would have been hard to realize the completion of this thesis work.

I would like to mention my utmost thanks to Prof. William Hofmeister, Prof. Weng Poo Kang, Prof. Haoxiang Luo, and Prof. Greg Walker for serving on my committee. I am greatly honored to have them as my committee members. Dr. Weng Poo Kang and Dr. Sharon Weiss are worthy of special thanks for being generous in letting me use their laboratory and cleanroom facility to conduct my research.

I would also like to thank Prof. John Wikswo and the Vanderbilt Institute for Integrative Biosystems Research and Education (VIIBRE) for providing me the necessary funding and his laboratory facility during the initial phase of my research. My wholehearted thanks to Dr. Dmitry Markov for all those technical discussions that I have had with him over the years. They have played a big role in putting this thesis together.

My sincere thanks to the graduate secretary of Materials Science program, Mrs. Sarah Ross for all the assistance provided to me right from my first day at Vanderbilt. My heartfelt thanks to my friends Sameer Mahajan, Dr. Sriram Dixit, Dr. Karthik Subramanian and Dr. Anupama Karthik for their never-ending friendship and involvement in research related discussions during the course of my Ph.D. They have been a family to me at Vanderbilt in the absence of my parents.

I wish to express my thankfulness to the group members, Dr. Dongyan Xu, Dr. Juekuan Yang, Jiashu Sun, Yang Yang, Dr. Yandong Gao, and Scott Waltermire with

whom I have shared these wonderful years during my graduate school career. Their association and involvement in useful discussions pertaining to my research work has always been a fruitful experience. My heartfelt gratitude goes to Dr. Dongyan Xu, Dr. Juekuan Yang and Jiashu Sun for always being there to help me out in any research related matter and for having the patience to bear with my trivial and mindless questions.

I thank Prof. Anthony Hmelo, Dr. Robert Geil, Dr. Bo Choi, and the Vanderbilt Institute of Nanoscale Science and Engineering (VINSE) for offering assistance involving microfabrication and other technical issues. My acknowledgments also go to Robin Midgett, the technical assistant and Myrtle Daniels, Jean Miller, and Suzanne Weiss, the administrative assistants at the Mechanical Engineering department, for all their help in terms of technical matters and procurement of lab supplies required for this research.

I will forever be indebted to my friends Dr. Amit Palkar, Hemangi Palkar, Dr. Ashwin Rao, Dr. Vaishali Ukirde, Sonam Shah, Dr. Sachin Bet, Sangram Kadam, Pravahan Salunkhe, Dr. Harsha Kulkarni, Chrysler Murray, Anil Tripathi, Anitha Vijay, Nikkon Ghosh, Supil Raina, Jadav Das, Deepti Thopte, Farah El-Mamouni, Rajan Arora, Chetan Kulkarni, Milind Shashtri, my closest cousin, Sooraj Arur, and others, who have contributed in their own unique ways during this period and always.

Finally, I would like to thank the two wonderful people, my parents Dr. K. S. Vajandar and Mrs. G. K. Vajandar, who brought me into this world. They have instilled an importance of education in me right from a very young age and have positively encouraged me during the highs and lows of my educational career. They have devoted themselves at every possible stage in my life so far to ensure that I do not compromise on

my education, for which I cannot thank them enough. Without them, I would not have been able to see this day of my thesis completion. I will forever be grateful to my sister, Sonal Lagad for her love, untiring support, and seemingly unlimited belief in me during my Ph.D. work. I also owe a lot to my brother-in-law, Vick Lagad, for having me over at his place in Atlanta during my time spent at Georgia Institute of Technology. He would always be present at the apartment complex gate to let me in with a smile, no matter how late in the night I would return from the cleanroom.

This acknowledgement would be incomplete without offering heartfelt gratitude to Vanderbilt University for giving me this opportunity to complete my graduate studies and to mother Nature for creating infinite avenues to continuously explore, learn, and contribute to the development of science and technology, and in effect, life on this fascinating planet.

TABLE OF CONTENTS

LIST OF FIGURES

LIST OF TABLES

ABSTRACT

Electro-osmotic (EO) pumps directly convert electrical energy into fluids' kinetic energy, which have many advantages such as a simple and compact structure, no mechanical moving parts, and easy integration. In general, it is easy for EO pumps to generate enough pressure but it has been a challenge for EO pumps to produce a high flowrate. EO pumps have found applications in various micro-/nano-electro-mechanical systems (MEMS/NEMS) and have the potential to impact a variety of engineering fields including microelectronics cooling and bio-analytical systems. This dissertation focuses on the design, fabrication and characterization of EO pumps based on two novel porous membrane materials: SiO_2-coated anodic porous alumina and SiN_x-coated porous silicon.

High quality porous alumina membranes of controllable pore diameters in the range of 30-100 nm and pore lengths of 60-100 μm were fabricated by electrochemical anodization. The pores are straight, uniform and hexagonally close-packed with a high porosity of up to 50%. The inner surface of the pore was coated with a thin layer (~5 nm) of SiO_2 conformally to achieve a high zeta potential. The EO pumping flowrate of the fabricated anodic alumina membranes, coated and uncoated, was experimentally measured. Results indicate that the high zeta potential of the SiO_2 coating increases the pumping flowrate even though the coating reduces the porosity of the membrane. The nanostructured SiO_2-coated porous anodic alumina membranes can provide a normalized flowrate of 0.125 ml/min/V/cm^2 under a low effective applied voltage of 3 V, which sets a record high normalized flowrate under low applied voltage.

To realize field effect control of EO pumping, we designed and fabricated SiN_x-coated porous silicon membranes with the silicon core as the electrode to apply a transverse gate potential. The gate potential will modulate the zeta potential of the pore wall and thereby provide control over the EO flowrate. The membranes were fabricated out of heavily doped silicon wafers using microfabrication techniques. The pores have a 15 μm × 40 μm cross sectional area with a thin layer of SiN_x coated conformally over the pores by low-pressure chemical vapor deposition (LPCVD). The range of gate voltages applied was from -45 V to +40 V. For $V_g < 0$, current leakage through the SiN_x film was observed whereas negligible leaking current was detected for $V_g > 0$. This current rectification effect is known as electrolytic rectification, as a result of which a greater EO flow control, nearly 70% reduction in flow velocity, was observed for positive gate bias and 15% flow velocity enhancement under negative gate bias of similar magnitude.

Ionic current is closely related to EO flow and the last part of the dissertation is devoted to ionic current measurements through commercially made nanoporous glass membranes (4 nm average pore diameter). This study was motivated by a molecular dynamics (MD) simulation highlighting an unusual ionic current trend in a 3 nm diameter pore having high surface charge density at high electrolyte concentrations. The ionic current was measured with two kinds of electrolytes – NaCl and KCl. The experimental results, however, indicated an expected linear trend of ionic current for electrolyte concentrations beyond 1 M, contrary to the results of the MD simulation study, which was attributed to a low surface charge density measured for the porous glass membranes.

CHAPTER I

INTRODUCTION

1.1 Electro-Osmosis

When an electric field is applied to a heterogeneous system consisting of a solid body (an insulator) in contact with an electrolyte solution, a solution flow known as *electro-osmosis* could be developed. The solid is most commonly a capillary porous body, while the electrolyte solution is an aqueous medium. This phenomenon attracted the attention of scientists long ago and was first demonstrated by F. F. Reuss at the beginning of the 19th century (Reuss 1809) wherein he showed through experiments that under the influence of an applied electric field water migrated through porous clay diaphragms toward the cathode. This, he reported, was a consequence of the fact that clay, sand and other minerals carry negative surface charges when in contact with water; the water containing some dissociated salt. The charged surface attracts the positive ions (counter-ions) in the water and repels the negative ions (co-ions). The counter-ions therefore accumulate within an electrical double layer (EDL) sheath next to the charged surface, and under the application of an electric field result in a net migration of ions in the double layer toward the cathode (figure 1.1). Due to viscous drag, the water within the pores is pulled by the moving double layer ions thus generating a flow through the porous medium.

However, notwithstanding the unusual nature of this phenomenon, electro-osmosis remained only an interesting scientific curiosity till the middle of the 19th cent-

ury. Scientific works raising the question of the causes of this phenomenon appeared only in the mid 1860s. Quincke observed electro-osmosis with glass capillaries and studied the phenomenon more systematically for a variety of materials and reported quantitative measurements (Quincke 1861). Helmholtz adopted his idea and proposed the double layer theory, which related the electrical and flow parameters for electrokinetic transport (Helmholtz 1879). He was the first to derive equations for electro-osmosis. In deriving the relevant expression, he assumed the pore to be a uniform capillary. He did not include the dielectric permittivity term in the equation. Smoluchowski used Helmholtz's expression with the permittivity term and applied it to a cross-section of arbitrary shape (Smoluchowski 1905). This expression is now known as the *Helmholtz-Smoluchowski equation* and is written as

$$u = -\frac{\varepsilon\varepsilon_o \zeta E_x}{\mu}, \tag{1.1}$$

where u is the EO velocity, E_x is the component of electric field in the positive x direction, ζ is the zeta potential/surface potential, μ is the dynamic viscosity, ε_o is the permittivity of vacuum, ε is the relative dielectric permittivity of the medium (dielectric constant).

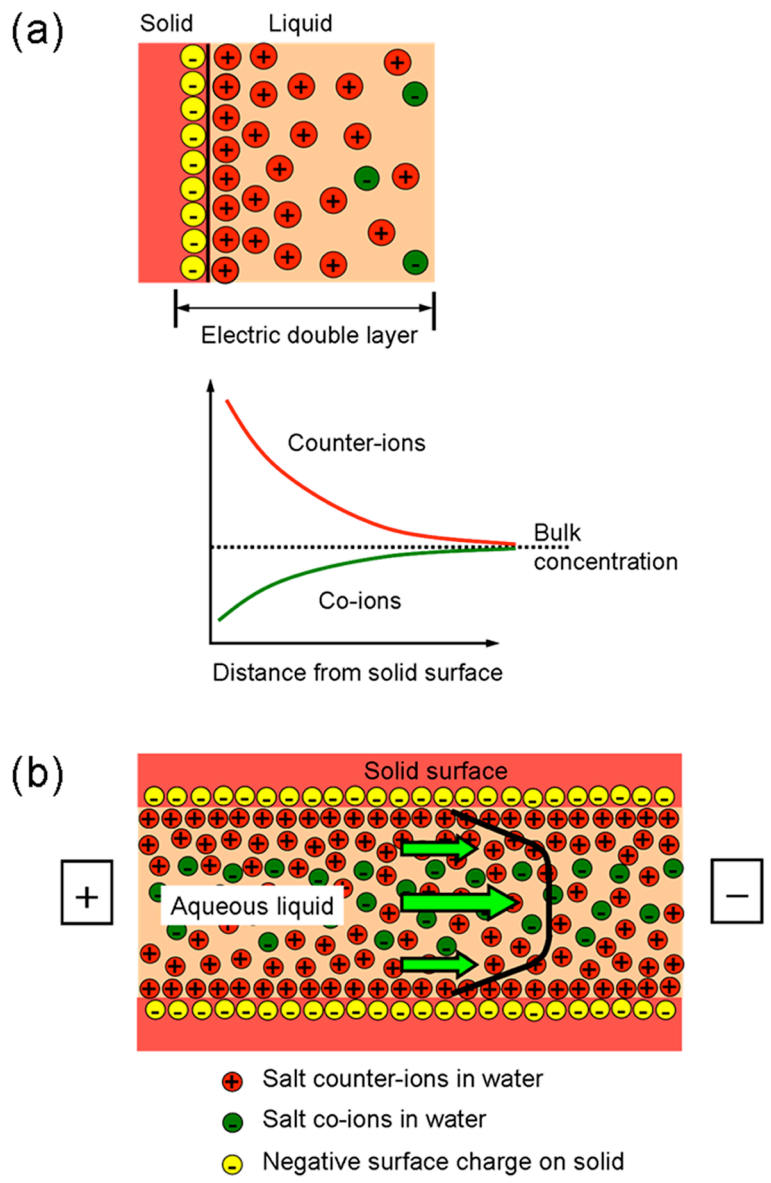

Figure 1.1 (a) Electrochemistry of a solid-liquid interface. Counter-ions in the liquid accumulate in the vicinity of the charged surface forming the electric double layer. (b) An externally applied electric field causes motion of counter-ions that shield a negative surface charge. Viscous drag causes the flow.

1.2 Electro-Osmotic (EO) Micropumps

Although the phenomenon of electro-osmosis has been known for nearly two centuries, its application to miniaturized devices, pumps in particular, for the generation of fluid flow has been of interest only in the last three decades. EO pumps are devices with no moving parts and offer distinct advantages over other micropumps in terms of pressure – they are known to generate significant pressure through pores or channels. The first instance of using electro-osmosis to drive fluid was reported by Pretorius et. al. in the mid-1970s (Pretorius et al. 1974). They used EO flow to drive liquid through a chromatographic separation column as an alternative to high pressure pumping. However they did not demonstrate the ability to generate high pressure. They used a 5 cm long, 1 mm inner diameter glass column packed with polydisperse silica particles (particle diameter ranging from 1-20 μm) to generate EO flow and reported a flow velocity of 0.2 mm/s at a field of 2000 V/cm. They concluded that adequate flowrates can be attained by using acceptable electric field strengths and that flowrate is substantially independent of the channel size. The very next year Theeuwes patented an EO pump for the generation of relatively high-pressure flow streams (Theeuwes 1975a, 1975b). He introduced the concept of miniaturized EO pump and designed a pump with a fluid dispenser attached to it. The pumping device was a porous plug made of porcelain, having 0.1 μm diameter pores, 21% porosity and 0.2 cm thick. He demonstrated a flowrate of 0.3 ml/hr with an output pressure of 0.7 atm at an applied potential of 50 V. The main application of his device was for a variety of controlled drug delivery systems. He also noted that the pump pressure showed a linear dependence to applied voltage.

Two and a half decades later, Gan and co-workers reported an EO pump flow injection analysis system with two homemade EO pumps and applied it in the determination of chromium (VI) traces in waste-water (Gan et al. 2000). Their EO pump consisted of a porous core made from boric glass powder by high temperature sintering. The porous core was 35 mm in diameter, 13 mm thick and had a pore size of 2-5 μm inner diameter. They demonstrated the pumping of several different electrolyte chemistries and their effect on the EO current, flowrate and efficiency of the pump. Their pumps generated a maximum flowrate of 3 ml/min at an applied voltage of 500 V resulting in a pump efficiency of approximately 87%. The maximum achieved pressure was 1.5 atm. That same year, Paul and Rakestraw (Paul and Rakestraw 2000) built and patented a packed column EO pump consisting of a glass capillary having a porous dielectric medium packed with silica beads and having the capability of generating high pressures. The capillary used was 15 cm long with an inner diameter of 75 μm and the silica beads were 3 μm in diameter. For an applied field of about 300 V/cm, they observed a pressure in excess of 170 atm. The inventors and co-workers later patented the use of these pumps as miniaturized high-pressure valves (Paul et al. 2001).

The following year, Zeng et. al. presented an analytical model and characterization of a relatively large inner diameter (> 500 μm) EO pump and described it's low and high back pressure operation (Zeng et al. 2001). Their EO pumps were fabricated by packing fused silica capillaries (500-700 μm inner diameter) with 3.5 μm diameter non-porous silica particles. The maximum flowrate and pressure generated by the EO pump was 4.8 μl/min and 23.5 atm, respectively at 2 kV applied voltage. In an effort to increase the flowrate of such pumps the authors later used polymerized porous

frit structures densely packed with non-porous silica particles (Zeng et al. 2002). The frits were made using UV photopolymerization and the particles were packed using a novel side-bore packing technology (figure 1.2). These structures resulted in a maximum flowrate and maximum pressure of 0.8 ml/min and 2 atm, respectively at 1.0 kV applied voltage.

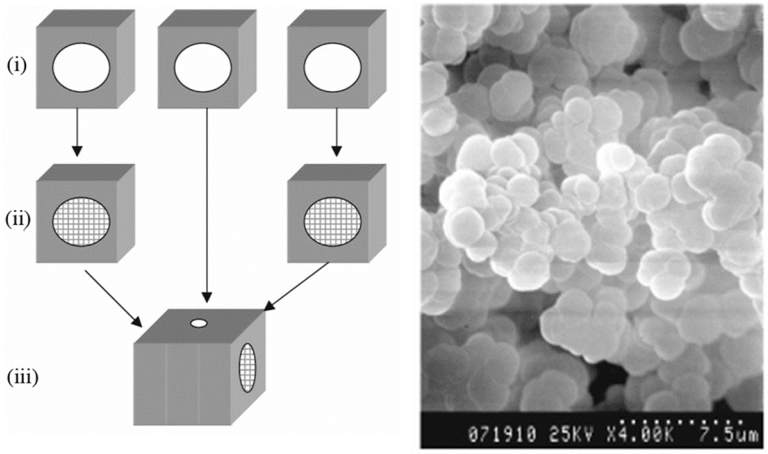

Figure 1.2 (a) Schematic illustration of parts and procedures for fabricating polymer frit EO pumps: (i) three similar frames are fabricated in acrylic; (ii) frits are polymerized into two of the frames; and (iii) the three frames are bonded and particles are loaded through a side port on the middle frame. (b) Scanning electron micrograph of polymer frits. (Zeng et al. 2002)

That same year, members from the same group also presented a planar EO micropump fabricated on a soda-lime glass substrate using photolithography and chemical wet etching techniques (C. H. Chen and Santiago 2002). They achieved a maximum pressure of 0.33 atm and a maximum flowrate of 15 μl/min at 1 kV that agreed

well with their theoretical model.

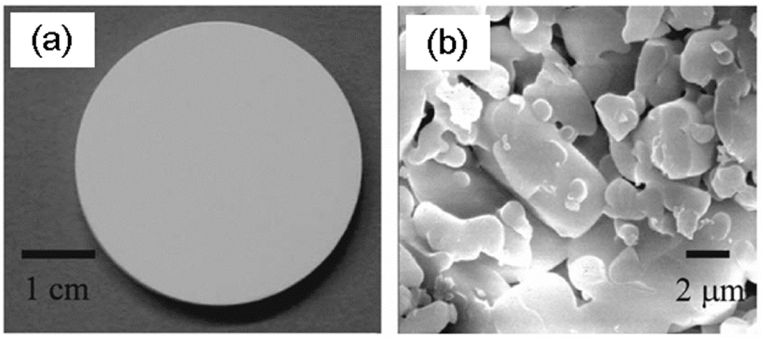

Figure 1.3 (a) Optical image of the porous glass frit. (b) A scanning electron micrograph of the same frit. (Yao et al. 2003)

Moving away from packed particle EO pumps, Yao et. al. reported EO pumps fabricated out of commercially available sintered porous glass frits (Yao et al. 2003). They performed a thorough analytical investigation of their pumps and modeled the EO flowrate, total pump working current and thermodynamic efficiency. Later they used their model as a design guideline and presented a detailed experimental validation of the performance of their pumps. The glass frit used was 5 mm thick and 40 mm in diameter with pore sizes on the order of 1 μm (figure 1.3). Their pump had a maximum flowrate and pressure capacity of 33 ml/min and 1.3 atm respectively, at an applied potential of 100 V. In addition to the pump they also demonstrated and characterized a gas recombination device to allow the cathodic hydrogen gas to bypass the pump output flow stream and combine directly with the oxygen produced at the anode. This device ensured that the pressure in their closed-loop system stayed under 0.1 atm (figure 1.4).

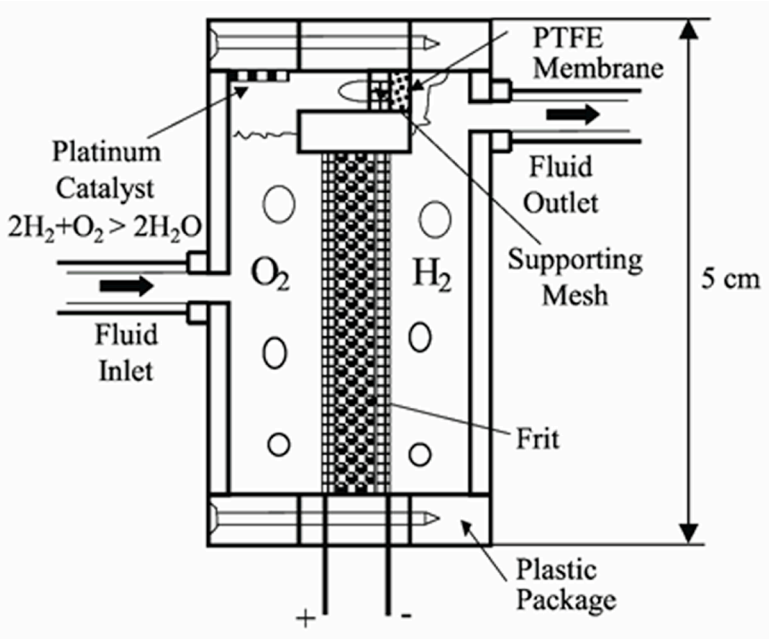

Figure 1.4 Schematic of the EO pump system designed by Yao, along with the gas recombination device. The hydrogen gas generated at the cathode permeates through the gas permeable teflon membrane and combines with the oxygen generated at the anode. The platinum catalyst recombines the hydrogen and oxygen gas into water. (Yao et al. 2003)

More recently, EO pumps have been fabricated out of porous monoliths. The advantage of using a monolith is that it can be prepared in situ by a simple chemical synthesis process and completely fills the volume of the designed chamber or a capillary. Tripp et. al. synthesized porous polymer monoliths by polymerization from liquid precursors and grafted the pore surface with ionizable monomers (Tripp et al. 2004). They studied and quantified the effects of pore size, percentage of ionizable moieties in the grafted layer, cross linking density, and driving voltage on flowrate and pressure.

Their monoliths generated a high pressure of 3.75 atm and a flowrate of up to 0.41 ml/min at an applied potential of 50 V. Wang and colleagues used silica monoliths fabricated by a sol-gel process to develop an EO pump (Wang et al. 2006). Since their monolith was silica based they were able to use organic solvents without swelling issues. The maximum flowrate and pressure generated by their 100 μm inner diameter monolith was 2.9 μl/min and 3 atm, respectively at 6 kV applied voltage.

Silicon has been another alternative material used in the fabrication of EO pumps. Laser and co-workers reported EO pumps fabricated from silicon substrates and tested them for integrated circuit thermal management applications like single phase forced convective cooling of small IC hot spots (Laser et al. 2001; Laser et al. 2003). Their prototype micropumps produced a maximum flowrate of 170 μl/min and a maximum pressure of 0.09 atm operating at 400 V. On similar lines, members from the same group used commercially available porous silicon membranes to realize EO pumps generating a high flowrate per unit applied voltage (Yao et al. 2006). The membranes had hexagonally packed pores, 1-3 μm in diameter. Unlike the frits and packed column EO pumps reported earlier, these membranes have parallel straight pores running through the length of the membrane (figure 1.5). Thermal oxide or oxidized low pressure chemical vapor deposited polysilicon provided the insulation surfaces. A pumping set-up, similar to the one shown in figure 1.4 was used for the characterization of these membranes. These pumps achieved a maximum flowrate of 3.2 ml/min at an applied voltage of 25 V and generated a pressure of 0.007 atm.

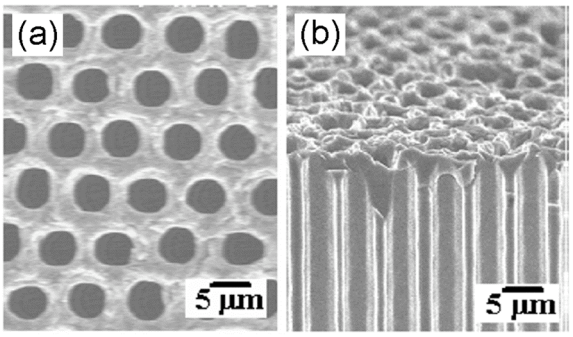

Figure 1.5 Scanning electron micrograph of porous silicon membranes: (a) Top view showing the hexagonal array of pores. (b) Cross-sectional view showing parallel, straight pores. (Yao et al. 2006)

Other notable works on electro-osmosis and its use in pumping have been reported by Jacobson et al. 1994; McKnight et al. 2001; Ramsey and Ramsey 1997. Jacobson and co-workers designed and fabricated an open channel liquid electrochromatography system on a glass microchip for separating and analyzing neutral species. Their system consisted of a microchannel with a chemically modified surface wherein they used EO flow for loading and pumping their samples onto the microchip. Ramsey and co-workers designed a microfluidic device to generate electro-osmotically induced pressures for creating a fluid electrospray from the end of a microchannel by applying an electric potential of sufficient amplitude between a microchip and a conductor spaced from the channel terminus. Their intention was to use this device for non-fluorescent molecule detection by coupling it with a mass spectrometer. They claimed that the coupling would enhance the informational output significantly. McKnight and colleagues used electro-osmosis for the purpose of demonstrating field-free fluid manipulation within microchannels. They patterned a pair of electrodes within

a microchannel and generated EO flow between them. The EO flow provided electric field-free pumping of fluid in channel regions outside of the electrodes.

EO pumps have found applications in various micro-/nano-electro-mechanical systems (MEMS/NEMS) and have the potential to impact a variety of engineering areas including microelectronics cooling and bio-analytical systems (Fintschenko and van den Berg 1998; Jiang et al. 2002; MacNair et al. 1997). One such microelectronic cooling application is to reduce the temperature of small, high power density regions of microchips through single phase forced convective cooling (Laser et al. 2003). High performance ICs are made up of a mixture of high and low power devices that are prone to develop hot spots during operation. Even with chip scale heat sinks designed for the removal of the chip's overall heat generation, the thermal resistance associated with solid-state conduction to the heat sink may be too large to avoid excessive temperatures at hot spots. A single phase forced convection cooling system as shown in figure 1.6 is one possible solution. Laser and colleagues have used a simple model and estimated a flowrate of 620 μl/min required for a forced convective cooling of a 2 W hot spot when the fluid temperature is allowed to rise to 70 °C. To demonstrate the application for microelectronic cooling, Jiang et. al. developed a closed-loop two-phase microchannel cooling system using an EO pump (Jiang et al. 2002). Using 1 mM buffered de-ionized water as the pumping fluid, a flowrate of 7 ml/min and a backpressure of 1.57 atm, their EO pump removed 38 W with a pump power of 2 W (figure 1.7).

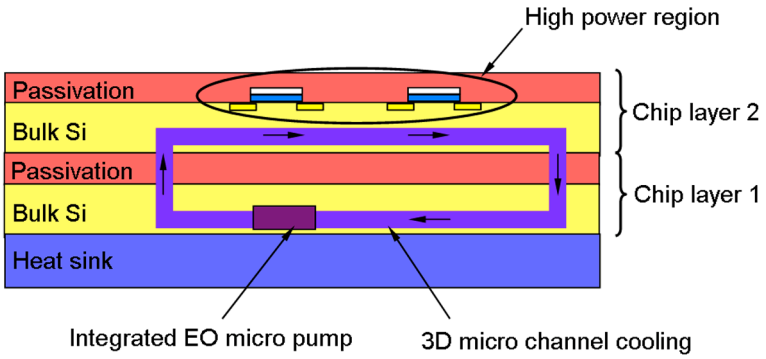

Figure 1.6 Schematic of the thermal management system for ICs based on integrated EO pumps and microchannels. (Laser et al. 2003)

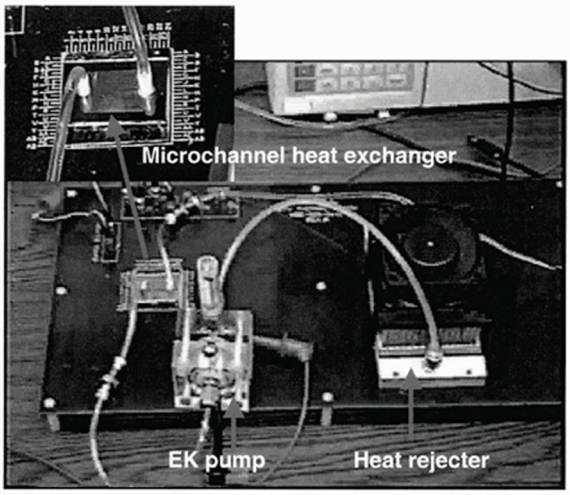

Figure1.7 Image of the closed loop cooling system incorporating the porous glass frit EO pump. (Jiang et al. 2002)

A recent press release by International Business Machines (IBM) titled "Made in IBM Labs: IBM Cools 3-D Chips with H_2O" further emphasizes the significance of EO pumps in the area of microelectronic cooling (IBM 2008). Their researchers have developed 3-dimensional chip stacks, which they claim to be a promising approach to enhancing chip performance by increasing a processor's capability to process data. A 3-

dimensional chip stack is a bunch of chips and memory devices stacked one on top of the other instead of the traditional side-by-side stacking on a silicon wafer. However, the vertical stacking of chips results in significant thermal management challenge since each intermediate layer poses as a barrier to heat removal and conventional coolers attached to the back of a chip do not suffice. To resolve this thermal issue these scientists designed micron scale pipes aligned vertically in between individual chip layers and pumped water around them in order to remove heat efficiently at the source. They demonstrated a cooling performance of up to 180 W/cm^2 per layer in a stack of 4 cm^2. A schematic of the 3-dimensional chip stack developed by these scientists is depicted in figure 1.8.

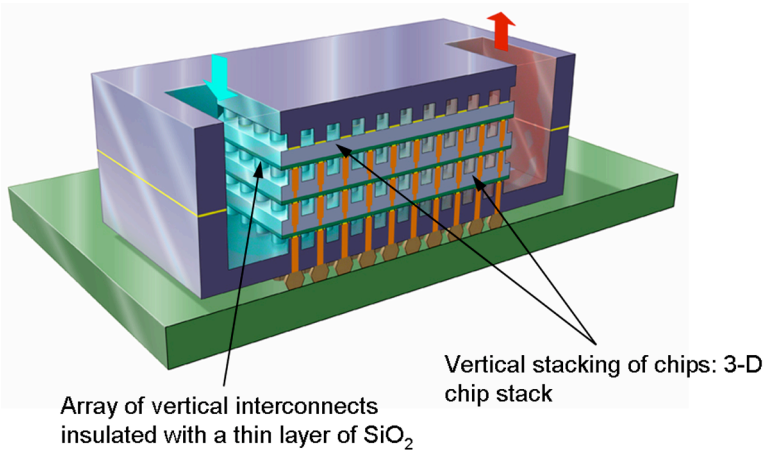

Figure 1.8 A 3-dimensional chip stack developed by IBM researchers incorporating water to remove heat generated in multilayer chips.

Despite all the efforts undertaken in the past couple of decades for the development of EO pumps, most porous membrane EO pumps reported in literature so far have suffered from low flowrates due to low porosity, high tortuosity (defined as

square of the ratio of the effective total length of zigzag microchannels to the physical pump length) and a non-uniform pore size of the porous membranes. They also have a relatively large thickness of the porous materials used for pumping thus requiring a higher applied voltage to achieve a sufficient field within the pump. For example, the pump demonstrated by Gan used a membrane of 13 mm thickness along the flow direction and could not generate sufficient field within the pump (Gan et al. 2000). Another instance is that of the pump reported by Zeng which also suffered from a low available electric field within the pump due to the presence of two 5 mm thick polymeric porous frits (Zeng et al. 2002). It is apparent from these previous efforts that the membrane used for EO pumping must have a high porosity, a low channel tortuosity, and a short channel length to achieve a high EO flowrate under low applied voltages.

A porous anodic alumina (PAA) membrane, with its excellent pore size uniformity, a high porosity, a low tortuosity of unity and low fabrication cost serves as an ideal candidate for EO pumping. Moreover, the nanometer scale pores of the PAA membrane should generate high enough pressures since the EO pump pressure scales inversely with the square of pore diameter. This dissertation will discuss the in-house fabrication of nano-structured silica coated PAA membrane for use as an EO pump. These membranes have been characterized on the basis of their EO pump flowrate and results show that they can provide a normalized flowrate of 0.125 ml/min/V/cm^2 under a low effective applied voltage of 3 V. This is orders of magnitude higher than most other EO pumps made from porous materials such as glass frits. In addition, this dissertation also presents some interesting flow phenomena for the nanometer scale pores of the PAA membrane, i.e., the effect of EO flowrate through these pores at very low buffer solution

concentrations (concentrations at which the double layers overlap) and ionic conductance at these concentrations and its deviation from the bulk value. Furthermore, EO flowrate characterization of the uncoated PAA membrane is also presented, which shows an unexpected non-linear trend with the effective applied voltage.

1.3 Porous Membrane EO Micropumps with Field Effect Flow Control

Tuning of EO pump performance has been achieved primarily through the following three approaches:

1. By changing the chemical composition of the buffer solution, i.e., ionic strength of buffer solution and solution pH (Lambert and Middleton 1990; McCormick 1988; Schwer and Kenndler 1991).
2. By coating the inner surfaces of the fluid channels and thus changing the zeta potential of the inner walls (Hjerten 1985; Jorgenson and Lukacs 1983; Vajandar et al. 2007).
3. By changing the applied electric field across the channels.

In addition to these, a more subtle control over EO flow can be achieved by modulating the zeta potential within the channels while keeping the main electric field along the channels constant. This can be done by applying a transverse electric field over the thin insulating wall of a microfluidic channel. The transverse field polarizes charge within the insulator and thereby modulates the surface charge density at the insulator/fluid interface within the channel. The principle is analogous to that of a solid-state field-effect transistor in integrated circuits, where an electric current is regulated by a perpendicular electric field generated by a third electrode termed as the “gate” electrode. Since this

principle involves the electric field manipulation of fluid flow, it has been termed as *Field Effect Flow Control* (FEFC).

FEFC was first demonstrated in the early 1990s by Lee and co-workers (C. S. Lee et al. 1990). The main application of their work was in the field of capillary zone electrophoresis (CZE) where they used this principle to enhance the separation efficiency and to prevent protein adsorption onto the walls of a capillary. A drawback of their work was the high voltages (several kilovolts) that had to be applied over the thick capillary wall to establish a significant change in the zeta potential. This was followed by similar works in the area of CZE by Ghowsi and Gale 1991; Hayes and Ewing 1992; Hayes et al. 1993a, 1993b; C. S. Lee et al. 1990; Polson and Hayes 2000; Wu et al. 1992.

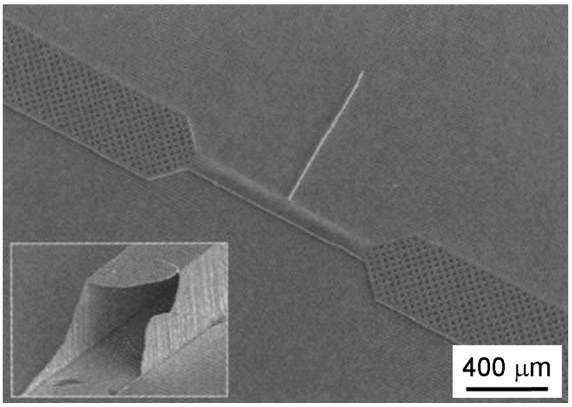

Figure 1.9 Scanning electron micrograph of the micro fabricated silicon nitride channel at the junction region. Inset: Scanning electron micrograph of the side channel cross-section showing the insulating 390 nm thick silicon nitride wall. (Schasfoort et al. 1999)

In 1999, Schasfoort and colleagues demonstrated the use of FEFC for electro-osmosis in microfluidic networks (Schasfoort et al. 1999). With modern microfabrication

techniques they were able to fabricate silicon nitride channels on a silicon wafer, having extremely thin walls (390 nm thick) that required a gate voltage of only tens of volts to generate significant field effect (Figure 1.9). They demonstrated that field effect control can manipulate the magnitude and even reverse the direction of EO flow within a microfabricated fluidic channel by applying a perpendicular electric field of 1.5 MV/cm. generated by a gate voltage of only 50 V using a low pH value buffer solution. Members of the same group later reported FEFC in microfluidic networks based on glass microchannels with integrated insulated gate electrodes that were used to modify the zeta potential at particular locations on the wall surface of the microchannels (van der Wouden et al. 2005). They claimed that these microchannels were mechanically more robust and had a better flow visualization in the gate region as compared to their previous work. On similar lines Buch and co-workers demonstrated FEFC in a polydimethylsiloxane (PDMS) based microfluidic system (Buch et al. 2001). Their microchannel was formed in PDMS, which was bonded to a silicon wafer with a 2 μm thick electrically insulating layer of silicon dioxide over it. The underlying silicon acted as the gate electrode. More recently, FEFC has been reported in nanofluidic systems (Z. Chen et al. 2005b; Karnik et al. 2005). The authors have demonstrated gate effect on the concentration of ions and molecules in the channel and ionic conductance by using a combination of fluorescence and electrical measurements. The nanochannels used in their work were fabricated out of silica. Field effect was demonstrated in both two-dimensional (2D) nanochannels and one-dimensional (1D) nanotubes (figure 1.10).

To date, all FEFC studies have been performed on single micro- or nanochannels primarily for studying separation science. For EO pumps, however, the desired flowrates

are achieved with porous membranes or microchannel arrays. FEFC on porous membranes or microchannel arrays will enable high performance porous membrane EO pumps having a wide range of zeta potentials, since this potential can be controlled by gate voltage. Moreover FEFC could be a better approach than other control methods to tune the EO flow because for many applications, certain electrolyte pH is required and coating the inner surface of the channel to increase the zeta potential can be a challenge. Even if a successful coating of the channel is achieved, the EO pump gets limited to buffers within a certain pH range. For example, FEFC can be particularly useful in micro-flow injection analysis (μFIA) systems using EO pumps such as that reported by Chen and co-workers (Z. Chen et al. 2005b), which makes use of an EO pump to produce an electro-spray. However, when delivering a low pH fluid, chemical modification was needed on their EO pump in order to maintain a significant flowrate. With FEFC, the pump can be used for both high and low pH fluids to produce desired flowrate without chemical modification of the channel surface. In addition, many EO pumps use very high voltage (on the order of kilovolts) along the main flow direction (Gan et al. 2000; Paul and Rakestraw 2000; Zeng et al. 2001; Zeng et al. 2002), making it difficult to further tune the EO flow by increasing the applied voltage along the flow direction. FEFC can control the EO flow at a constant externally applied voltage with the application of a gate potential of relatively low magnitude.

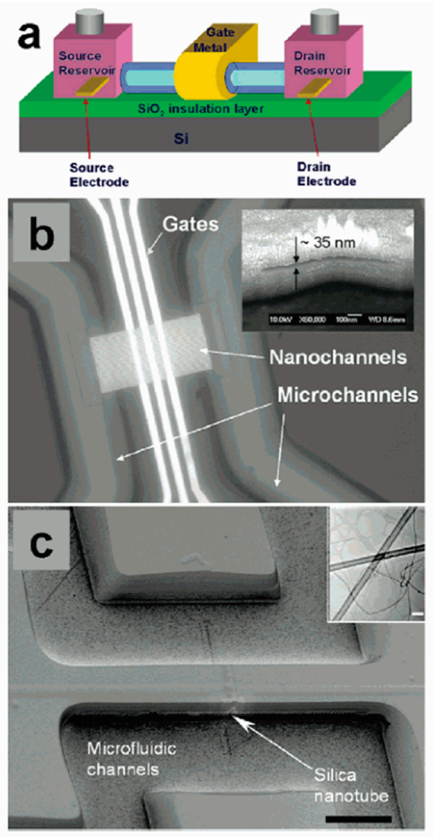

Figure 1.10 Nanofluidic transistor devices. (a) Schematic of a nanofluidic transistor. (b) Scanning electron micrograph of the two-dimensional silica nanochannel transistor. (c) Scanning electron micrograph of a one-dimensional silica nano tube transistor. Scale bar is 200 nm. (Karnik et al. 2005)

This dissertation will present detailed fabrication and characterization of a SiN_x-coated porous silicon EO pump having gate modulated flow control. Furthermore the dissertation will discuss electrical current leakage through SiN_x, which is unexpected because LPCVD SiN_x is well known as an excellent insulator. The leakage current observation brings to light the electrolytic rectification effect in an electrolyte-insulator-semiconductor system.

1.4 Ionic Conductance Measurements

EO pumping is closely related to the ionic current through micro- and nanoscale fluidic channels. Therefore, a thorough understanding of ionic current through micro- and nanochannels is essential for the understanding of EO flow and better design of EO pumps. Over the past decade, ionic current through nanochannels has attracted a lot of attention, mainly because of its important implications in single molecule detection with the resistive pulse sensing (Coulter counter) technique.

Nanoscale Coulter counters use either naturally occurring protein nanopores or laboratory-made inorganic nanopores/channels with dimensions comparable to the size of single molecules, to detect the translocation of single molecules or nanoparticles. (Chang et al. 2004; Henriquez et al. 2004; Kasianowicz et al. 1996; J. Li et al. 2001; Smeets et al. 2005). These nanoscale Coulter counters rely on sensing the ionic current through the nanopore and its modulation from the translocation of individual nanoparticles or single molecules to their detection and interrogation of their properties. The baseline ionic current, which itself is a function of the pore size, electrolyte concentration, applied electric field, and surface properties of the nanopore, is of consequence because it discloses many unique phenomena occurring within these nanopores. Furthermore the sensitivity of these Coulter counters is determined by the stability and noise of the baseline ionic current.

To better understand the ionic current through nanopores, several studies have recently been carried out. Stein and co-workers measured the electrical conductance of silica nanochannels filled with different concentration KCl buffered solutions (Stein et al. 2004). Their results indicated that at low concentration, the electrical conductance was

dominated solely by the surface charge, independent of salt concentration. Daiguji et al. first reported theoretically the possibility of creating a unipolar solution of counter-ions in a 30 nm diameter silica nanotube and using a gate electrode to modulate the ionic current through the nanotube (Daiguji et al. 2004). Later, Karnik and collaborators experimentally observed the modulation of the electrical resistance through both ~ 50 nm diameter nanotubes and 40 nm high, 1 μm wide nanoslits by applying a gate potential (Karnik et al. 2005). Schoch and Renaud measured and modeled the electrical conductance of an electrolyte-filled nanoslit of 50 nm in height (Schoch and Renaud 2005). Their results indicated that at low salt concentrations, the electrical conductance was dominated by the effective surface charge density, which could be regulated by the pH and external gate potential. All reports to date indicate that ionic current through a nanopore/channel at low electrolyte concentrations is determined solely by the surface charge density of the nanopore/channel, while at higher concentrations, the ionic current can be estimated based on the bulk electrolyte concentration and the size of the nanopore. However, all of the previous research has been focused on the effects of overlapped EDLs (low concentration electrolytes) without paying much attention to ionic transport through nanopores at high concentration electrolytes with non-overlapped double layers. Therefore, ionic current data for high concentration electrolyte through nanopores is limited and not systematic.

A recent molecular dynamics (MD) simulation, however, indicated unusual ionic current trends in a 3 nm diameter nanopore having high surface charge density at high electrolyte concentrations (Ge et al. 2009). In the last part of the dissertation, we tried to verify the MD simulation results experimentally by measuring the ionic current through a

nanoporous glass membrane with an average pore size of 4 nm. The ionic current was measured with two kinds of electrolytes – NaCl and KCl. The experimental results indicated a linear trend of ionic current for electrolyte concentrations beyond 1 M, contrary to the results of the MD study, which was attributed to a low surface charge density measured for the porous glass membranes.

1.5 Summary

In summary, this dissertation will focus on electro-osmotic phenomena in micro-/nanoporous membranes of three different materials. Two of these have been fabricated in-house and their fabrication details will be presented. Of these two membranes, one has been characterized as a high flowrate EO pump while the other has been used as an EO pump having gate controlled flowrate modulation. The third porous membrane is commercially fabricated and used for studying ionic current at high electrolyte concentrations. The characterization details for all three porous membranes will be discussed at length. The organization of this dissertation is as follows:

- Chapter I reviews the background and previous work in the area of electro-osmotic pumps, field effect flow control and ionic transport through nanopores/channels.
- Chapter II details the fabrication of silica coated PAA membranes and SiN_x coated porous silicon membranes.
- Chapter III discusses the characterization of silica coated PAA membranes as high flowrate EO pumps.

- Chapter IV presents the characterization details of gate bias modulated flowrate in SiN_x-coated porous silicon membranes followed by a discussion of current leakage through SiN_x thin films.
- Chapter V focuses on ionic current through nanoporous glass membranes at low and high electrolyte concentrations.
- Chapter VI summarizes and concludes the dissertation.

CHAPTER II

POROUS MEMBRANES – MATERIALS AND FABRICATION

Porous membranes have generated significant scientific and technological interest because of their extremely large surface area to volume ratio, which provides many advantages and opportunities. It therefore does not come as a surprise that these materials have found their worth in a wide range of applications: for example, they have been used for separation and purification purposes (Bhave 1991), as high surface area adsorbents (Fain 1994), as solid supports for sensors and catalysts (Keizer 1996; Lin et al. 1997), as template materials for synthesis of nanotubes (N. I. Kovtyukhova et al. 2003; Kyotani et al. 1996), as scaffolds for tissue engineering (Hubbell 1995), and as low-dielectric constant materials for microelectronic devices (Hedrick et al. 1998; Prakash et al. 1995). These materials have also been actively explored as photonic band gap (PBG) materials for use in optoelectronics (Joannopoulos et al. 1997) and as new types of mechanical materials that may exhibit negative Poisson's ratios (Lakes 1987). This dissertation presents research on EO pumping with porous membranes, and this chapter will focus on the fabrication of two kinds of porous materials – the PAA membrane and porous silicon.

2.1 Porous Anodic Alumina (PAA) Membrane

Anodization by definition is the electro-oxidation of a metal in the presence of an acidic or basic electrolyte resulting in the formation of an oxide layer of the respective metal over the surface. This was a commercial method employed on aluminum surfaces in the early 1920s for decoration purposes and protection against corrosion (Bengough

and Stuart 1923). Since then this method of oxidizing aluminum has been investigated and used in numerous products (Diggle et al. 1969; M. S. Hunter and Fowle 1954; Keller et al. 1953; Lohrengel 1993; Thompson et al. 1978; Thompson and Wood 1981; Wood and O'Sullivan 1970) and more recently the nanoporous form of this oxide has become a popular template system for the synthesis of various functional nanostructures (N. I. Kovtyukhova et al. 2003; N. L. Kovtyukhova and Mallouk 2005; S. B. Lee et al. 2002; Linjie Zhi 2005; Mikulskas et al. 2001; Park et al. 2004; Sarah J. Hurst 2006; Woo Lee 2005). Depending on the anodization conditions (temperature, current density, anodization voltage), the anodization process can be classified into two categories – mild anodization (MA) and hard anodization (HA). Here, a brief description on both processes will be given within the confines of the subject matter of this dissertation.

2.1.1 Mild Anodization (MA)

Mild anodization is the most widely used method for fabrication of PAA membranes since the anodization conditions are less extreme, and therefore can be carried out without the need of using specialized tools and equipments. However, in the event of fabrication of thick membranes (on the order of tens to hundreds of microns) this method becomes very time consuming – nearly 20 hours for making a 100 μm thick film. The most commonly used acidic electrolytes for carrying out MA have been reported to be chromic, sulfuric, oxalic, phosphoric and boric acids (Wernick et al. 1987). Contingent upon the anodization conditions, in particular the pH value and the type of electrolyte used, the MA membranes can be further classified into barrier-type and porous-type membranes

- *Non-porous barrier oxide film:* When MA is carried out in completely insoluble electrolytes (electrolytes in which the anodized alumina does not dissolve), e.g., boric acid ($5 < pH < 7$), a flat, non-porous insulating oxide known as the 'barrier layer' forms. In this case the film growth continues until the resistance of the film prevents any more current from reaching the anode and the anodization stops due to passivation of aluminum surface.
- *Porous oxide membrane:* When MA is carried out in mildly soluble electrolytes (electrolytes in which the anodized alumina dissolves partially), e.g., chromic, oxalic, phosphoric or sulfuric acids, a porous membrane forms with a thin barrier layer present at the bottom of each pore. In this case the oxide membrane growth is accompanied by localized dissolution of the membrane.

The pore formation mechanism in a MA porous membrane is reflected on a potentiostatic current density curve, a typical example of which is depicted in figure 2.1. The curve is divided into four regimes corresponding to the four steps occurring during pore formation (Diggle et al. 1969; Jessensky et al. 1998; Parkhutik and Shershulsky 1992).

Step 1: Ionic migration initially to form the barrier layer alumina, which covers the entire aluminum surface. This layer thickens until the current impedance through the oxide layer becomes significantly high. The current density therefore decreases rapidly in figure 2.1 (regime 1).

Step 2: When the barrier layer reaches a certain thickness, a field assisted conversion process starts. The electric field roughens up the oxide layer by preferential oxide growth at sites which offer least resistance for the fastest transport of oxygen through the oxide layer to aluminum. The current density reaches a minimum at this stage (regime 2).

Step 3: Field assisted dissolution of portions of the oxide at the points of field concentration. Oxide dissolution rate is faster than oxide growth rate at this stage. This results in nucleation of pores and a rise in the current density (regime 3).

Step 4: Once pores nucleate they grow perpendicular to the surface by attaining equilibrium between field-enhanced oxide dissolution at the oxide/electrolyte interface and oxide growth at the Al/oxide interface. The steady state pore formation leads to a constant current density with anodization time (regime 4).

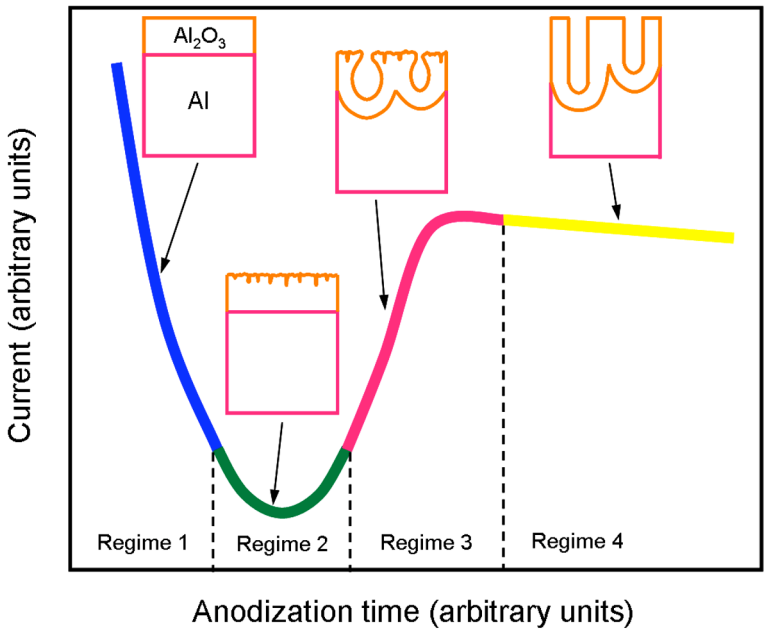

Figure 2.1 A potentiostatic current density curve depicting the four regimes encountered during pore formation in a MA process. The stages of porous structure development are also shown.

Due to the steady-state condition the barrier layer at the bottom of each pore maintains a constant thickness. While the pores nucleate at the surface at almost random positions, ordered pore domains are observed at the bottom layers indicating that longer

anodization time results in improved regularity of pores. Jessensky, Li and colleagues (Jessensky et al. 1998; A. P. Li et al. 1998, 1999) have studied the hexagonal self-organization of pores and explained the effect by taking into consideration the situation during steady-state pore growth. During anodization the volume of alumina expands roughly by a factor of two since the atomic density of aluminum in alumina is a factor of two lower than that in metallic aluminum. This translates into mechanical stresses at the Al/oxide interface causing repulsive forces between neighboring pores. Since oxidation takes place at the entire Al/oxide interface simultaneously, the oxide can only expand in the vertical direction and the existing pore walls are pushed upwards. The vertical expansion of pores and the repulsive forces between them during growth promote the formation of hexagonal self-organization of pores. The chemical reaction during anodization occurring at the anode is

$$2Al(s) + 3H_2O(l) \rightarrow Al_2O_3(s) + 6H^+ + 6e^-,$$

while at the cathode hydrogen is evolved

$$6H^+ + 6e^- \rightarrow 3H_2(g).$$

Figure 2.2 depicts the hexagonal self-organization of pores with the barrier layer present at the bottom of each pore.

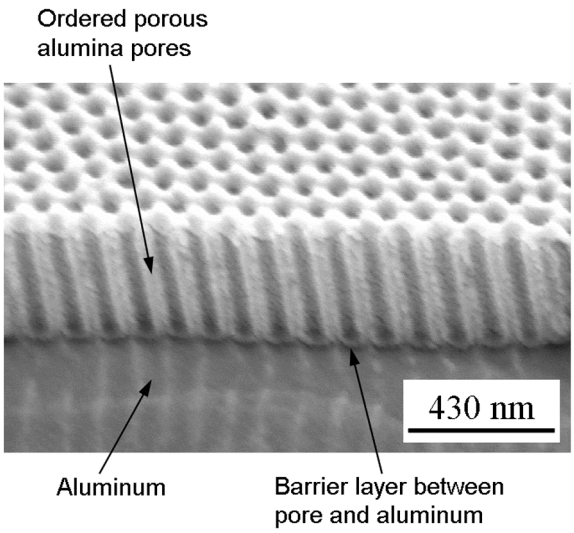

Figure 2.2 Scanning electron microscopy (SEM) micrograph of a PAA membrane prior to removal from the aluminum substrate. The barrier layer is seen at the bottom of each pore. The membrane was anodized in 0.3 M oxalic acid at 40 V and 15 °C.

Most of the MA PAA membranes reported in literature have followed a two-step replication process, first documented by Masuda (Masuda and Fukuda 1995). This approach yields a high quality membrane with good chemical and thermal stability, higher mechanical strength, and better pore ordering. A two-step replication process means aluminum films are first anodized to form oxide followed by stripping off the oxide and re-anodizing the aluminum again. The pore imprints left by the first step on the aluminum surface act as nucleation centers for pore formation in the second step. Researchers from the same group further studied the detailed conditions required for long-range self-ordering of hole configurations in these porous membranes (Asoh et al. 2001). The long-range self-ordering was observed to occur under limited voltage conditions that were specific to the solution used for anodization, e.g., in a sulfuric acid

solution, the long-range self-ordering takes place at 25 V, for oxalic acid solution it occurs at 40 V and for phosphoric acid solution it takes place at 195 V. The degree of spatial ordering decreases drastically if the anodization is carried out outside the self-ordering regime. An applied voltage that is higher than the optimum value required to maintain stable anodization in a given electrolyte results in 'breakdown' or 'burning' of the oxide film caused by catastrophic flow of electric current (Ono et al. 2004). For the purpose of this dissertation, all MA PAA membranes have been fabricated in oxalic acid using the two-step replication process and the forthcoming paragraph will detail the setup and fabrication conditions used for making these membranes.

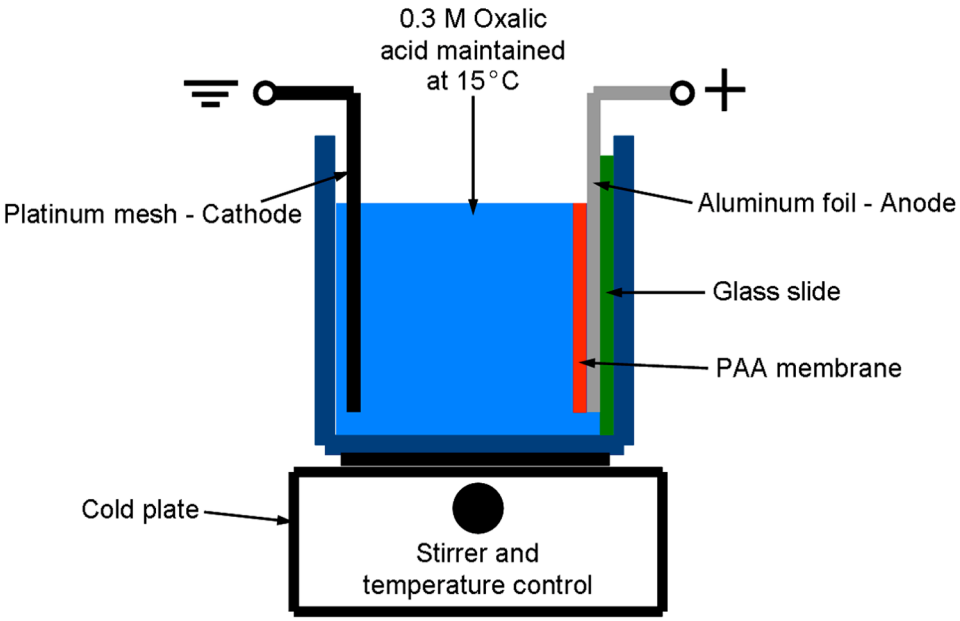

Figure 2.3 Schematic of the anodization set-up used to fabricate MA PAA membranes.

An aluminum sheet (99.99% purity, Alfa Aesar) was cut into 3 cm × 1 cm with a strip of aluminum protruding from one of the shorter sides. This strip facilitated the

connection to the anode. The sheet was then degreased and cleaned by rinsing in acetone. The cleaned sheet was mounted onto a glass slide using crystal bond (a high temperature adhesive), prior to immersing into the electrolyte for anodization. The schematic in figure 2.3 gives details of the anodization set-up. The first anodization step was carried out in 0.3 M oxalic acid solution at a constant voltage of 40 V for 5 hours. The temperature of the electrolyte was maintained at 15 °C using a cold plate under constant stirring to remove the heat evolved from anodization. The oxide formed was dissolved in an etching solution comprising of 1.8 wt% chromic acid and 6 wt% phosphoric acid at 60°C for 3 hours, which resulted in the formation of a periodic concave texture on the aluminum surface. This textured pattern behaves as self-assembled marks inducing the ordered formation of pores for the second anodization step (Masuda et al. 1997; Sulka et al. 2002). The second anodization step was carried out using identical conditions as those used for the first step but for a longer period of 16-17 hours, resulting in an ideally arranged honeycomb structure. The long anodization time improved the regularity of cell arrangement as well as reduced the number of defects and dislocations (Masuda and Fukuda 1995). The bottom aluminum layer was etched away in a saturated solution of mercury chloride, leaving behind the as-fabricated membrane. Following this the barrier layer present at the bottom of the membrane was chemically etched and the pore size increased by immersing the as-fabricated membrane in 5 wt% phosphoric acid solution at 30 °C for approximately 70 min. The step-wise flow chart in figure 2.4 describes the membrane preparation process. Figure 2.5 shows an SEM image of the MA PAA membrane surface before and after pore widening treatment.

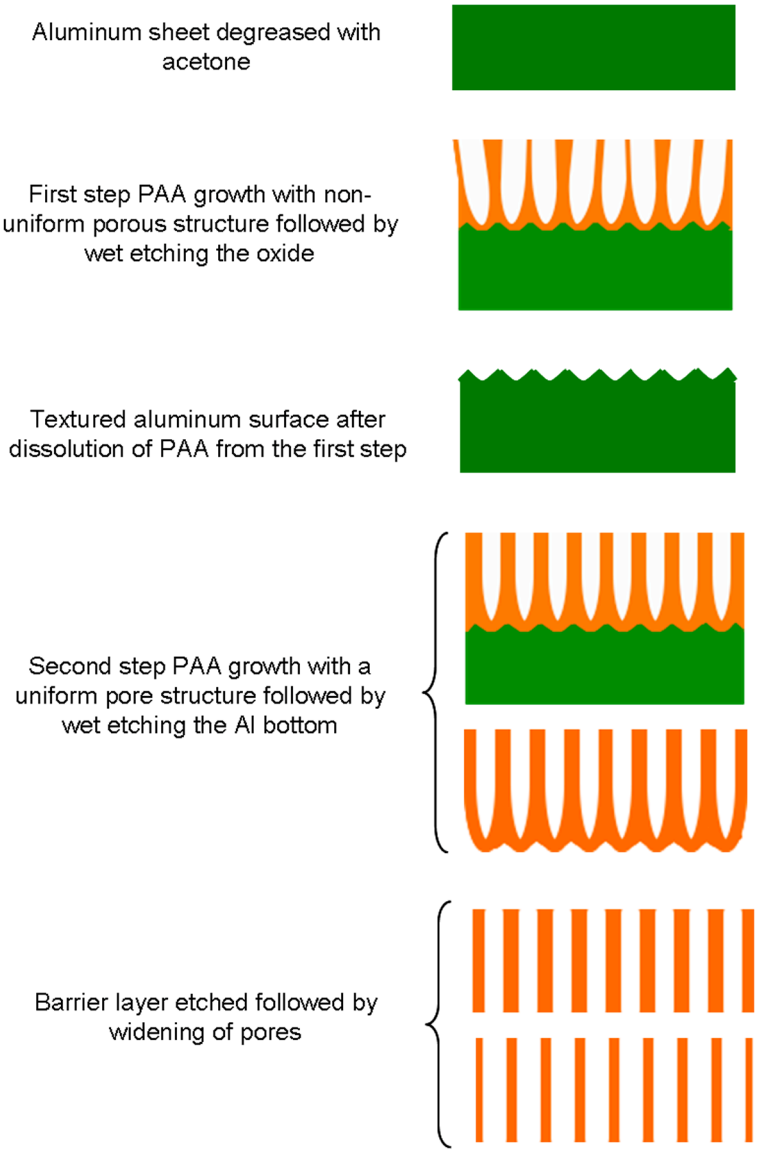

Figure 2.4 Step-wise flow chart describing the PAA membrane preparation process.

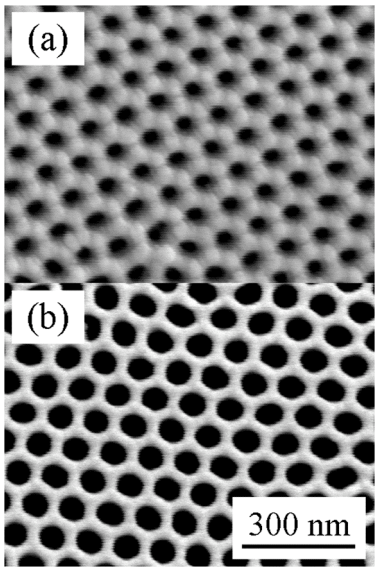

Figure 2.5 SEM images of MA PAA membrane surface: (a) before and (b) after pore widening treatment. The pore diameter before and after pore widening was around 50±5 nm and 80±5 nm, respectively and the membrane thickness was around 90±5 μm.

2.1.2 Hard Anodization (HA)

Hard anodization of aluminum was invented in the early 1960s (P. Csokán 1961; P. Csokán and Sc 1962; P. Csokán 1964; Lichtenberger-Bajza et al. 1960) and has been widely used for various industrial applications such as surface finishing of aluminum cookware, automobile engineering, textile industry, electronic parts, etc. This process is characterized by the use of relatively low temperatures and high current densities compared to the MA process. To date, industry has mostly relied on a sulfuric acid based HA process by taking advantage of the high-speed oxide growth (50-100 μm/hr) of mechanically robust nanoporous oxide films (Hecker 1988; John et al. 1984; Olbertz 1988; Rajendra et al. 2005). In academic research, however, the HA process has not been favored over the past four decades and has not been applied to the development of nanostructured materials because of difficulties in controlling important structural parameters, such as pore size,

interpore distance and the aspect ratio of the nanopores of the resulting alumina membranes.

This situation changed when Lee and co-workers reported a new self-ordering regime of PAA membranes that they found while anodizing aluminum substrates using 0.3 M oxalic acid within the potential range of 100-150 V (W. Lee et al. 2006). Just as in the case of MA PAA films, a two-step replication process is followed to improve the quality of the membrane and achieve better pore ordering. A cleaned aluminum sheet was anodized under MA conditions followed by oxide dissolution in a chromic and phosphoric acid solution. The textured sheet was then inserted into the anodization cell, which in this case was designed differently to accommodate the water sink and a thermoelectric cooler (TEC/Peltier element). Since the HA process operates at much higher voltages than the MA process, it is accompanied by large evolution of heat which has to be effectively removed. To serve this purpose a Peltier element was used which is a combination of semiconductor thermocouples that generates a temperature difference between its two sides when a voltage is applied across it. The aluminum sheet was placed in contact with the cold side and the hot side was placed in contact with a heat sink (a copper cold plate with water cooling) to take away the heat. A thermoelectric paste was applied in between the aluminum sheet and the cold side of the TEC to facilitate uniform cooling. To suppress breakdown effects and to enable uniform oxide film growth at high voltages (100-150 V), a thin layer of MA PAA film (hundreds of nm thick) was formed on the surface of the aluminum substrate before carrying out the HA process. This protective oxide layer was generated by anodizing the substrate under MA conditions (0.3 M oxalic acid at 40 V) for 5–10 min. Subsequently, the anodization voltage was

slowly increased to a target formation voltage (100–150 V) for HA at a rate of 0.3 V/s and the HA was then continued under a constant potential. It is believed that the initial surface oxide layer provides uniform pore nucleation sites at the early stage of high-voltage anodization, preventing local catastrophic events such as local flow of high electrical current and defects by surface pitting. Figure 2.6 shows a typical setup used in the fabrication of HA films and figure 2.7 illustrates the SEM images (before and after pore widening) of a HA PAA film, anodized in a 0.3 M oxalic solution at a temperature of 0 °C and 120 V. Just as in the case of MA films, the self-organization of hexagonal pore arrays in HA films has been attributed to mechanical stresses at the Al/oxide interface. The higher current densities corresponding to the HA process will generate larger mechanical stresses at the Al/oxide interface due to associated volume expansion. This high interfacial stress gives rise to greater repulsive forces between the pores at the interface. Under such an energetically unfavorable condition, the anodization proceeds in a way so as to minimize the resulting mechanical stresses between the pores, which is achieved by reducing the pore size to enlarge the surface area of the Al/oxide interface. The higher current densities, larger mechanical stresses and therefore greater repulsive forces between the pores combine to yield a smaller pore diameter (larger interpore distance) in an as-fabricated HA film when compared to the MA process. This is evident on comparing the SEM images in figures 2.5 (a) and 2.7 (a) taken before the pore widening treatment.

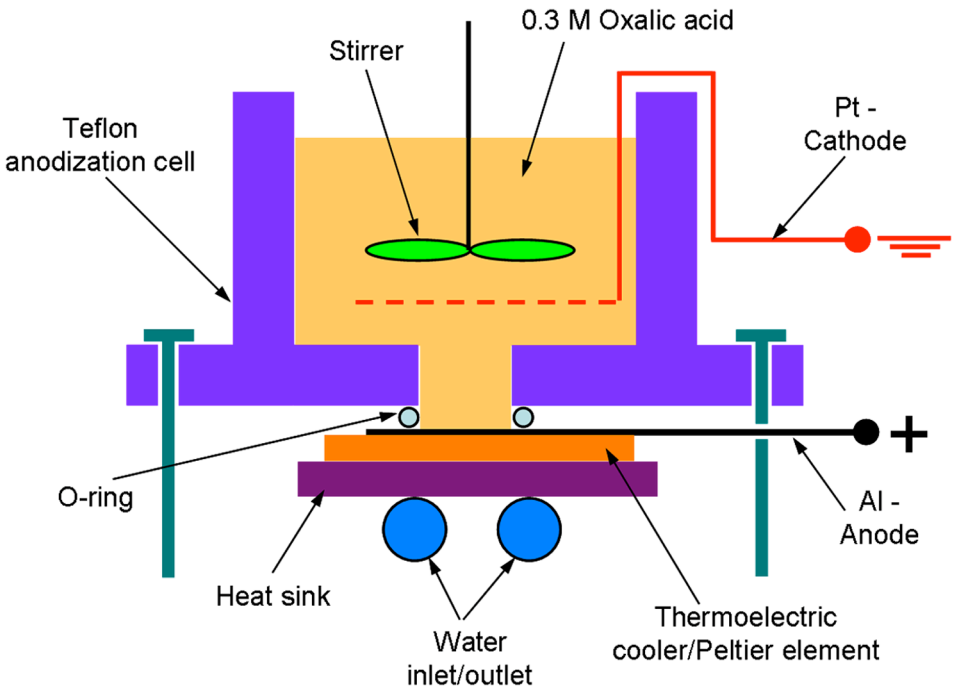

Figure 2.6 Schematic of the anodization set-up used to fabricate HA PAA membranes.

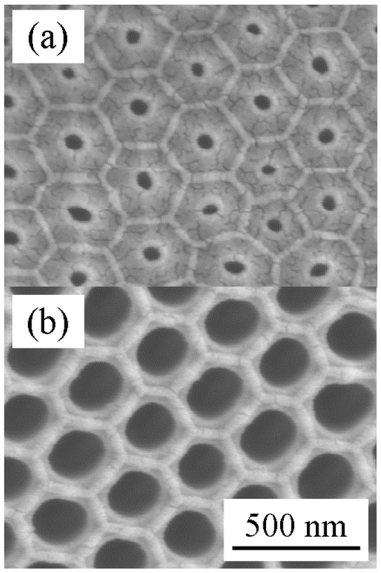

Figure 2.7 SEM images of the HA PAA membrane surface: (a) before and (b) after pore widening treatment. The pore diameter before and after pore widening was around 50 nm and 250 nm respectively.

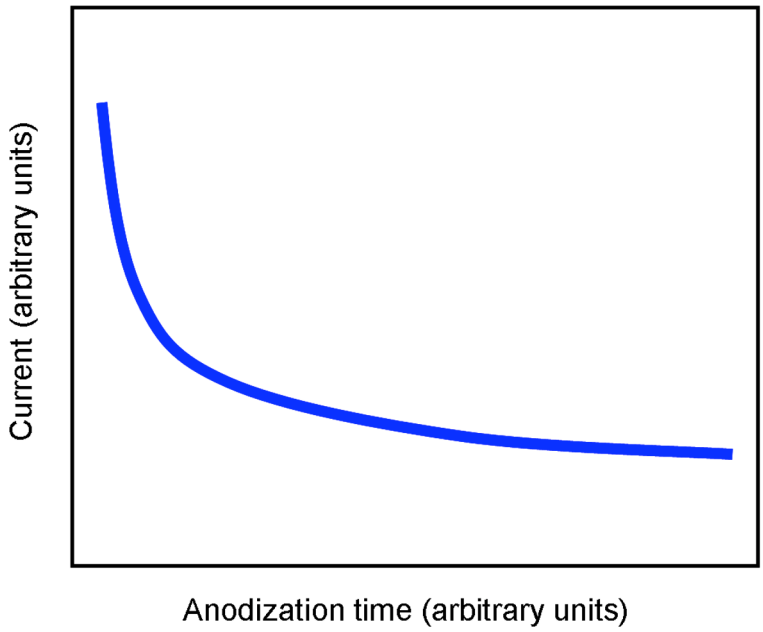

Figure 2.8 A current-time transient encountered during pore formation in a HA process.

Unlike the typical anodization curves for a MA process (figure 2.1), the current–time transient in a HA process shows a nearly exponential decay as a function of time (figure 2.8). Such a behavior of current transition for HA has been explained by the diffusion-limited electrochemical oxidation of aluminum at the pore bottom as a result of the extremely rapid and homogeneous film growth on the whole sample area. As mentioned previously, it is believed that the anodization current is mainly related to the movement of ionic species (O^{-2}, OH^{-1}, Al^{+3}) through the oxide layer at the bottom of the pores Hence the ionic current is expected to decrease, exponentially in the initial few minutes of the process (high growth rate during this time due to shorter diffusion path along the nanopores) and gradually later as the growth rate slows down over time due to the extended diffusion path along the nanopores.

2.2 Porous Silicon (PS) Membrane

Fabrication of PS membranes can be followed via two routes and depending on the end application can be made from either (a) electrochemical anodization of silicon, or (b) a combination of photolithography and deep reactive ion etching techniques (DRIE). In some respect, electrochemical anodization technique and DRIE of silicon to fabricate PS membranes can be seen as complementary techniques. Electrochemical anodization, while being limited in lateral design, has the ability to achieve very high aspect ratios. DRIE, in contrast, has a higher degree of freedom when it comes to lateral design, but aspect ratios are limited to values of about 20 and below. For the purpose of this dissertation, option (b) was chosen over (a) for reasons that will be made clear subsequently. However, a brief discussion on both techniques will be presented in this section.

2.2.1 Electrochemical Anodization of Silicon

The formation of PS through an electrochemical anodization technique was first discovered in 1956 (Uhlir 1956), which has led to interesting novel devices from quantum structures, permeable membranes to photoluminescent and electroluminescent devices. PS membranes are classified into two types based on their pore sizes, which depend on the density of doping and span over three orders of magnitude: microporous (< 50 nm) and macroporous (> 50 nm). There have been a number of different models suggested to explain PS formation as reviewed by Föll (Föll 1991) and Smith (Smith and Collins 1992). A general consensus is that the etching reaction requires electronic holes (h^+), which have to be supplied by the silicon. The basic conditions for electrochemical

pore formation in a silicon electrode are a passive state for pore walls and an active state at the pore tips promoting dissolution. Dissolution of silicon takes place in the presence of hydrofluoric (HF) acid and will occur if h^+ are present at the surface. If a h^+ reaches the silicon surface it will be consumed in a nucleophilic attack on surface Si–H bonds by fluoride ions supplied by HF acid, eventually forming SiF_6^{2-}, which gets removed from the surface (Kang and Jorne 1993; Lehmann and Gosele 1991). If a silicon atom is removed from an atomically flat surface due to this reaction, an atomic size dip is left behind which will change the electric field distribution in such a way that h^+ transfer will occur at this location preferentially, further amplifying the surface inhomogeneity (pore tips). Consequently a surface area depleted of h^+ is generated (passivated pore walls).

Since most studies on PS formation in literature have been conducted on n-type silicon, this dissertation will focus on PS formation in n-type silicon. The pore size distribution in PS produced by the dissolution process depends critically on whether mass transport or charge supply is the rate-limiting mechanism and the silicon doping density, which in turn affects the depletion region width (space charge region – SCR) at the interface. If the reaction rate is limited by mass transfer, characterized by current densities larger than the critical current density (J_{PS}), a surface charge of h^+ builds up and any 'hills' on the surface dissolve faster than 'troughs' because they are more exposed to the electrolyte. As a result the surface becomes smoother – electropolishing. For current densities below J_{PS}, charge transfer at the interface is the rate-limiting step, h^+ get consumed and dissolution occurs, resulting in formation of micropores over the surface. This is the case for heavily to moderately doped n-type silicon since the SCR at the interface under anodic bias is in the range of 1 nm – 50 nm and charge transfer occurs

either through tunneling (heavily doped) or charge carriers are generated through breakdown (moderately doped). The pore size and the interpore spacing scale accordingly with the SCR and micropores are formed in such a way that the SCRs of the neighboring pores overlap and the walls remain passivated. For low doped n-type silicon, the SCR is several microns thick and under anodic bias a steady state condition is reached between ionic mass transfer and charge transfer rate. This condition is characterized by the current density being equal to J_{PS} and in such a case macropores are formed over the silicon surface in line with the SCR width. The necessary h^+ for low doped n-type silicon can also be generated by illumination of the silicon substrate. A typical PS anodization cell is shown in figure 2.9. While the pores in a micro PS film tend to be branched and interconnected (Feng and Tsu 1994), the macro PS film has a parallel porous structure with pores being nucleated at random spots over the silicon surface. Using a pattern of pits over the silicon surface, generated through photolithographic and anisotropic silicon wet etching techniques one can control the position of pores in a macro PS film. The distance between neighboring pits would define the interpore spacing and therefore the pore positions over the silicon surface (Lehmann and Föll 1990). This distance is usually kept equal to or smaller than two times the SCR width to ensure that h^+ do not diffuse in between the pore walls and de-passivate them. For an n-type substrate, however this condition need not be followed strictly as the h^+ are minority carriers and even if the pits are separated by more than two times the SCR width, the hole concentration between the pore walls would be nearly equal to zero (Lehmann and Ronnebeck 1999). Figure 2.10 (a) and (b) depicts the SEM images of macropores formed in an n-type silicon substrate before and after pre-determined patterning of pits (adapted from (Lehmann 1993)).

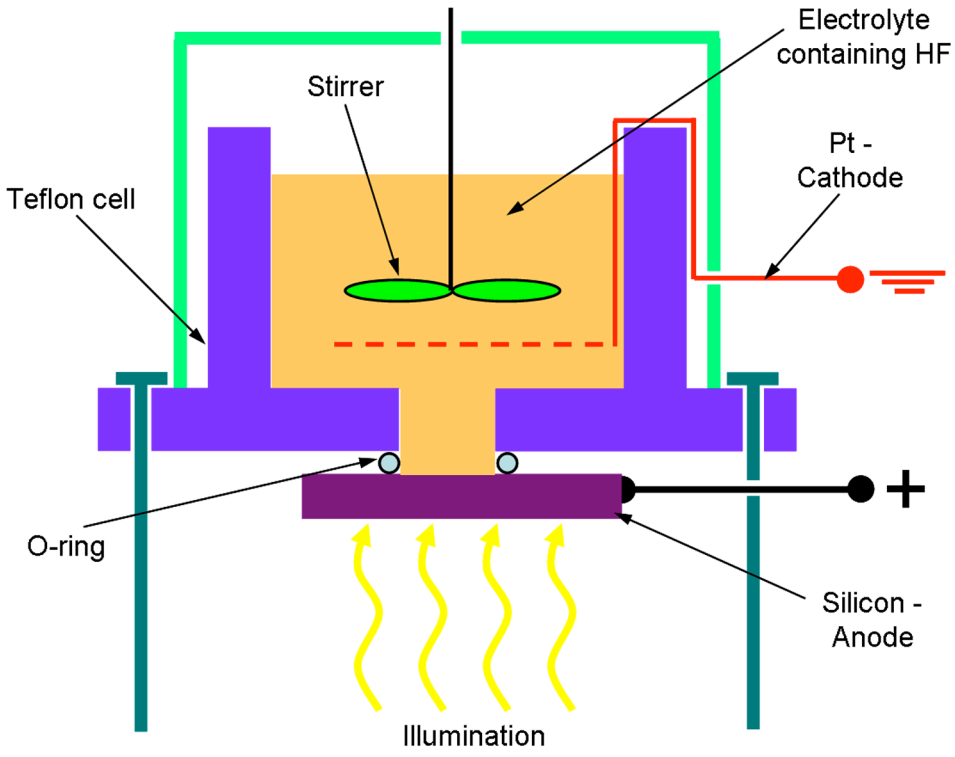

Figure 2.9 Schematic of the anodization set-up used to fabricate PS membranes.

From the viewpoint of porous membrane EO micropumps, the macro PS membrane would be an ideal choice due to its uniform and regular parallel array of pores unlike micro PS membranes. However, with regards to field effect control, the choice of macro PS membranes would be an issue. Since current leakage through the dielectric layer was observed (refer to Chapter IV for further details), a heavily doped silicon substrate would be needed to ensure that there is minimal voltage drop over the PS membrane core and the applied gate bias is dropped entirely over the dielectric layer. This would not be possible since macro PS membranes are anodized in low doped silicon substrates. Therefore an alternate method was needed to fabricate PS membranes from heavily doped silicon substrates and this was done by resorting to photolithographic and

DRIE techniques. Fabrication of PS membranes using the DRIE technique being independent of silicon doping density can therefore be used to fabricate PS membranes on silicon substrates doped to any extent.

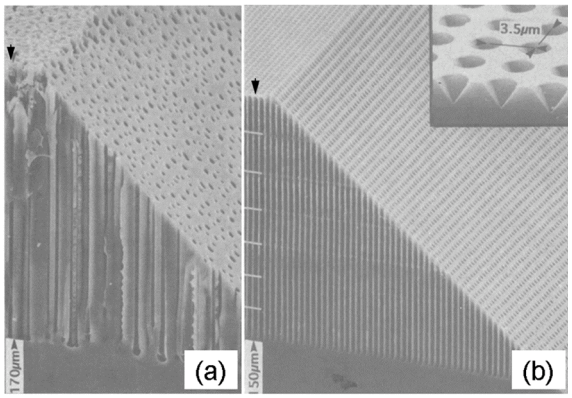

Figure 2.10 Surface and cross-section of macro PS formed in an n-type silicon sample: (a) showing a random pattern of pores, (b) showing a pre-determined pattern of pores. For this case, pore growth was induced by a regular pattern of pits produced by standard lithography and subsequent alkaline etching (inset, upper right). (Lehmann 1993)

2.2.2 PS membrane fabrication using Deep Reactive Ion Etching (DRIE)

A DRIE system works on similar lines to the ubiquitous parallel plate reactive ion etching (RIE) system with the difference being that a DRIE system generates high plasma densities ($> 10^{11}/cm^3$) while operating at low pressures (1 to 20 mTorr) in comparison to an RIE system. An ideal DRIE system has a very high etch rate (~ 3 μm/min), has selectivities to photoresists of greater than 70:1 and 150:1 for silicon dioxide, has the ability to etch deep anisotropic features, has excellent etch profile control and non-uniformities across the wafer of 5% or less (Ayon et al. 1999b; Ayon et al. 1999a). A DRIE system consists of two radio frequency (RF) power supplies operating at 13.56

MHz. One RF supply is connected to a coil surrounding the etch chamber (Inductively Coupled Plasma – ICP source). The ICP source generates electromagnetically induced electric currents leading to high density plasma and hence a high etch rate. The other RF supply is connected to the platen holding the wafer to create directional electric fields for generating anisotropic etch profiles. A DRIE system uses two distinct gas-feeding approaches: standard and time multiplexing. In the standard approach, two gases are introduced at the same time, and the etching results depend on their glow discharge. One gas is used for etching, while the other for protecting the side walls during etching. In the time-multiplexing scheme, also known as the "Bosch process" patented by Robert Bosch GmBH, Stuttgart, Germany (Laermer and Schilp 1996), the etching and passivation gases used are introduced independently, one at a time, and the tool alternates between an etching cycle and a passivation cycle. During the etch step, a shallow trench is formed in the silicon substrate within the pattern defined by the mask layer. The duration of this step is normally $\leq$ 12 secs. During the passivation cycle, a protective fluorocarbon film is deposited on all surfaces. The duration of this step is shorter than the etch step and is usually $\leq$ 10 secs. The protective film acts as a shield for the vertical sidewalls from the ensuing etch step. In the subsequent etch step, ion bombardment preferentially removes the fluorocarbon film from all horizontal surfaces, thus exposing them for further etching and hence promoting a highly anisotropic etch profile. Figure 2.11 depicts a typical DRIE system schematic. A typical composition of gases in a DRIE process consists of SF_6 for the etch cycle and C_4F_8 during the sidewall passivation cycle. Table 2.1 details the characteristics of a Bosch DRIE process and the forthcoming paragraph describes the specifics of SiN_x coated PS membrane fabrication used in this dissertation.

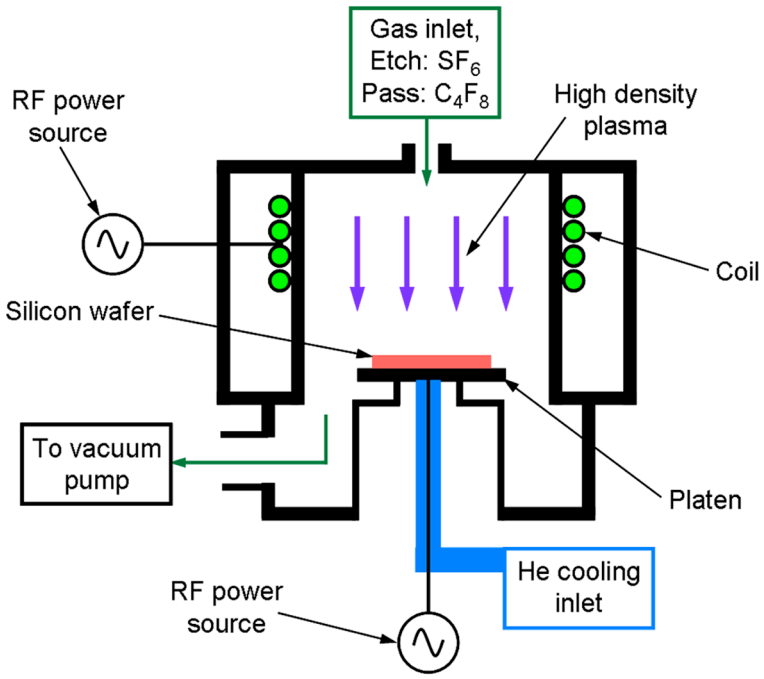

Figure 2.11 Schematic of a typical DRIE system.

SF_6 flow	30 – 150 sccm
C_4F_8 flow	20 – 100 sccm
Coil power	600 W
Platen power	10 W
Etch cycle	5 – 15 secs
Sidewall passivation cycle	5 – 12 secs
Pressure	1 – 20 mTorr
Temperature	20 – 80 °C
Etch rate	1.5 – 4 μm/min
Sidewall angle	90° ± 2°
Selectivity to photoresist	~ 100 to 1
Selectivity to silicon dioxide	~ 200 to 1

Table 2.1 Typical characteristics of a Bosch DRIE process. (Maluf 1999)

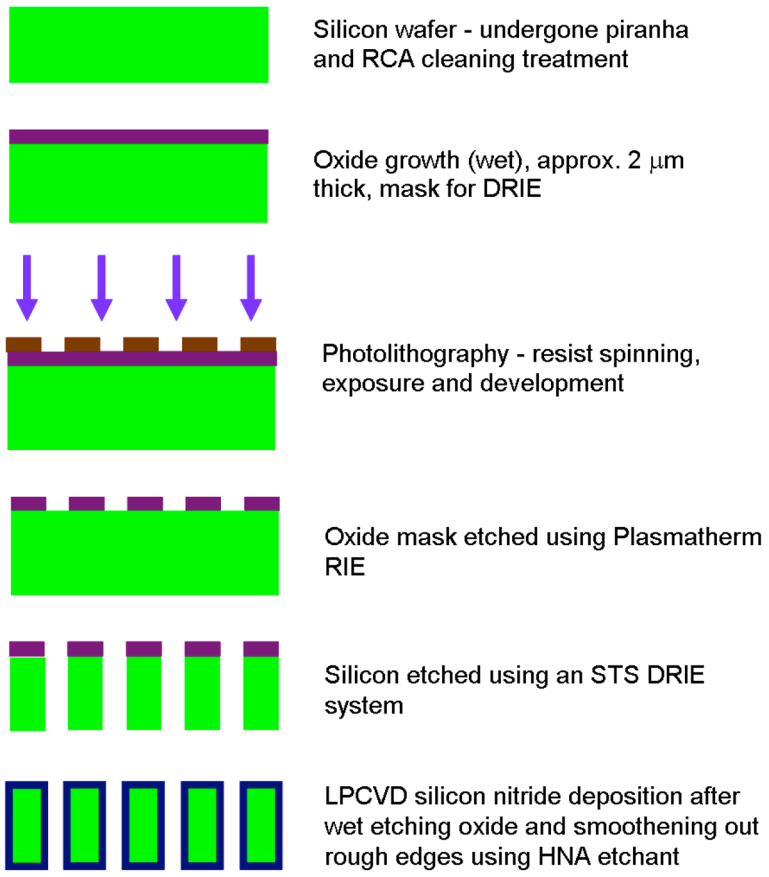

Figure 2.12 Stepwise fabrication of SiN_x coated PS membranes.

All microfabrication work described here was carried out at the Microelectronic Research Center (MiRC), Georgia Institute of Technology, Atlanta, GA. The silicon wafers were thoroughly cleaned using standard wafer cleaning processes, i.e. SC-2 and piranha clean process to remove any metallic contaminants and organic residues respectively. This was followed by a wet oxide etch using buffered-oxide-etch (BOE) solution. The cleaned silicon wafers were then wet-oxidized in a TYTAN oxidation furnace system (Tystar Corporation, CA) to grow a 2 μm thick SiO_2. Following oxidation, the wafers were patterned using standard photolithographic techniques.

Microposit SC 1827 (Shipley, Marlborough, MA), a positive thick film photoresist, was spin-coated onto the wafers to have a film thickness of approximately 2.7 μm. This film and the SiO_2 layer underneath acted as the masking layer for oxide etching and deep silicon etching to be performed in the subsequent steps. The wafers were then exposed using a photomask and Karl-Suss MA-6 mask aligner and the pattern was developed. The pattern details are as follows: an array of 15 μm × 40 μm rectangles with a pitch of 35 μm along the breadth and 70 μm along the length of the rectangle. The array measured 5 mm × 5 mm in dimensions. Nine such arrays were patterned onto a single 4″ silicon wafer. Following the development of the pattern, the wafers were dry etched using a Plasmatherm (Plasma-Therm, Inc., FL) ICP RIE to etch the SiO_2 and expose the silicon inside each rectangular pattern of the array. This was followed by DRIE of the exposed silicon using the Surface Technology Systems (STS plc, UK) ICP deep silicon etcher resulting in rectangular channels/pores running all the way through the silicon wafer. The wafers were immersed in acetone to wash away any remnant photoresist and then immersed in BOE to etch away the remaining SiO_2 masking layer. To round off the sharp edges created as a result of dry etching, the wafers were immersed in an isotropic wet silicon etchant comprising of hydrofluoric acid, nitric acid and acetic acid (HNA). Following this step the wafers were undertaken through the standard wafer cleaning processes again prior to SiN_x deposition. SiN_x was deposited using the low-pressure chemical vapor deposition (LPCVD) technique in a TYTAN nitride deposition furnace system (Tystar Corporation, CA). This resulted in a conformal coating of low stress SiN_x, 500 nm thick, over the entire pattern. The wafers were then diced into nine individual chips, each chip containing one array. Figure 2.12 details the stepwise fabrication process

schematically. Figure 2.13 depicts the SEM images of the silicon chip with zoomed in views of the rectangular pores.

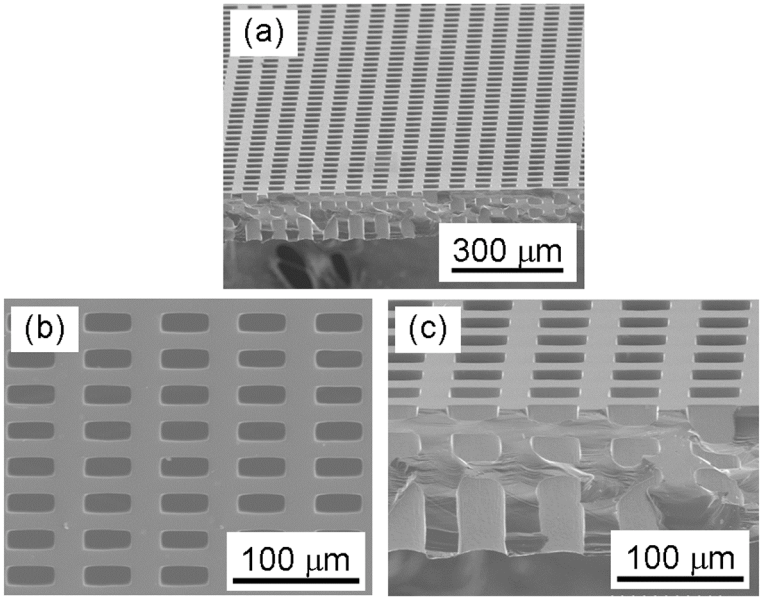

Figure 2.13 Scanning electron micrograph of the entire SiN_x coated porous silicon membrane (a). Zoomed-in views of the membrane surface (b) and cross-section (c). The cross-section image shows irregular features running across the pores. These are part of the silicon core and appear because of the way the membrane is chipped.

2.3 Summary

This chapter puts forth and discusses briefly the different techniques that can be used to fabricate porous membranes from aluminum oxide and silicon substrates. It further goes on to describe in detail the different methods that were primarily used for fabricating PAA and PS membranes. While PAA membranes can be made using MA and HA processes, the MA process was preferred over the latter due to its relatively easier setup configuration and use of lower anodization voltages. For PS membranes, since current leakage through the dielectric layer was an issue, DRIE technique was favored over

electrochemical anodization because it provided freedom for using a heavily doped silicon substrate for fabricating PS membranes, which was a limiting factor for the electrochemical anodization technique.

CHAPTER III

SiO_2 COATED POROUS ANODIC ALUMINA MEMBRANES FOR HIGH FLOWRATE ELECTRO-OSMOTIC PUMPING

This chapter describes the work on in-house fabricated SiO_2-coated porous anodic alumina (PAA) membranes and their characterization for high flowrate EO pumping under low effective applied voltages. With EO pumping being extensively used as one of the primary fluid driving forces in lab-on-a-chip devices and in micropumps for microelectronic cooling, a pump with high flowrate per unit area, operating at low effective applied voltage would be of prime importance for efficient operation. High quality porous alumina membranes of controllable pore diameters in the range of 30-100 nm and pore lengths of 60-100 μm were fabricated in-house by electrochemical anodization. The pores are straight, uniform and hexagonally close-packed with a high porosity of up to 50 % of the total area. The inner surface of the pore was coated conformally with a thin layer (~ 5 nm) of SiO_2 to achieve a high zeta potential. The EO pumping performance of the fabricated anodic alumina membranes, coated and uncoated, was investigated using standard relevant aqueous electrolyte buffer solutions. The high zeta potential of the SiO_2 coating increases the pumping flowrate even though the coating reduces the porosity of the membrane. Results show that nanostructured SiO_2-coated porous anodic alumina membranes can provide a normalized flowrate of 0.125 $ml/min/V/cm^2$ under a low effective applied voltage of 3 V. This compares favorably with other porous materials such as glass frits.

3.1 Theoretical Background

A model for treating EO flow in a porous media has been suggested by Mazur and Overbeek wherein the tortuous microchannels with circular cross section were assumed to have equal pore radii, a, and an equal value of zeta potential, ζ (Mazur and Overbeek 1951). They derived a set of flow equations depicting EO flow in porous structures. A similar set of equations were derived by Rice and Whitehead in their theoretical study of EO flow in a narrow cylindrical capillary (Rice and Whitehead 1965). Implicitly, in terms of the electrical potential within the pore, the general velocity profile within the circular cross-section of the pore with a high aspect ratio (pore axial length to pore radius ratio) is obtained from the Navier-Stokes equations and the continuity equation as

$$u(r) = \frac{P_x}{4\mu}\left(a^2 - r^2\right) - \frac{\varepsilon\varepsilon_o\zeta E_x}{\mu}\left[1 - \frac{\psi(r)}{\zeta}\right]. \tag{3.1}$$

Here $P_x = \Delta P/L$ is the streamwise pressure gradient within the pores; $E_x = V_{eff}/L$ is the streamwise electric field within the pores; ΔP is the pressure drop within the pores; V_{eff} is the effective voltage drop across the membrane; L is the total physical pump length for flow and $\psi(r)$ is the potential distribution within the pores.

This velocity profile when integrated over the cross-sectional area, A, and L, yields the flowrate for the entire porous membrane as

$$Q = \frac{\phi}{\tau}\left(-\frac{\Delta P A a^2}{8\mu L} - \frac{\varepsilon\varepsilon_o\zeta A V_{eff}}{\mu L} f\right), \tag{3.2}$$

where f is an integral of the form

$$f = \int_0^a \left(1 - \frac{\psi}{\zeta}\right)\frac{2r}{a^2}dr. \tag{3.3}$$

Here φ is the porosity of the porous membrane and τ is the tortuosity defined as square of the ratio of the effective total length of zigzag microchannels to the physical pump length. The porosity of a hexagonal structure is given as

$$\phi = \frac{2\pi}{\sqrt{3}}\left(\frac{a}{D_{\text{int}}}\right)^2, \tag{3.4}$$

where D_{int} is the interpore distance (Nielsch et al. 2002). Using equation 3.4 and the pore dimensions, the porosity of the as-fabricated PAA membrane was calculated to be about 50%. The tortuosity is given as

$$\tau = \left(\frac{L_e}{L}\right)^2, \tag{3.5}$$

where L_e is the effective total zigzag length of the pores (Yao and Santiago 2003). Since the pores are perfectly parallel to each other in a PAA membrane, this tortuosity factor turns out to be unity for this membrane. The parameter f in equations (3.2) and (3.3) approaches to unity for a large pore diameter to Debye length ratio ($a/\lambda = \kappa a$ = electrokinetic radius, $\kappa = 1/\lambda$, λ = Debye length = characteristic thickness of the EDL) (R. J. Hunter 1981; Yao and Santiago 2003).

Equations (3.2) and (3.3) can be used to theoretically calculate the EO flowrate through a porous membrane. However, caution must be used to interpret the theoretical prediction from these equations since they are based on continuum theory, which may not be accurate for high zeta potentials. This is especially true if the potential in the pore, ψ in equation (3.3), is obtained by solving the Poisson-Boltzmann equation with the Debye-Hückel approximation, which is only valid for low to moderate zeta potentials below 25 mV (R. J. Hunter 1981). Since the PAA membrane surfaces were coated with SiO_2,

whose zeta potential is generally on the order of 100 mV (Yao et al. 2003), the symmetric electrolyte approximation suggested by Hunter (R. J. Hunter 1981) was used. According to this approximation, for high zeta potential surfaces, an unsymmetric electrolyte can be treated as being symmetric having the properties of the counter-ion without incurring much error. For the range of buffer concentrations used in this study, the zeta potential for SiO_2 has been reported to be 65 mV-110 mV at a solution of pH ~ 9 (Scales et al. 1992; Yao and Santiago 2003; Yao et al. 2006). Hence for all experiments on PAA membranes the buffer solutions have been treated as symmetric and having the properties of sodium ion from the sodium tetraborate buffer.

3.2 Fabrication of PAA Membranes

The fabrication of PAA membranes will not be dealt with in detail here as it has been described in the previous chapter. However, the details pertaining to SiO_2 coating process over these membranes will be furnished in this section. Post-PAA membrane fabrication, the pore walls were coated with a thin layer (approximately 5 nm thick) of SiO_2 for the purpose of achieving a high zeta potential. This was done using surface sol-gel synthesis technique (N. I. Kovtyukhova et al. 2003) involving adsorption, hydrolysis and washing of each aluminum oxide membrane. Briefly, each membrane was immersed in a silicon tetrachloride ($SiCl_4$) solution diluted with carbon tetrachloride (CCl_4) (60% by volume) for 6 mins and followed by a rinse in a fresh solution of CCl_4 for 5 mins to wash off non-reacted $SiCl_4$ from the membrane surface. The membrane was then transferred to another beaker containing a fresh solution of CCl_4 for 25 mins to remove any unbound $SiCl_4$ from within the pores. Following this, the membrane was soaked in a

CCl_4 and methanol (MeOH) mixture (1:1) for 5 mins and ethanol (EtOH) for 10 mins to remove CCl_4 and then dried in an argon stream. Then the membrane was immersed in deionized (DI) water for 10 mins to complete the hydrolysis of $SiCl_4$ to SiO_2, followed by immersion in MeOH for 5 mins and then drying in an argon stream. The hydrolysis reaction is as follows (Ramsden 2000)

$$SiCl_4\ (l) + 2H_2O\ (l) \rightarrow SiO_2\ (s) + 4HCl\ (g).$$

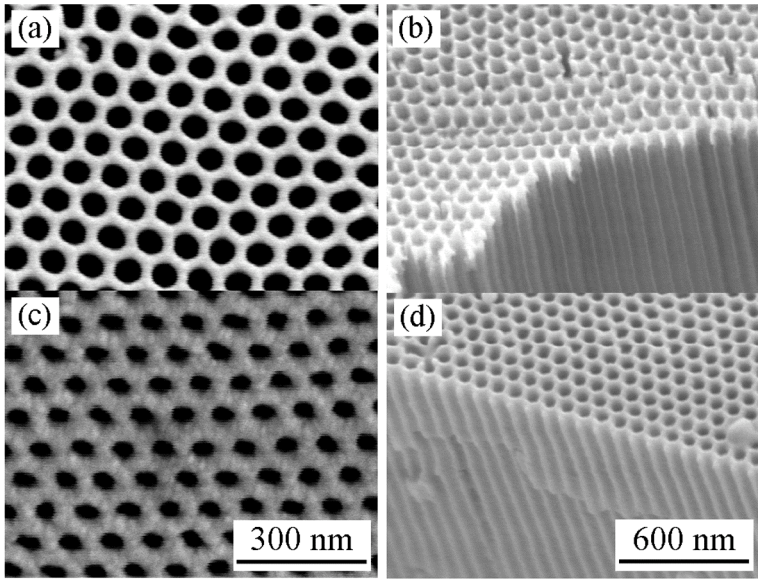

Figure 3.1 SEM images of the MA PAA membrane before going through the SiO_2 coating process: (a) and (b); and after completion of the process: (c) and (d).

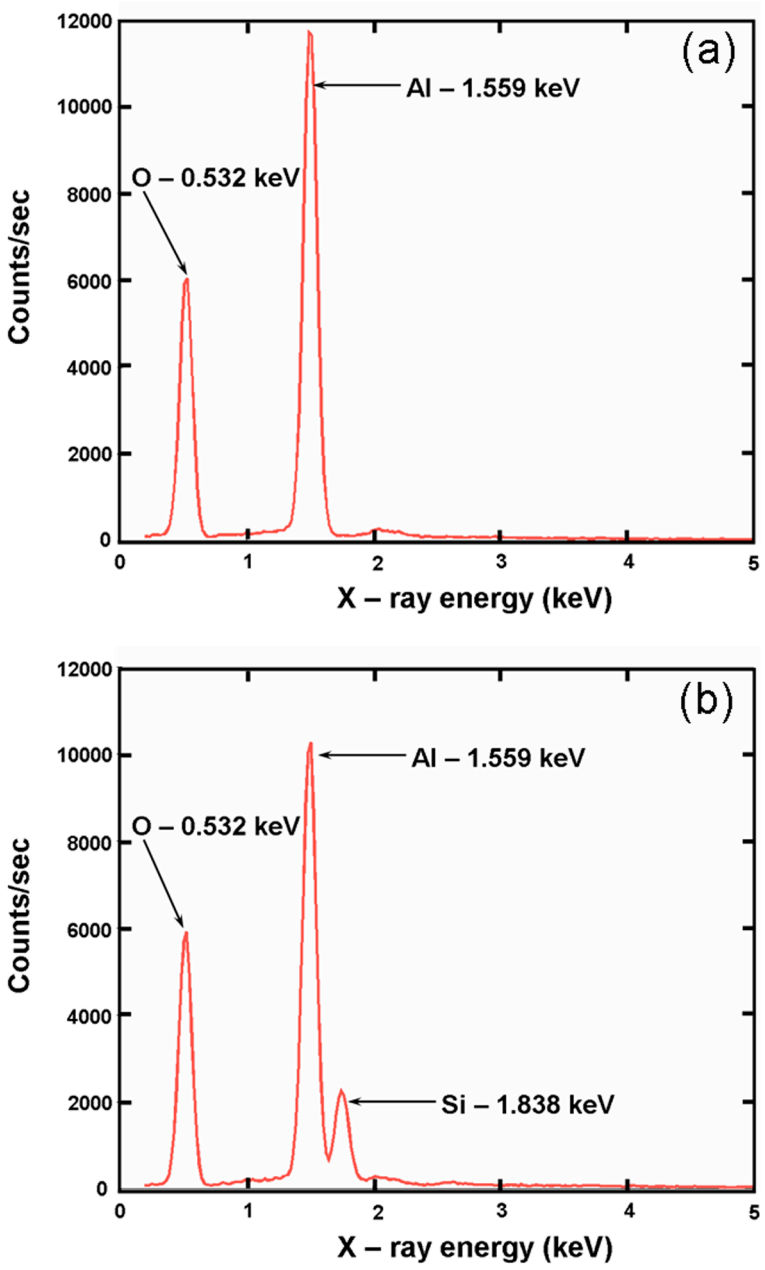

Figure 3.2 EDX spectra of (a) uncoated and (b) SiO_2 coated PAA membrane.

Each membrane was taken through five cycles of the coating process to ensure that the inner wall of the pore was completely covered with the SiO_2 layer. A stream of argon was used to envelope the membrane while transferring it from one beaker to the

other during the coating process to prevent the $SiCl_4$ from getting hydrolyzed with moisture in air. Figure 3.1 shows the PAA membrane viewed before and after the SiO_2 coating process. The thickness of PAA membranes after the coating process was still 90±5 μm but the pore diameter was reduced to 70±5 nm, as measured with a SEM. Additionally, energy dispersive X-ray (EDX) analysis was conducted on the coated and uncoated PAA membranes to further confirm the presence of SiO_2 over the membrane surface. Figure 3.2 (a) shows the EDX spectra indicating the presence of Al and O with an additional peak in figure 3.2 (b) corresponding to Si.

3.3 Experimental Details for Characterization of EO Flowrate

3.3.1 Experimental Set-up

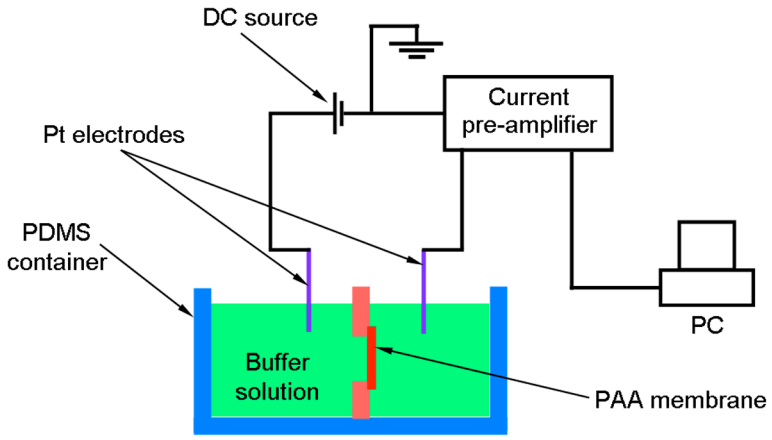

Figure 3.3 Schematic of the experimental set-up for pumping flowrate characterization.

The experimental setup for pumping flowrate characterization is depicted in the schematic shown in figure 3.3. An Agilent power supply (Agilent Technologies, E3612A) was used as the power source for pump operation. Platinum electrodes were

used for both cathode and anode. The current signal was recorded through a current pre-amplifier (DL Instruments, Model 1211) and transferred to a computer using an automated data acquisition system comprising of a data acquisition card (National Instruments, 6052t), a BNC terminal break-out box and LabView software (National Instruments Corporation).

The PAA membrane was mounted over a 1 mm thick glass slide inserted in the center of a container made of PDMS and held in place using silicone sealant. The glass slide had a 6.35 mm diameter hole in the center to expose the membrane to the electrolyte on the upstream side. For the downstream side the membrane surface was covered with colorless nail polish (acetate and nitrocellulose based formulation) leaving a 6.35 mm diameter area in the center coinciding with the hole in the glass slide.

3.3.2 Distribution of Applied Electric Potentials

The pumping setup designed here for our experiment was such that all of the applied electric potential, V_{app}, supplied by the power supply was not experienced by the membrane, but only a part of it, V_{eff}. This was due to the fact that V_{app} would get distributed as V_{dec}, the decomposition potential associated with the electrode reactions at the electrode/electrolyte interface and the combined potential drop of $(2R_b+R_h+R_m)I$. Here R_b is the resistance of the region from the electrode to the glass slide on either side; R_h is resistance of the region within the hole on the glass slide immediately adjoining the membrane; R_m is the resistance of the PAA membrane; and I is the system current. Yao et. al. conducted a calibration experiment and estimated the value of V_{dec} to be around 4.5 V for the platinum electrode/borate buffer combination (Yao et al. 2003). Based on the I-

V relation $V_{app} - V_{dec} = (2R_b + R_h + R_m)I$, V_{dec} can be determined with two different applied voltages and correspondingly measured currents. The value of V_{dec} so obtained was around 4 V and the value determined for each run was used for the data reduction. The resistance $2R_b+R_h$, and R_m were also measured by conducting a blank run (without the membrane mounted) and a full run (with the membrane mounted) at an applied voltage for each run. The range of the effective electric fields across PAA membranes selected was between 0.01 V/μm (~1 V across the PAA membrane) and 0.1 V/μm (~9 V across the PAA membrane), which was comparable to the values reported in literature.

3.3.3 Selection of Buffer Solutions

EO pumps reported in literature have operated on buffered aqueous electrolytes prepared by using DI water or DI water itself (C. H. Chen and Santiago 2002; Gan et al. 2000; Yao et al. 2003; Zeng et al. 2001; Zeng et al. 2002). From the viewpoint of practical microcooling systems, buffered DI water has been used as an effective cooling medium in a closed loop EO microchannel cooling system for VLSI circuits (Jiang et al. 2002). In this dissertation, for all pumping experiments on PAA membranes the working fluid was an aqueous borate buffer ($Na_2B_4O_7$) based on sodium ion (Na^+) concentration varying from 0.1 mM to 7.5 mM with a pH ~ 9. The range of buffer concentrations used and the measured conductivity corresponding to each concentration is tabulated in table 3.1. The pH and conductivity of the electrolyte was measured using a pH meter (Accumet AB15 Basic) and a conductivity meter (Oakton CON 11 series).

Buffer Concentration (mM)	Conductivity (S/m)
0.1	1.075e-3
0.25	2.49e-3
0.5	4.7e-3
0.75	6.9e-3
1	9.02e-3
2.5	2.15e-2
5	4.15e-2
7.5	6.10e-2

Table 3.1 Range of standard buffer concentrations used in experiments.

3.3.4 Experimental Procedure

Freshly prepared membranes were mounted and rinsed thoroughly with DI water by filling both sides of the PDMS container with DI water and agitating the water over the membrane surface. The membrane was then primed electro-osmotically by filling the container with the buffer solution of a particular concentration to be used for testing and applying a small voltage across the electrodes for approximately 30 – 45 min. During the experiments, the upstream side of the container was filled with a known volume of buffer solution and allowed to flow through the pores to the other side through capillary forces. The downstream side was then filled with an equal volume of the buffer solution. The combination of capillary filling, agitation, and priming ensures that all the channels in the PAA membrane are free of ionic contaminants and are filled with the testing solution. In the event of testing a solution of a different concentration, a similar cleaning procedure was employed except that after cleaning the membrane with DI water agitation, DI water

was passed electro-osmotically through the channels. Decay was observed in the measured ionic current indicating the removal of ionic species from the previous run. The cleaning was carried out until a steady ionic current was observed followed by EO priming of the channels with the new test solution.

The pumping flowrate was measured based on the mass difference of the electrolyte between the downstream and upstream fluid reservoir and the pumping time. An Acculab mass balance (Acculab, VI-3mg) was used to measure the mass of the electrolyte on either side. This was done by first weighing the container with both sides filled to give mass W_1, emptying and drying the downstream side of the container after the run and weighing again to give mass W_2, and then weighing the empty container to give mass W_3. The mass differences (W_1-W_2) and (W_2-W_3) correspond to the mass of the downstream side and upstream side, respectively. The total pumped mass is then half the difference between the weights of the downstream and upstream side. The pumping time was measured using a stopwatch.

3.4 Results and Discussions

Pumping flowrates for PAA membranes were characterized, both with and without SiO_2-coating under different effective applied voltages. With SiO_2-coated PAA membranes, a high normalized pumping flowrate per unit membrane area per applied voltage under a low effective applied voltage was achieved. The uncoated PAA membranes have a higher porosity than the SiO_2-coated PAA membranes, but lower pumping flowrates. Moreover, the pumping flowrates for the uncoated membranes showed a non-linear flowrate versus effective applied voltage behavior under some

conditions.

3.4.1 Pumping Flowrate Characterization for SiO_2-coated Membranes

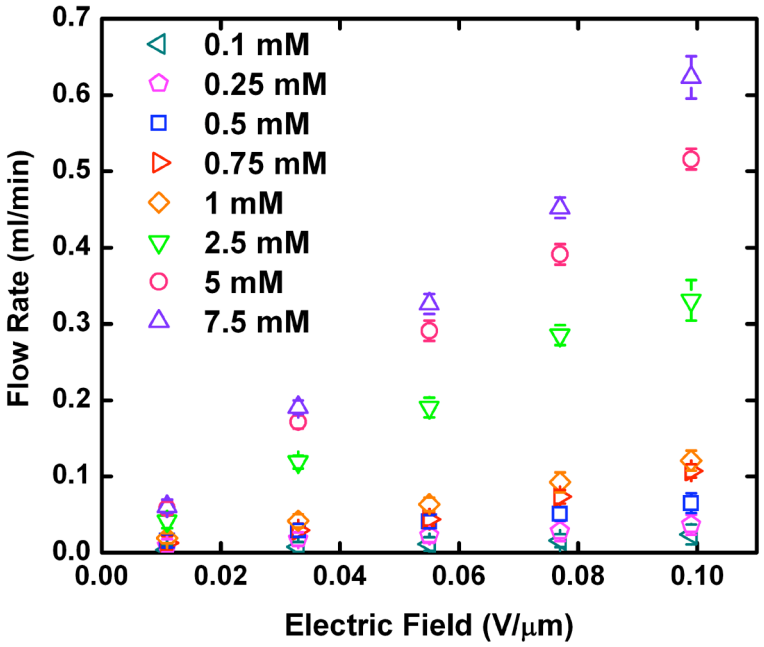

Figure 3.4 Flowrate versus electric field for SiO_2-coated PAA membranes at different buffer concentrations.

Figure 3.4 shows the pump performance based on flowrate measured at different effective applied electric fields for the different concentration buffers used in this work. The flowrates show a linear increasing trend with increasing electric field, as expected. In addition, as the buffer concentration increased, the pumping flowrate increased. There are larger experimental uncertainties for high concentration electrolytes (5 mM, 7.5 mM) under high total applied voltages (> 50 V). In this case, we observed that the measured current from the pre-amplifier was not very stable (the fluctuation is about 10-20% of the

baseline current), probably due to the disturbance from gas bubble formation at the electrodes from the electrodic reactions. At lower buffer concentrations and applied voltages, this problem was not encountered. Therefore a maximum flowrate was obtained within the regime where the measured current was stable, which in this case was achieved using a buffer solution of 2.5 mM concentration operating at a total applied voltage of 40 V.

A good figure of merit for the pumping performance of different materials is the normalized flowrate in the unit of milliliter per minute per voltage per unit area. Figure 3.5 shows the comparison of the maximum flowrate achieved in this study along with EO flowrates that have been reported in literature within the past decade. Within the regime where the measured current is stable, based on the effective voltage drop across the membrane, the normalized flowrate obtained in this work is 0.125 ml/min/V/cm^2. This is higher than the flowrates of most other micro EO pumps reported in literature (Laser and Santiago 2004) by a factor of at least two, and often higher by orders of magnitude. The only comparable normalized flowrate reported is for an EO pump made of porous silicon (Yao et al. 2006).

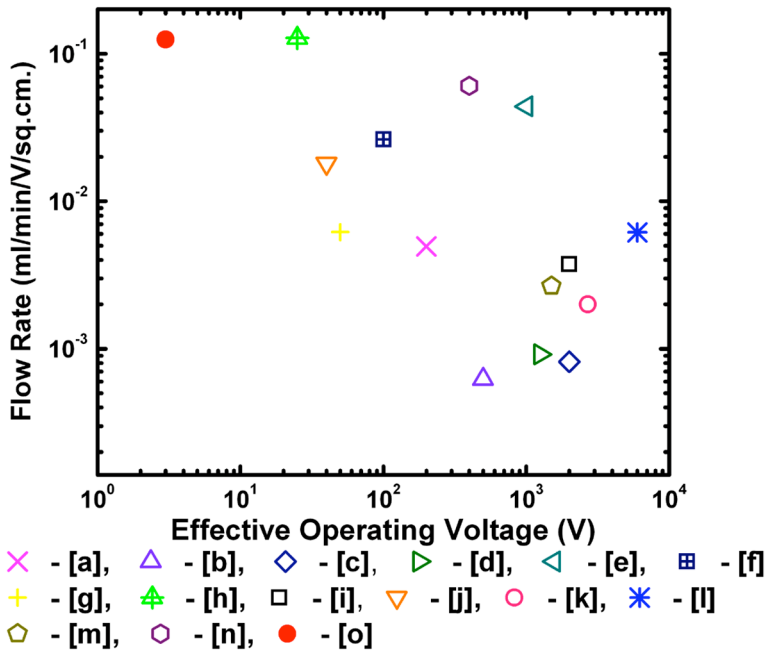

Figure 3.5 Comparison of the EO flowrate obtained from SiO_2-coated PAA membranes against flowrates reported in literature. The flowrate for the coated PAA membrane is based on the effective voltage across the membrane.

[a] - (Jiang et al. 2002); [b] - (Gan et al. 2000); [c] - (Zeng et al. 2001); [d] - (Zeng et al. 2002); [e] - (C. H. Chen and Santiago 2002); [f] - (Yao et al. 2003); [g] - (Tripp et al. 2004); [h] - (Yao et al. 2006); [i] - (Ramsey and Ramsey 1997); [j] - (McKnight et al. 2001); [k] - (Jacobson et al. 1994); [l] - (Wang et al. 2006); [m] - (Guenat et al. 2001); [n] - (Laser et al. 2003); [o] - (Vajandar et al. 2007)

In addition to the high flowrate, it is worth noting that the flowrate was achieved using a far lower effective voltage. This is very important for low voltage applications. A point to clarify is that for the flowrates reported in literature, the voltage used for normalization is based on the actual applied voltage instead of effective voltage as was

used for the calculation here. The relatively large thickness of the membranes used in other pumps posed the dominant electrical resistance in the system and therefore the total applied voltage drop across the thick membranes was nearly the same as the effective voltage. The high normalized flowrate achieved using SiO_2-coated PAA membranes can be attributed to the high porosity, low tortuosity and uniform pore diameter for the PAA membrane and the low effective operation voltage is due to the small thickness of the PAA membrane. The simple and cost-effective fabrication of a PAA membrane also makes it attractive for EO pumping applications.

It is known that zeta potential varies inversely with ionic concentration (Arulanandam and Li 2000; R. J. Hunter 1981; Kirby and Hasselbrink 2004) though the dependence is a weak one (D. Q. Li 2004). Thus a slightly higher flowrate should be expected at lower buffer concentrations due to the increase in zeta potential. However an exactly opposite trend was observed as shown in figure 3.4. The reason is that for nanochannels, the channel diameter is comparable to the Debye length, λ. As reported by Rice and Whitehead, the volume transported per unit area and unit time decreases in the region $1 < \kappa a \leq 10$ as the double layer thickness becomes comparable to the channel diameter and eventually overlaps (accounted for by the integral f in equation (3.2)), with the velocity profile taking on a Poisseuille form for $\kappa a \leq 2$ (Rice and Whitehead 1965). A plot of the measured flowrate against log κa at three different V_{eff} demonstrates this trend and is shown in figure 3.6. The pumping flowrate increases as κa increases since the combination of a and the electrolyte concentration results in κa being in the region of $1 < \kappa a \leq 10$ for PAA membranes.

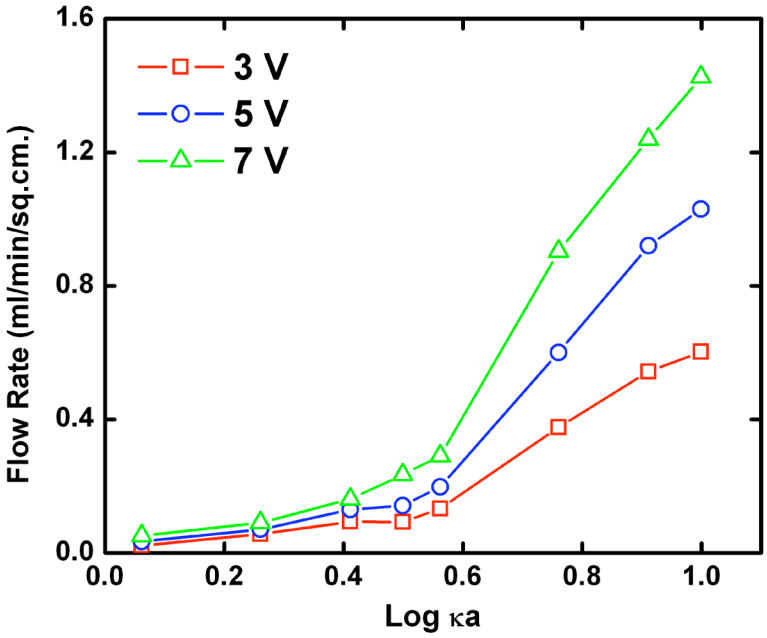

Figure 3.6 Flowrate as a function of electro-kinetic radius for three different effective voltages.

It is an established fact that surface charge governs ionic transport in nanofluidic channels at low solution concentrations, i.e., the electrical conductance of the solution saturates at a value independent of solution concentration (Stein et al. 2004). To examine this effect on the EO flowrate of SiO_2-coated PAA membranes, the flowrate-κa plot (figure 3.6) was extended further to lower solution concentrations (concentration < 0.1 mM) for the case of 3 V. Figure 3.7 depicts the plot of EO flowrate versus log κa for solution concentration 1 mM and below.

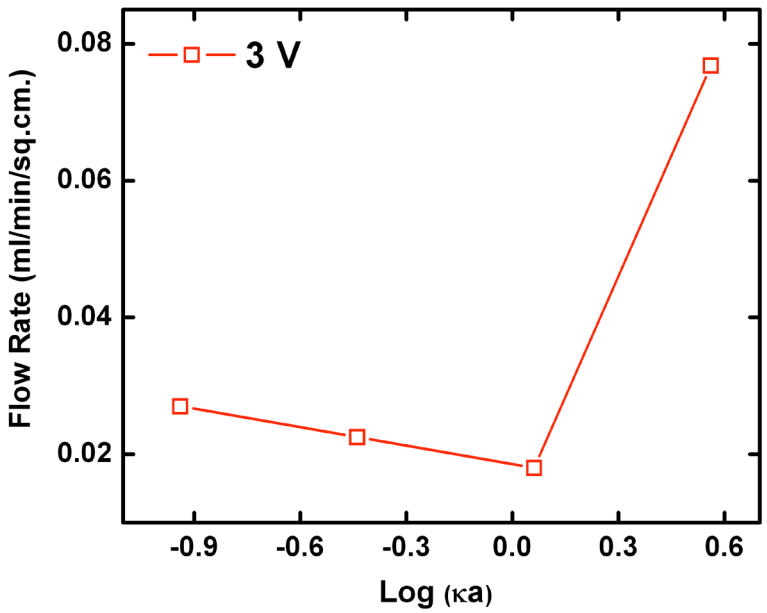

Figure 3.7 Flowrate versus electro-kinetic radius for lower buffer concentrations (< 1 mM) measured at 3 V.

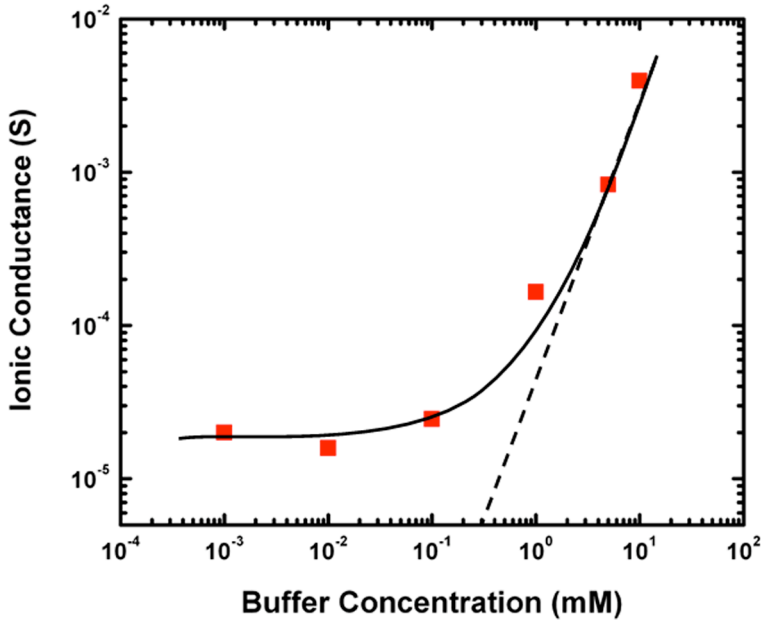

Figure 3.8 Measured ionic conductance (solid curve) of silica coated PAA membrane depicting the deviation from bulk behavior (dashed line) at low concentrations.

It can be seen from figure 3.7 that the flowrate shows a marginal increase for concentration below 0.1 mM (negative values of κa). We believe that the reason for this increase can be attributed to the surface charge governed ionic transport and high surface charge density of the SiO_2 coated PAA membranes at these concentrations. The negative surface charge density of SiO_2 surface arises from the density of SiO^- groups present on its surface, which in turn is a function of the buffer solution pH (Papirer 2000). Additionally the sodium borate buffer used for these experiments has a basic nature due to the hydrolysis of the conjugate base ($B_4O_7^{-2}$ in this case). The hydrolysis reaction produces OH^- ions, which gives the buffer solution its basic nature. At low salt concentrations the OH^- ion concentration is lowered thus lowering the pH of the solution. Therefore to maintain a pH of around 9, sodium hydroxide (a strong base) was added while preparing the buffer solution. The addition of the base increases the OH^- ion concentration in the solution. This prevents the SiO^- groups from getting protonated to neutral SiOH and thereby maintains a high surface charge density for the SiO_2 surface. Moreover the ionic conductance in the pores also follows the expected trend at low solution concentrations corroborating surface charge dominated transport in PAA membranes. It should be noted here that the conductance measurement using a porous membrane yields a higher and therefore a more precise value of conductance as compared to conductance measurements on single nanochannels. This is because each pore in the PAA membrane is parallel to each other and the parallel conductance adds up to give a higher equivalent conductance. Figure 3.8 shows the measured ionic conductance. The solid curve in the figure depicts the deviation of ionic conductance from bulk behavior (dashed line) at low salt concentrations.

A check on the pumping flowrate indicates that the predicted flowrates using equations (3.2) and (3.3) can be several times higher than the experimental results. For the 2.5 mM buffer the predicted flowrate is approximately 8 times more than the measured value, while the discrepancy is lower for 5 mM (5.4 times) and 7.5 mM (4.8 times) buffer solutions. One possible reason is that we used the high limit of the zeta potential for SiO_2 in the calculations (110 mV), while the sol-gel coated SiO_2 may have a lower zeta potential. A more possible reason is that in our calculation, the electrical potential distribution in the channel, ψ in equation (3.3), is modeled based on the Debye-Hückel theory, which is only strictly valid for low to moderate zeta potentials below 25 mV (Rice and Whitehead 1965; Yao and Santiago 2003), while the zeta potential of SiO_2 is usually much higher. A recent molecular dynamics simulation by Qiao and Aluru suggested that for high surface charge density, which corresponds to high zeta potentials, the continuum theory that equations (3.2) and (3.3) were based on could overestimate the EO flow significantly (Qiao and Aluru 2005). For example, for a surface charge density of 0.1 C/m^2, which corresponds to the upper limit of the oxide surface charge density (Karnik et al. 2005), the continuum theory predicts an EO flow mobility that is more than five times of that from molecular dynamics simulation. This indicates that the prediction based on the continuum theory, i.e., equations (3.2) and (3.3), may not be feasible to be used for quantitative flowrate calculations for a channel with an oxide surface of high zeta potential.

Other factors one might think of could include the back pressure effect on the overall measured flowrate as the fluid is being pumped, or the symmetric electrolyte approximation taken into account here and pore diameter variations along the length of

the pore. To avoid error from evaporation in the experiment, the run times were kept short (3 to 5 minutes, depending on the flowrate), and the maximum surface level difference between the two reservoirs was around 0.2 cm because of the relatively large surface area of the reservoir. This liquid level difference leads to a back pressure value of about 20 Pa giving rise to a reverse flowrate of around 2.4×10^{-5} ml/min, which is negligible compared to the measured pumping flowrates on the order of 0.1 ml/min. Therefore, it is fair to assume that the back pressure has a negligible effect on the overall measured flowrate (~ 0.01%), and hence can be ruled out. The symmetric electrolyte approximation is a well documented fact (R. J. Hunter 1981; Yao and Santiago 2003) and should hold well in this case since the zeta potential for the range of buffer concentrations used is reported to be 65 mV-110 mV at a solution of pH ~ 9 (Scales et al. 1992; Yao and Santiago 2003; Yao et al. 2006), unless the sol-gel coated SiO_2 has a much lower zeta potential. The laboratory fabricated PAA membranes are known to have an excellent uniformity in diameter of pores as verified by SEM observations and as reported in literature (Asoh et al. 2001; W. Chen et al. 2005a; A. P. Li et al. 1999; Masuda and Fukuda 1995; Masuda and Satoh 1996), and therefore pore diameter variations as being one of the factors responsible for the discrepancy can be eliminated. Also it is not likely that this discrepancy is caused by the possibility that the membrane is not completely wetted by the solution since the flowrate for each case was measured two to three times with consistent results. This would not be true if the percentage of membrane that was wetted was not 100% and varied from run to run.

3.4.2 Pumping Flowrate Characterization for Uncoated Membranes

In addition to testing the SiO_2-coated PAA membranes for their EO pumping performance, the uncoated PAA membranes were also tested to see if a similar pumping behavior is observed. It has been reported that alumina surface exhibits a negative zeta potential in the presence of an aqueous solution of pH ~ 9 (Sprycha 1989). Hence the buffer solution composition, pH, and concentrations were unchanged from those used for the coated PAA membranes. For the range of buffer concentrations used here the zeta potential value for the uncoated PAA membrane surface has been reported to be 15 mV-35 mV (Sprycha 1989), which is lower than that of SiO_2 surfaces. Though the porosity of the uncoated porous alumina is 1.3 times that of SiO_2-coated membranes, a lower flowrate is still expected for the same range of effective applied electric fields due to the low zeta potential. In addition, a similar linear increasing trend with the effective applied electric field should be expected.

Lower flowrates were observed; however, the trend is not linear with increasing electric field, which is unexpected as shown in figure 3.9. At lower fields ($\leq$ 0.03 V/μm) the flowrate increases linearly with the effective applied field for all ranges of buffer concentrations used. However at higher fields (> 0.03 V/μm) the flowrate deviates from linearity for buffer concentrations in the range of 0.1 mM to 2.5 mM. For the buffer concentration of 2.5 mM, the deviation from linearity is much more drastic showing a "hump" like feature. More interestingly, for 5 mM and 7.5 mM the flowrate shows a linear trend all the way through. The abnormal behavior was maintained on repetitions with different PAA membranes.

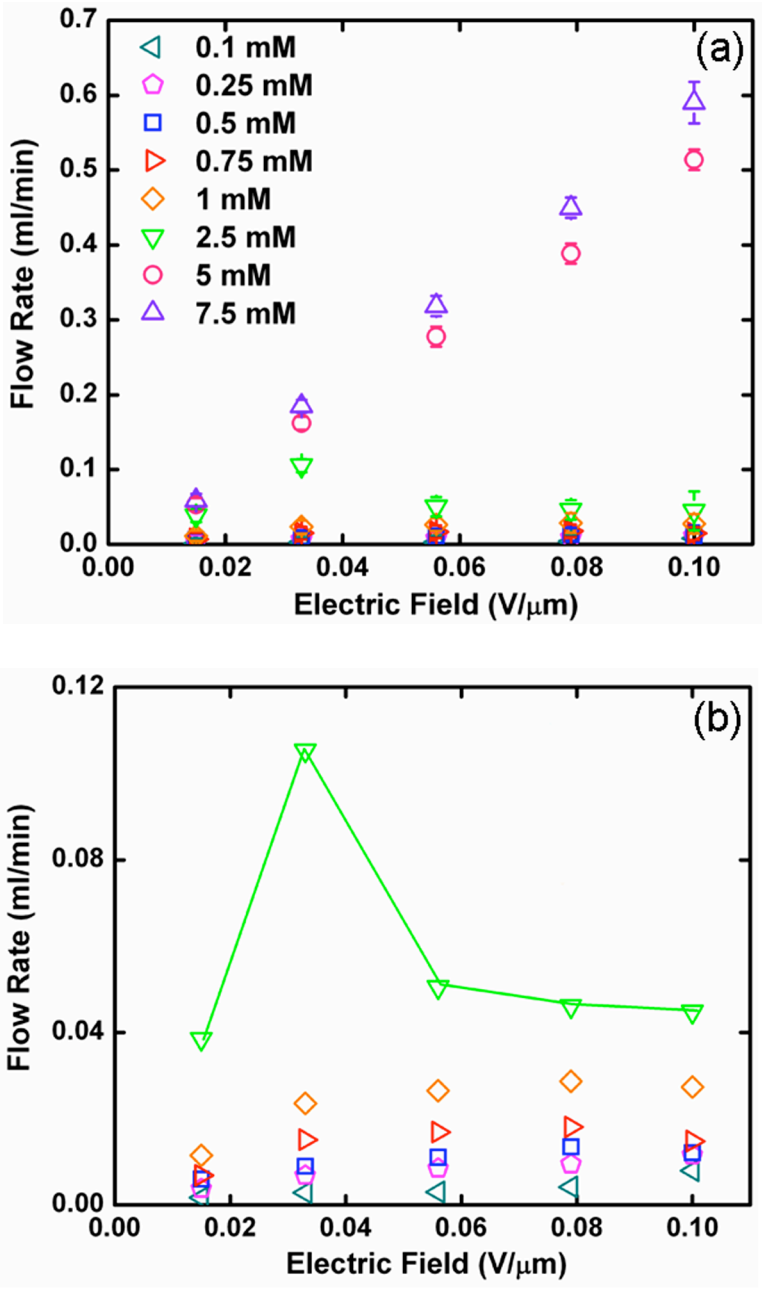

Figure 3.9 Flowrate versus electric field for an uncoated PAA membrane: (a) all buffer concentrations; (b) for lower buffer concentrations.

A possible reason for this abnormality could be the direct conduction of current through the bare PAA membrane at higher voltages arising from electrochemical

reactions occurring on the surface of the membrane. This would be reflected in the current-voltage characteristic for the uncoated membrane. A plot of the current-voltage characteristic for a bare PAA membrane with 1 mM buffer concentration in figure 3.10 shows a linear trend thus leading to the belief that there was no direct conduction of current through the PAA membrane. Additionally an experiment was performed where a bare PAA membrane with the barrier layer (~50 nm thick) at the bottom was mounted inside the PDMS container with 1 mM buffer solution on both sides and a voltage was applied. The barrier layer was able to withstand a voltage drop of around 35 V without current leakage before it broke down. This was much higher than the maximum effective applied voltage (~ 9 V) on the PAA membrane in the pumping tests, which further eliminates the possibility of current conduction through the membrane during flowrate measurements. At this moment, a confirmed explanation for this abnormal behavior is not available.

3.4.3 Additional Comments on Error Analysis

Since the pumping setup design was an open system and the flowrate was measured based on mass differences, electrolyte loss due to electrolytic reactions at electrodes could induce an error in the measurement, which could be significant for concentrations below 1 mM as flowrates at these concentrations were small. The only important electrolytic reaction was electrolysis of water (Yao et al. 2003) since inert platinum electrodes were used for the experiments. This was corrected by measuring the total mass of the filled PDMS container before and after each run, the difference of which gave the mass of water lost from electrolytic reactions. The amount of H_2 and O_2 lost at

the cathode and anode was calculated from the electrolysis reaction and added to the corresponding side prior to the calculation of flowrate for each run. The results discussed above reflect the gas loss correction. Another source of error could arise from reduction in pH of the buffer in the upstream region of the pump. The pH value of the buffer was measured for both sides after each run and was not found to fall below 8, due to the short run times employed here. The conductivity of the solution was also not found to change with time. The error from emptying the container and measuring the mass of electrolyte left behind in each chamber was also tested. Twenty trial runs were performed with a dummy electrolyte and the error from this was found to be below 10%.

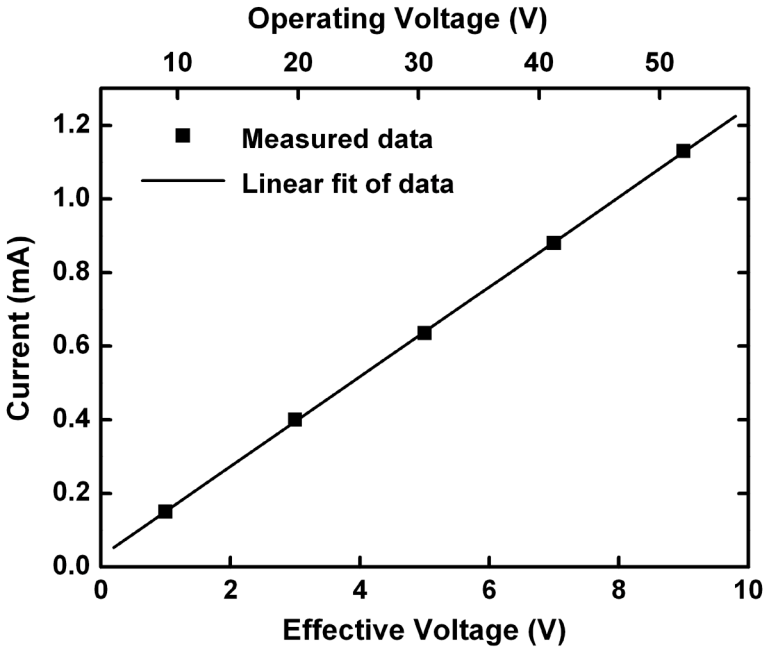

Figure 3.10 Current-voltage characteristic for a bare PAA membrane with 1 mM buffer solution.

3.5 Summary

Nano structured SiO_2-coated PAA membranes have been fabricated and tested for EO pumping. Results show that these nano structured membranes can achieve EO pumping flowrates that are higher than those reported in literature at a low effective applied voltage across the membrane. This is attributed to its dense array of highly ordered parallel nanopores resulting in a high porosity and a low tortuosity of unity. A maximum normalized flowrate of 0.125 ml/min/V/cm^2 was obtained based on the effective applied voltage with 2.5 mM buffer solution, which is much higher than most of those reported in literature. The only comparable result is obtained using porous silicon membrane at a higher applied voltage (~50 V). The low operation voltage and cost-effective fabrication could make PAA membrane more attractive.

A decrease in flowrate was observed for lower concentration buffers due to comparable electric double layer thickness with the pore diameter, resulting in a change in the velocity profile within the nanopore. Additionally, the ionic conductance of the nanopores deviates from bulk value at low buffer concentrations, as demonstrated in single nanopore measurements in literature. Tests were also conducted on uncoated PAA membranes and results showed that the pump flowrate is lower than those from SiO_2-coated membranes. Interestingly, the flowrate measured using uncoated PAA membrane does not follow a linear trend when the electrolyte concentration is lower than or equal to 2.5 mM and the effective applied electric field is over 0.03 V/μm, which cannot be explained with the current available information.

CHAPTER IV

FIELD EFFECT FLOW CONTROL ON ELECTRO-OSMOTIC PUMPING IN SiN_x-COATED POROUS SILICON MEMBRANES

This chapter demonstrates field effect flow control of EO pumping using silicon nitride (SiN_x)-coated porous silicon (PS) membranes. A heavily doped silicon core was used as a conducting electrode to apply a transverse gate potential over the insulating SiN_x pore walls. The applied gate potential modulates the zeta potential of these walls and thereby provides control over the EO flowrate while keeping the main electric field along the pores constant. These membranes have been fabricated using standard photolithographic techniques. The conformal insulating thin layer of SiN_x was deposited using the low-pressure chemical vapor deposition (LPCVD) technique. Gate voltages in the range of -45 V to +40 V were applied. A current leakage through the SiN_x for $V_g < 0$ has been observed. Furthermore, on switching the gate bias polarity from negative to positive, a current rectification effect known as electrolytic rectification has been observed, which leads to asymmetric EO flow velocity control at opposite gate biases.

4.1 Theory

Analogous to the metal-oxide-semiconductor field effect transistor (MOSFET) in solid-state where a conducting channel comprising of electrons or holes is generated and manipulated between the source and drain electrodes through the application of a bias at a third electrode called the gate, a potential applied between the outside surface of the

channel wall and the bulk of solution within the channel (V_g), relative to the local potential in the channel, V_{EOF}, will result in a change of zeta potential (ζ) through polarization of charge (capacitance effect) in the channel wall. The application of a negative relative voltage ($V_{rel} = V_g - V_{EOF} < 0$) will increase the surface charge density on the negatively-charged channel wall at the solid/liquid interface and thus increase the ζ potential prompting an acceleration of fluid near the wall. The opposite is true on application of a positive relative voltage ($V_{rel} = V_g - V_{EOF} > 0$). The surface charge density on the negatively-charged channel wall at the solid/liquid interface will decrease thus reducing ζ and prompting a deceleration of fluid near the wall. Figure 4.1 depicts this principle schematically.

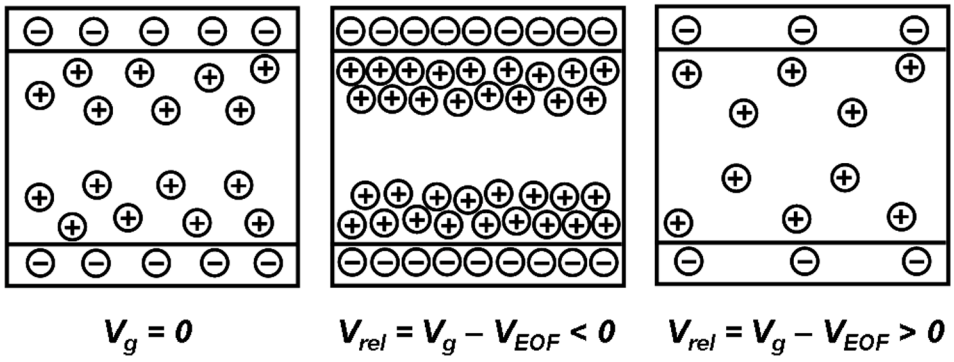

Figure 4.1 A schematic depiction of field effect control on EO flow velocity.

A three-capacitor model as shown in figure 4.2 has been proposed in literature to estimate the magnitude of the capacitance effect (C. Y. Lee et al. 2004; Schasfoort et al. 1999; van der Wouden et al. 2005). The model is a series of three capacitances, i.e. the channel wall capacitance, C_w, the stern layer and diffuse layer capacitances of the EDL,

C_{stern} and C_d respectively. C_{stern} is usually neglected in most studies because the equivalent capacitance of the EDL is dominated by C_d as the stern layer is extremely thin compared to the EDL thickness, following the equation:

$$\frac{1}{C_{EDL}} = \frac{1}{C_{stern}} + \frac{1}{C_d}. \tag{4.1}$$

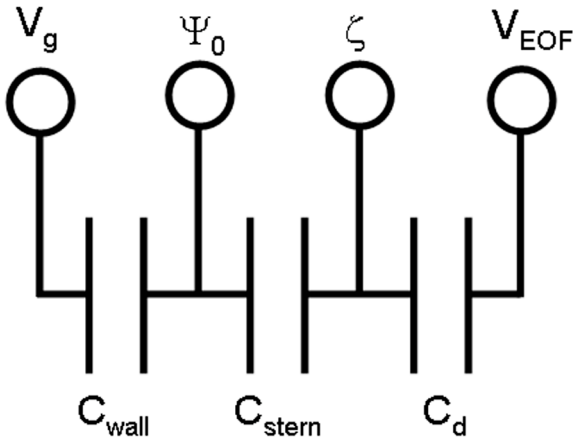

Figure 4.2 A three-capacitor model to estimate the magnitude of the capacitance effect. Ψ_0 – surface potential of SiN_x wall. Adapted from (van der Wouden et al. 2005).

The capacitance per unit surface area is given as

$$C = \frac{\varepsilon \varepsilon_0}{d}, \tag{4.2}$$

where d is the separation distance between the capacitor plates. For the EDL, d is the thickness of the stern and diffuse layers. The change in ζ due to a potential V_g applied on the outside of the channel wall is then expressed as

$$\Delta\zeta = \frac{C_{wall}}{C_d}\left(V_g - V_{EOF}\right). \tag{4.3}$$

C_d for dilute aqueous solutions is expressed as (Bard and Faulkner 1980)

$$C_d = 228 z \sqrt{c} \cosh(19.5 z \zeta). \tag{4.4}$$

Here c is the electrolyte concentration in mol/L, z is the ion valence and ζ is expressed in mV. Since C_d is a function of electrolyte concentration and $|\zeta|$, equations (4.3) and (4.4) are coupled and the modulation of ζ at high electrolyte concentration and high $|\zeta|$ becomes difficult. Furthermore equations (4.3) and (4.4) suggest that $\Delta\zeta$ will tend to saturate at higher values of $|V_g|$.

4.2 Materials

For the fabrication of PS membranes, 4″ n-type silicon wafers (Silicon Quest International, Inc., CA) were used, which were polished down to 200 μm thickness. These wafers were heavily doped having a resistivity of 0.005 ohm-cm. This was done so that gate voltages applied over the insulating pore wall would suffer minimum resistive loss within the PS core (current leakage was observed through the insulating wall – refer to section 4.4.2 for further details).

From equations (4.2) and (4.3) it is seen that $\Delta\zeta$ is proportional to C_{wall} and hence a thin channel wall having a high dielectric constant and high breakdown field is needed so that effective ζ modulation can be achieved using low gate voltages over the channel wall. To achieve this LPCVD SiN_x was chosen as the gate dielectric material since it has a high breakdown field (~10^7 V/cm) and a dielectric constant of seven, which is higher than thermal silicon dioxide (SiO_2) (Madou 2002).

For tests of field effect control of EO pumping, two different aqueous buffer solutions spanning three pH values were used – sodium acetate buffer, pH 3.6 and pH 5;

sodium borate buffer, pH 9.2. The buffer solution concentration was maintained at 5 mM. A diffusion pump oil plug from Dow Corning 704 (Dow Corning Corporation, MI) was used to monitor the EO flowrate. Platinum electrodes were used for all measurements due to their inertness.

4.3 Experimental Procedure

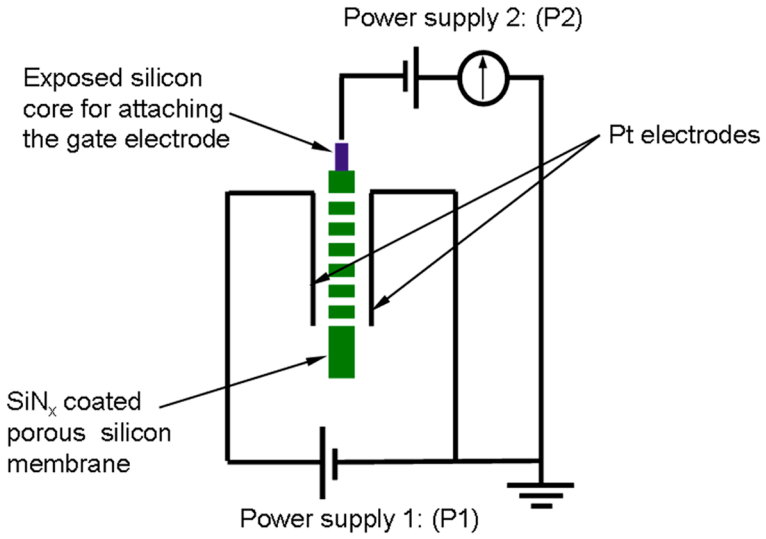

Figure 4.3 Electrical circuit schematic of the experimental setup. P1: Power supply for applying V_{EOF}, P2: Power supply for V_g.

The fabrication of SiN_x coated porous silicon membrane has been described in detail in Chapter II and will not be repeated here. The experimental set-up for EO flowrate measurement is depicted in figure 4.3. Two power supplies (Agilent Technologies, E3612A) were used in the set-up, one for applying bias to generate EO flow (P1) and the other as the source for applying bias over the gate (P2). P1 and P2 share a common grounded. A digital multimeter (Agilent Technologies, 34401A) was

connected in series to P2 to detect any leakage current through the SiN_x insulation layer (Refer to section 4.4.2 for details of current leakage). Platinum electrodes were used for both cathode and anode, which were placed in such a way that they made contact with the chip closely on both sides.

The silicon chip was mounted over a 1 mm thick glass slide inserted in the center of a fluidic chamber made of PDMS and held in place using silicone sealant. This resulted in two reservoirs in the fluidic chamber, an upstream and a downstream reservoir. The glass slide had a 2 cm × 2 cm opening in the center. The chip was mounted using colorless nail color (acetate and nitrocellulose based formulation). Once mounted, the edges of the chip were covered with a layer of silicone to make sure that the silicon exposed at the edges does not come into contact with the buffer solution. Also, the area of the chip excluding the patterned array was covered with a thin layer of silicone on both sides of the chip. This ensured that only the surface of the patterned array on either side of the chip and the pore walls made contact with the buffer solution. This was done to keep the leakage current through the SiN_x to a minimum. Prior to beginning the experiment, a small amount of DI water was placed on one side of the patterned array while holding the PDMS fluidic chamber in a vertical position (pores aligned vertically). The water was allowed to flow through the pores under capillary action and gravity. This was done to clean the pores of any contaminants and also to wet the pores. After repeating this process a few times, a small amount of the buffer solution was placed on the top of the patterned array and allowed to flow through the pores as before. This was also repeated a few times. This ensured that all the pores were filled with the buffer solution.

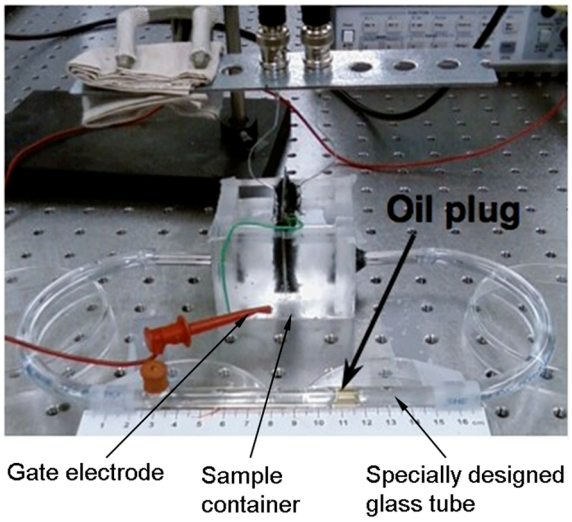

Figure 4.4 The experimental setup used for EO flowrate measurement. The PDMS fluidic chamber is seen here with the silicon chip mounted and buffer solution on either side of the chip. The fluidic chamber is attached to the specially designed glass tube through flexible nalgene tubes.

To measure the EO flowrate, a visual observation technique was followed. The PDMS fluidic chamber was designed to have two 6 mm diameter glass tubes glued to the bottom of the upstream and downstream reservoirs. The tubes were connected externally to another specially designed glass tube (GT) through flexible nalgene tubes. This resulted in a closed-loop, U-tube type system with the reservoirs open to atmospheric pressure to eliminate backpressure effects. Electrodes were placed on both sides of the chip. The downstream reservoir was first filled with buffer solution, which instantly flowed through the externally connected glass tubes under atmospheric pressure and filled the entire system including the upstream reservoir. GT had a small opening to one side with a rubber septum from where an oil plug was inserted. Under EO flow, the oil

plug in GT would move opposite to the direction of flow in the pores. The motion of the oil plug/buffer solution meniscus was monitored over a scale and the distance was recorded over time to solve for the EO flow velocity. To minimize the flow resistance of the oil plug, the inner surface of GT was coated with a thin layer (tens of angstroms) of AMC18 (Advanced Materials Components Express, LLC, PA), which made the surface lipophobic. Figure 4.4 shows the PDMS fluidic chamber used for EO flow velocity measurement with the silicon chip mounted and GT attached.

4.4 Results and Discussion

4.4.1 Field Effect Control of EO Flow

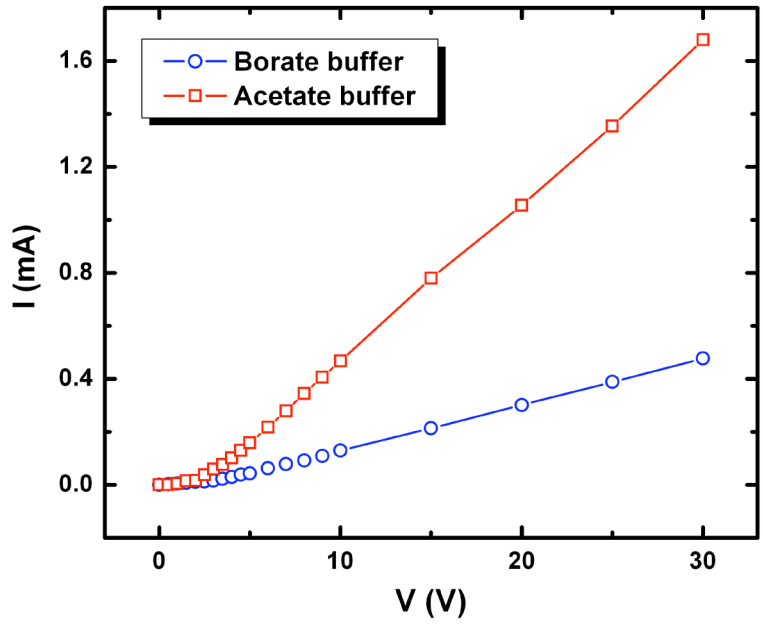

Figure 4.5 Current vs. voltage scans for the platinum electrode/acetate buffer solution system and platinum electrode/borate buffer solution system.

For all field effect control tests, the applied voltage for generating EO flow (V_{EOF}) was maintained at 25 V. However, after taking into account the decomposition potential associated with the electrode reactions at the electrode/electrolyte interface, the effective voltage was found to be less than the applied voltage. For a given electrode/electrolyte system the decomposition potential can be estimated from the initial non-linear part of a current vs. voltage (*I-V*) curve obtained by running a voltage scan between the two electrodes in an electrolyte and recording the corresponding current. Figure 4.5 shows the *I-V* scans for the platinum electrode/acetate buffer solution system and platinum electrode/borate buffer solution system. The decomposition voltages estimated from these scans are approximately 3 V and 4 V for the acetate and borate buffer solutions, respectively. The range of gate voltages applied to the pumping membrane was from -45 V to +40 V.

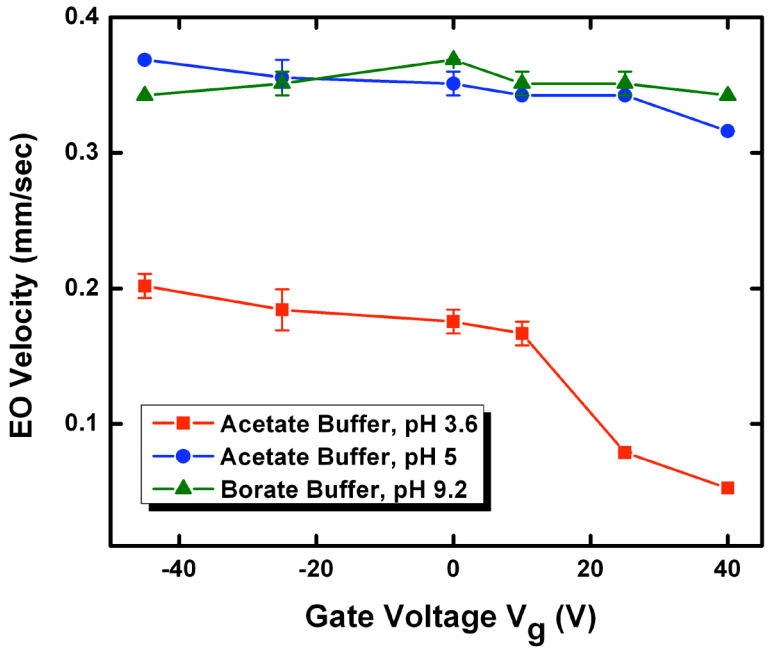

Figure 4.6. Field effect control on EO flow velocity for V_g ranging from -45 V to +40 V.

The field effect control data obtained for buffer solutions of three different pH values (pH 3.6, pH 5 and pH 9.2) are shown in figure 4.6. It can be deduced from the figure that the pH 5 and pH 9.2 buffer solutions show a lower field effect control on the EO flow velocity as compared to the pH 3.6 buffer solution. This pH dependence is in good agreement with that reported in literature for studies on fused silica capillary systems and silicon based systems (Buch et al. 2001; Ghowsi and Gale 1991; Hayes and Ewing 1992; Hayes et al. 1993a; Huang et al. 1993; C. S. Lee et al. 1991; Poppe et al. 1996; Schasfoort et al. 1999). This trend is expected since at higher pH values the zeta potential is higher which translates into a larger C_d in equation (4.4) leading to a reduced zeta potential modulation at these pH values. Furthermore, the EO flow velocities measured for the pH 5 and pH 9.2 buffer solutions are very close to each other and much higher than the EO flow velocity measured for the pH 3.6 buffer solution. This is also reasonable since the dependence of SiN_x zeta potential on buffer solution pH shows a maximum slope in the pH range of 2 and 5 with the zeta potential increasing from pH 2 to 5 and saturating for pH values greater than 5. Zeta potential measurements performed on silicon nitride in literature corroborate this trend (Bousse and Mostarshed 1991; Bu and Moudgil 2007; Hegde and Babu 2004).

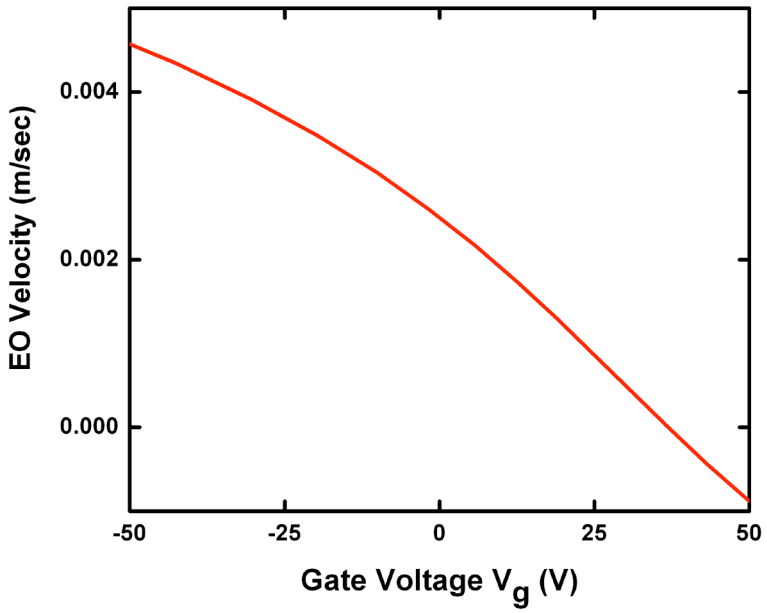

Figure 4.7 Theoretical trend of EO flow velocity against gate bias for a low pH buffer. An opposite, but equal in magnitude influence on EO flow velocity should be expected on reversing the gate bias polarity.

While the low field effect control for the pH 5 and pH 9.2 buffer solutions is anticipated, the pH 3.6 buffer solution reveals an unexpected result. Figure 4.7 shows the expected trend of EO flow velocity against gate potential calculated for a low pH solution (pH ~ 4) using equations (4.3) and (4.4) and an iterative procedure. The theoretical trend indicates an opposite, but approximately equal in magnitude influence on the EO flow velocity on reversing the gate bias polarity. The experimental trend suggests otherwise. For the pH 3.6 buffer, a velocity enhancement of approximately 15% from $V_g = 0$ was measured on application of -45 V gate potential whereas approximately 70% reduction in velocity was observed on application of +40 V gate bias. This difference arises due to an effect termed as "Electrolytic Rectification" and is explained in the following section.

The same effect is also responsible for the fact that under negative gate potential, the pH 9.2 buffer solution shows a reduced flowrate, which is exactly opposite to the expectation that negative gate potential will enhance the zeta potential, and hence the flowrate.

4.4.2 Current Leakage through Silicon Nitride – An Electrolytic Rectification Effect

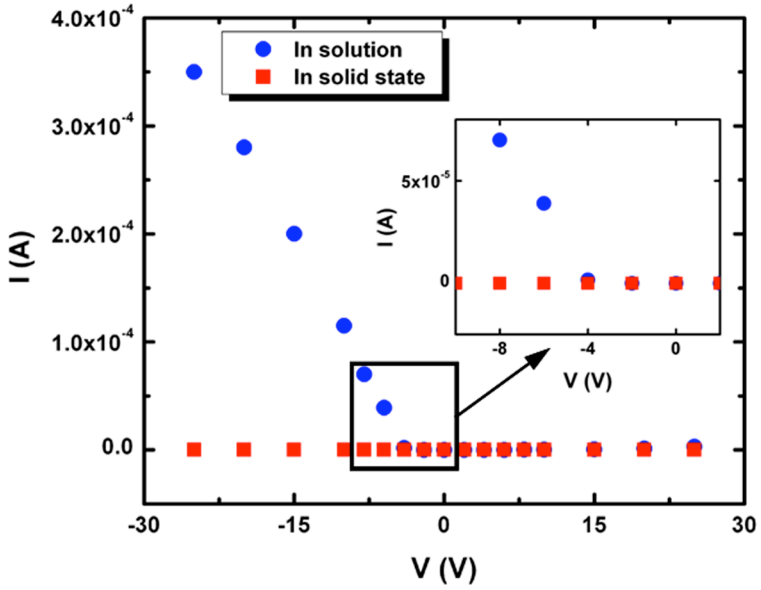

Figure 4.8 I-V plot for a voltage scan in solution from -25 V to +25 V demonstrating the electrolytic rectification effect on 500 nm SiN_x coated porous silicon membrane. Current leakage begins at around -4 V. Also depicted is the I-V plot measured in solid-state conditions showing no rectification effect. The two plots overlap each other starting from -4 V through to +25 V as seen in the inset plot.

As is well known, SiN_x, like thermal SiO_2, is a commonly used insulating film functioning as a gate dielectric material in microelectronic devices like MOSFETs (Brown and Khaliq ; Buchanan 1999; Depas et al. 1996; Ma 1998; Wong and Gritsenko

2002; Wright and Saraswat 1989; Yeo et al. 2000), owing to its superior electrical properties - dielectric constant of LPCVD SiN_x is seven and its dielectric strength is as large as 10^7 V/cm (Madou 2002). However this is true only for solid-state devices. In an aqueous solution the electrical properties (dielectric strength and resistivity) of this film are substantially modified.

To better understand this phenomenon, resistivity of the LPCVD SiN_x films deposited on porous silicon membranes used in these experiments was measured. By placing the PDMS sample container in a vertical position, a drop of buffer solution was placed on the top side of the patterned area of the mounted porous silicon chip and was allowed to wet the opposite side through capillary action. The silicon was biased cathodically (negative bias applied onto silicon) while a platinum electrode placed in the buffer solution drop was biased anodically and an I-V plot was generated for a voltage scan of 0 to -25 V. The measured resistivity was on the order of 10^7 ohm-m, about seven orders of magnitude lower than that reported for measurements done under solid state (Madou 2002). This lower resistivity allows a significant leakage current through the SiN_x film. Moreover when the bias polarity was reversed, i.e., silicon biased anodically and the buffer solution biased cathodically, a negligible leakage current was measured. Figure 4.8 shows the I-V plot for a voltage scan from -25 V to +25 V, together with a similar scan for the SiN_x in all solid-state, which did not show any leakage current over the whole voltage range. The observed trend is similar to that of an I-V plot of a rectifying diode where current is allowed to pass through in a forward biased condition (silicon biased cathodically in this case) and blocked in the reverse biased condition (silicon biased anodically here). An analogy with a metal-oxide-semiconductor (MOS)

system can be drawn here, where the role of the metal is played by the buffer solution and therefore such systems are referred to as the electrolyte-insulator-semiconductor (EIS) systems and the rectification effect is termed as electrolytic rectification.

The electrolytic rectification effect on an EIS system involving a buffer solution, a thermally grown SiO_2 and silicon was first reported by M. Madou and co-workers (Madou et al. 1979, 1980) and a few observations made by them on their samples are noteworthy and listed as follows.

1. Microscopically visible flawed regions on the SiO_2 after the application of a cathodic bias;
2. Generation of bubbles, presumably hydrogen, at localized points on the surface under high cathodic bias;
3. Luminescence, characteristic of the cation in the buffer solution under high cathodic bias on *p*-type silicon;
4. For *p*-type silicon, an increase in cathodic current upon illumination with a microscope lamp;
5. Flaws, if present, tend to spread over the SiO_2 surface at cathodic voltages of greater than 10 V.

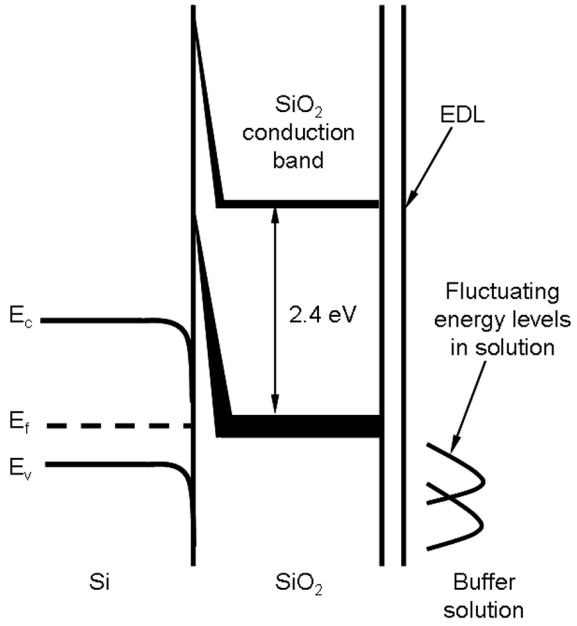

Figure 4.9 Band diagram of a Si/SiO_2/buffer solution system as postulated by Madou and co-workers. The impurity band lays 2.4 eV below the SiO_2 conduction band. The fluctuating energy levels are indicated in the solution region. (Madou et al. 1980)

From their experiments they concluded that the current through SiO_2 was electronic and postulated a model to explain the cause of the current. It is known that there is a so-called impurity band within bulk SiO_2, which lies 2.4 eV below the SiO_2 conduction band (Morrison 1980). Figure 4.9 shows the band diagram for the Si/SiO_2/buffer solution system with the impurity band located 2.4 eV below the SiO_2 conduction band. It is also known that this band has an exceptionally large capture cross-section for electrons and is associated with alkali ions (Na^+, K^+) that are almost always present within the bulk SiO_2 (DiMaria 1978; Madou 2002). Moreover, SiO_2 is known to be structurally very "open", meaning there exist channels within its structure through which positive ions such as Na^+ and K^+ can readily migrate and therefore when in contact with an aqueous solution it

behaves like a sponge to ions in the solution. Madou and co-workers suggest that under cathodic bias on silicon large amounts of protons (H^+) or positive ions like Na^+ if present in the solution diffuse to the Si/SiO_2 interface further augmenting the ionic density already present within the oxide. If flaws are present on the oxide surface then this diffusion occurs most rapidly at these defects. Additionally the cathodic bias bends the bands in the SiO_2 making it easier for electrons to tunnel to the conduction band or the impurity band of the oxide, depending on the bias. They further go on to suggest that the band in the SiO_2 that actually does the conducting is not necessarily the conduction band but rather the impurity band associated with the moving positive ions. They observed that a cathodic bias of about 2 V was sufficient to lower the impurity band so that electron transfer to this band could readily occur. As the electrons tunnel through, they neutralize the positive ions causing more positive ions to diffuse in, until the SiO_2 is heavily doped with H^+ or Na^+. This model is consistent with the observation of copious amounts of hydrogen bubbling out at localized spots at the SiO_2/buffer solution interface, which is an indication of the development of electronically conducting channels within the SiO_2 at these localized spots. On reversing the bias polarity, i.e., under anodic bias, the protons or ions will tend to move away from the Si/SiO_2 interface, thereby increasing the barrier for electron flow and hence blocking their transport.

Electrolytic rectification effect in LPCVD SiN_x thin films has not been reported in literature yet and here we attempt to shed light on this phenomena based on the model postulated by Madou and co-workers. LPCVD SiN_x is known to be an excellent barrier material for diffusion of impurity ions such as Na^+ and K^+ (Madou 2002), which is why it is used as a diffusion mask over thermal SiO_2 – a poor diffusion barrier material.

However certain amount of hydrogen entrapment in SiN_x films has been reported which is dependent upon the reagents used during their deposition (Belyi et al. 1976; K. Chen et al. 1993; Vlasov et al. 2003). In LPCVD SiN_x, ammonia and silane contribute to hydrogen incorporation in the nitride film (Vlasov et al. 2003). This entrapment effect may be significant due to the fact that the deposited nitride films had a non-stoichiometric nature, leading to crystallographic point defects such as vacancies within the film, which can be filled in with atoms of different elements. The trapped hydrogen is believed to considerably influence the chemical, physical and electrical properties of these films (Belyi et al. 1976). It has also been reported that SiN_x film surface undergoes a slow conversion to a hydrated silicon nitride layer when in contact with an aqueous solution and the hydrated layer can significantly increase hydrogen ion concentration in the bulk film (Yu and Yen 2002). In view of these reports, it is therefore possible that an impurity band associated with hydrogen ions, similar to the one present in thermal SiO_2, may be present below the SiN_x conduction band. The exact energy level associated with this impurity band remains unknown at this point of time. A cathodic bias on silicon will have two effects on this band: (1) it will cause H^+ ions to diffuse in the SiN_x, further enhancing their concentration; and (2) it will bend this impurity band so that electron transfer from silicon to this band readily occurs. The tunneling electrons will neutralize the hydrogen ions leading to hydrogen evolution from the SiN_x/buffer solution interface. To further substantiate the occurrence of electrolytic rectification in SiN_x, a test similar to the one carried out by Madou and co-workers (Madou et al. 1980) was conducted. A flaw was intentionally introduced on the SiN_x surface by lightly scratching it with a diamond scribe and a cathodic bias of ~50 V was applied for around ten minutes. As observed by Madou,

the flaw began to spread over the SiN_x surface. Figure 4.10 shows the SEM micrographs of the flaw on the SiN_x surface before and after the application of cathodic bias.

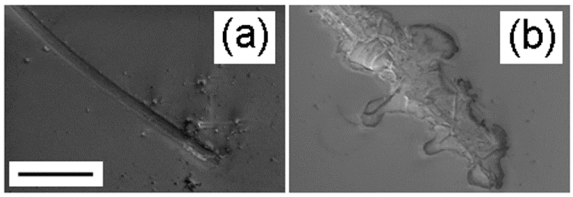

Figure 4.10 Intentionally introduced flaw on the SiN_x surface, (a) before and (b) after application of cathodic bias. The bias spreads the flaw over the nitride surface. The scale bar is 30 μm.

Additionally the effect of buffer solution concentration as well as time on current leakage through the SiN_x film was also tested to further understand the diffusion of hydrogen ions within the SiN_x film. On a nitride coated silicon chip, a 2 mm × 1 mm area was defined by using a non-conducting polymer. Sodium acetate buffer solutions of different concentrations (100 mM, 10 mM, 1 mM and 0.1 mM) were used. A drop of each concentration was placed over the exposed area and a Pt electrode was immersed in the drop. A cathodic bias of 10 V was applied for all the cases. As noted earlier a leakage current was measured and hydrogen bubbles were seen evolving from the exposed area. The hydrogen bubble evolution was very severe for the 100 mM solution leading to a very unstable and immeasurable current. For the rest of the concentrations, the current was fairly stable and decreasing overall with the concentration. This is depicted in figure 4.11 (a). The data point for 100 mM solution was excluded because of the extremely large uncertainty due to unstable current.

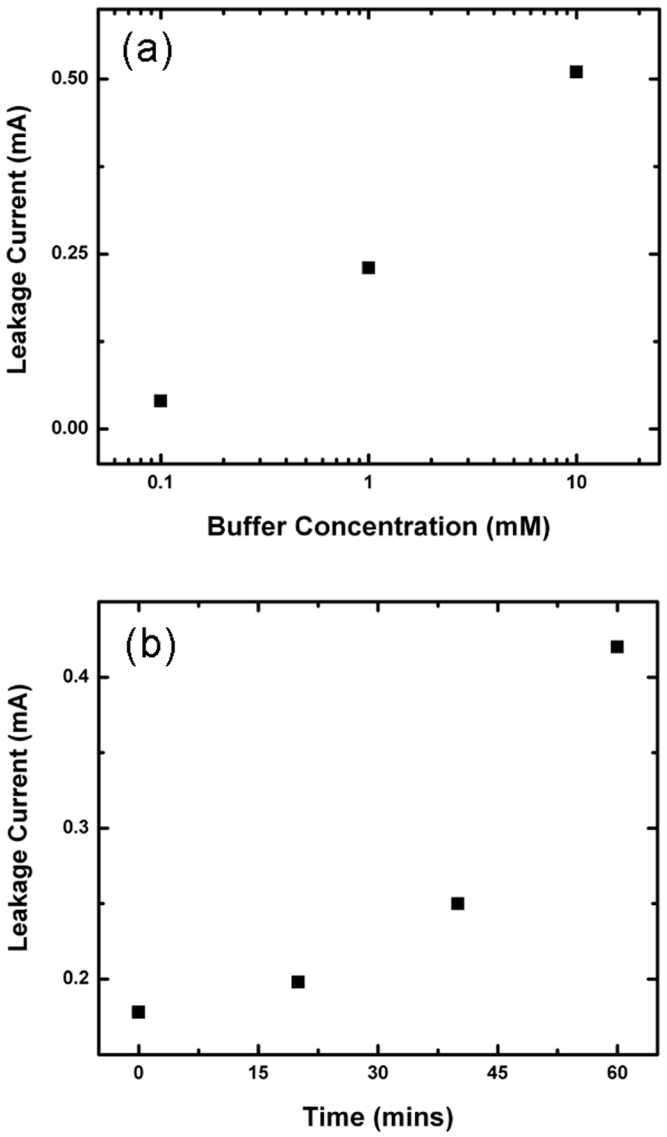

Figure 4.11 (a) Leakage current through SiN_x film as a function of buffer concentration. (b) Effect of time over leakage current through SiN_x film. The overall current went up consistent with the aforementioned fact that defects in the nitride film tend to spread further over time under cathodic bias.

Measurement results show that the leakage current increases by approximately one order of magnitude as the concentration of the buffer solutions increases by two

orders of magnitude. Currently we do not have a confirmed explanation on this observed relation of the leakage current as a function of buffer concentration. One possibility is that the resistance of the buffer solution is on the same order of the SiN_x films because even though the leakage conductivity of SiN_x is small (on the order of 10^{-8} S/m as estimated from figure 4.8), its thickness is only 500 nm, which is much smaller than the size of the droplet. Therefore, the electrical resistance of the buffer solution can be comparable to that of the SiN_x film. One also cannot rule out the possibility that different concentration buffers might affect the electrical leakage of the SiN_x film, and hence alter its resistivity through energy level changes at the nitride/buffer solution interface that are expected to occur with a change in the ionic concentration of the buffer solution (Morrison 1980).

A time dependent test on the leakage current was also performed using the same setup and 1 mM buffer solution (pH ~ 4.5). The cathodic bias was maintained at 10 V and leakage current was measured at every 20-minute interval for one hour. The current measured showed minor fluctuations, again due to hydrogen bubble formation. As time progressed the overall leakage current went up. This is expected and is consistent with the aforementioned fact that defects in the nitride film tend to spread further over time under cathodic bias. Figure 4.11 (b) illustrates this effect. The exponential trend indicates that the spread of defects in the nitride film multiplies exponentially over time. This test indicates that over time more electrically conducting channels are developed within the nitride film under cathodic bias thus causing additional hydrogen diffusion to occur and thereby deteriorating the nitride film further. It is worth noting that a portion of the increase might come from the increased buffer concentration due to evaporation and

dissociation occurring at the electrodes. Over the one-hour period, the droplet shrinks by about 25% from evaporation and dissociation. To minimize the effect of evaporation we repeated the same experiment in a humid environment by enclosing the setup within a box. Inside the box, along with the setup, was placed a petri dish filled with water. The water evaporation from the petri dish ensured a humid environment within the box. The result showed a monotonic increase of leakage current with time, similar to that shown in figure 4.11 (b). It should also be noted here that each experiment was performed on a different chip, and other than the results shown in figure 4.11 (b), the effects of gate potential were all measured within a time period of less than five minutes. Therefore, the drift of leakage current over time should not contribute significantly to any background drifting for the reported experimental results.

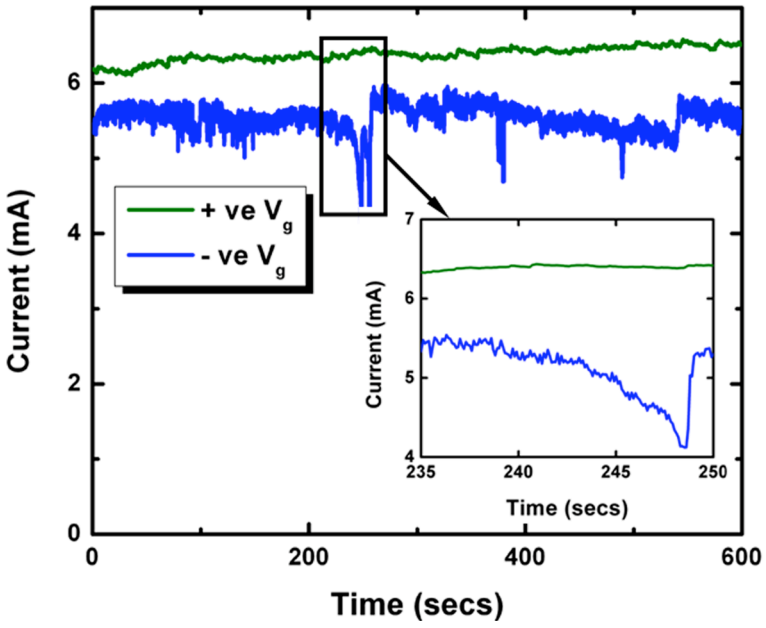

Figure 4.12 Fluctuating current under negative gate bias suggesting disruption or blockage of ionic current within the channels. Inset: Enlarged view of a section of the plot to highlight the current dip.

Another concern that can be raised here is dopant diffusion from the heavily doped silicon to SiN_x at high temperatures encountered during or after nitride deposition. Such diffusion would aid current leakage through the nitride film. However, reports in literature indicate that this is unlikely, as SiN_x films in addition to being used as diffusion barriers to alkali ions also serve as a barrier to the diffusion of *p*- and *n*- type dopants during high temperature processes (Doshi et al. 2001; Izumi et al. 2001). This is especially true given the fact that the only high temperature step used was during the SiN_x deposition at 840 °C without any further annealing treatment.

Referring back to figure 4.6, the observed difference in the change in EO flow velocity on altering the gate bias polarity can now be construed in view of the above-mentioned reasoning. Since hydrogen bubbles out at localized points from the SiN_x/buffer solution interface under cathodic bias, with the evolution being greater for a higher cathodic bias, it is highly likely that hydrogen bubbles block some of the channels in the PS membranes. Such a blockage would then reduce the field effect control of EO flow velocity for $V_g < 0$. However, for $V_g > 0$, the leakage current measured is negligible and no hydrogen evolution occurs for these gate voltages. Therefore a pronounced field effect on EO flow velocity is observed for $V_g > 0$. To corroborate this claim, a test was conducted wherein the ionic current across the platinum electrodes was measured under positive and negative gate bias by placing an ammeter in series with P1 in figure 4.3. Under positive gate bias the measured current is much more stable than that for negative gate bias. The current under negative gate bias shows significant fluctuations with several large downward spikes. This current behavior under negative gate bias suggests the disruption or blockage of ionic current within the channels of the porous silicon

membrane by the generated hydrogen bubbles. Figure 4.12 shows the current-time plot obtained under positive and negative gate bias.

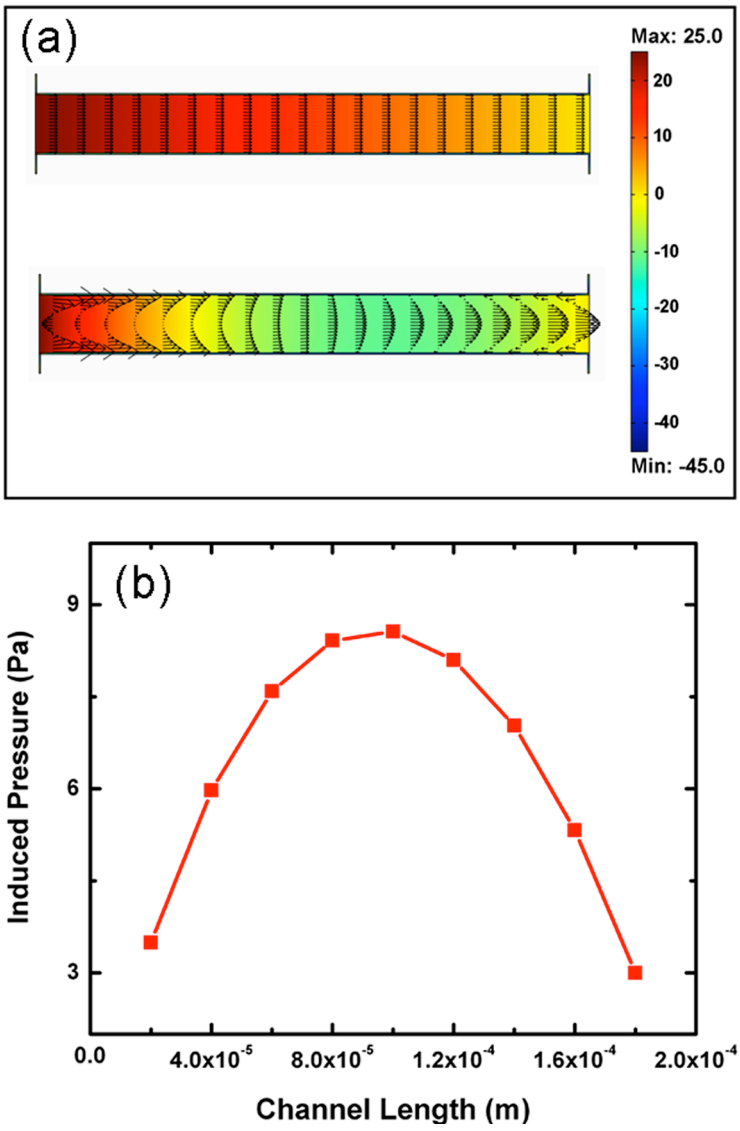

Figure 4.13 (a) Simulated effect of gate potential on the local channel potential and the EO flow velocity for two cases of SiN_x conductivity: (top) 2.88×10^{-8} S/m, as measured in our experiment; (bottom) 2.88×10^{-5} S/m, for comparison. Surface: Electric Potential (V), Arrow: EO Flow Velocity (m/s). (b) Induced pressure variation within the channel along its axis.

One might wonder what the influence of gate potential on the local channel potential is because of the current leakage for $V_g < 0$ and how such an influence would affect the flow velocity within the channel. To provide some insights on this, the EO flow velocity and the local potential inside the channel was simulated using a commercial finite element package, COMSOL 3.2 (COMSOL, Inc. MA) in line with our previous work (Sun et al. 2008). The channel dimensions used were the same as those of a single channel in the porous silicon membrane. The leakage conductivity for the 500 nm SiN_x wall was estimated to be 2.88×10^{-8} S/m (from figure 4.8) and a conductivity value of 0.047 S/m was measured for the buffer solution using a conductivity meter (Oakton CON 11 series). These values were used respectively for the nitride channel wall and buffer solution within the channel.

The electric potential and the EO flow velocity within the channel were calculated using Laplace and Navier-Stokes equations respectively. We simulated the case for V_g = -45 V (the maximum negative gate bias applied in our experiment). The result as depicted in figure 4.13 (a-top) indicates that the gate potential does not influence the local channel potential or the EO flow velocity within the channel. To further illustrate this point one more case was simulated wherein the nitride wall conductivity was increased by three orders of magnitude. This result is depicted in figure 4.13 (a-bottom) and indicates how the leakage current, and therefore the gate potential, would have affected the local channel potential and hence the local electric field had the nitride wall conductivity been significantly higher than that measured in our experiments. In this case since the application of the gate potential changed the local electric field inside the channel, the EO flow velocity would not be uniform along the channel axial direction as is seen in figure

4.13 (a-bottom). This would cause a pressure build-up at the center of the channel, giving rise to a pressure driven flow along the channel axis, which opposes the EO flow at the inlet and enhances it at the outlet to maintain a mass balance. Figure 4.13 (b) shows the induced pressure variation along the channel axis. However, the leakage current would affect only the local flow field in figure 4.13 (a-bottom) but the overall flowrate should still be the same for both cases. This is because no matter how the local electric field varies, the overall external driving force to the channel in the flow direction is that applied at the two ends, which is the same with or without the applied gate voltage. This was confirmed through integration of the total flow velocity over the channel cross-section. In view of the result of figure 4.13 (a-top), which indicates that the leakage current and hence the gate bias does not influence the local flow field, hydrogen bubble generation seems to be the more likely cause for a reduced flow velocity at $V_g < 0$ than the influence of gate potential on the local channel potential.

On a surprising note, a fact worthy of mention here is that all the works done on single channel FEFC reported so far make no mention of electrolytic rectification effect in their results. The FEFC study carried out by Schasfoort and co-workers (Schasfoort et al. 1999) utilizes a single microchannel surrounded by a 390 nm thick SiN_x wall (the nitride thickness used in this work is 500 nm), yet their work does not indicate any signs of current rectification through the nitride wall. Other reports on single channel FEFC (Buch et al. 2001; Hayes and Ewing 1992; Hayes et al. 1993a, 1993b; Karnik et al. 2005; Polson and Hayes 2000; van der Wouden et al. 2005) employ SiO_2 as their channel wall material which, as this study indicates, is worse than SiN_x due to its open structure and lower resistance to ionic diffusion in the presence of an aqueous solution. A possible

reason for these authors to ignore the electrolytic rectification effect in their study could be the contact area of the channel wall with the metal electrode used for applying the gate bias. In most of these reports the metal electrode makes contact with only a small portion of the channel surface area, and therefore the leakage current measured through the dielectric would be negligible. This is not the case for porous silicon membranes used in this work. The SiN_x layer covers the entire surface area of the porous silicon membrane. In other words, the heavily doped silicon core used for applying the gate bias makes contact with the entire surface area of the SiN_x channel array. This translates into a higher leakage current under cathodic bias and the multitude of channels further magnifies this effect.

4.5 Summary

A field effect modulation of EO flow in an array of microchannels was demonstrated for the first time. The channel array is composed of heavily doped silicon core with 500 nm thick SiN_x film conformally deposited over the surface of the entire porous silicon membrane. The silicon core functions as the gate metal to control the EO flow inside the microchannel array. Measurement results indicate an EO flow velocity enhancement of approximately 15% on application of -45 V gate bias and a reduction of nearly 70% on application of +40 V gate bias for a pH 3.6 buffer solution. This discrepancy in enhancement-reduction of EO flow velocity has been attributed to the electrolytic rectification effect, which is a first-time report for SiN_x. The electrolytic rectification effect causes a leakage current to flow through the nitride when silicon is biased negatively with respect to the buffer solution, which results in hydrogen being

evolved at the SiN_x/buffer solution interface. The hydrogen then inhibits EO flow through the porous membrane by blocking the channels. Results from this study indicate that field effect control can be realized on a channel array for EO pumping control; however, to increase the flowrate by applying negative gate potential, methods to prevent current leakage through the dielectric material must be found.

This research brings to light the occurrence of electrolytic rectification in SiN_x – an effect that has been studied and documented only for SiO_2 so far. Though the reasoning behind the rectification effect in SiN_x is not firmly confirmed, this work opens up an avenue for researching this dielectric material further from the standpoint of hydrogen diffusion and electron transport through it – especially when SiN_x is in contact with an aqueous solution and under bias. This work further indicates that electrolytic rectification effect can play a significant role in microfluidic devices and should not be neglected in certain circumstances for future microfluidic applications.

CHAPTER V

IONIC CONDUCTANCE OF NANOPOROUS GLASS MEMBRANES

A recent molecular dynamic (MD) simulation result has brought out an interesting and unexpected ionic current behavior with electrolyte concentration – for a 3 nm pore with high zeta potential, the ionic current increases linearly with concentration up to 0.9 M and begins to deviate from linear behavior beyond that. This chapter of the dissertation will present measurements of the conductance of nanoporous glass membranes at high electrolyte concentrations and attempt to shed light on this interesting phenomenon from an experimental perspective. Unlike the in-house fabricated porous membranes discussed in the past two chapters, these membranes having an average pore diameter of 4 nm were purchased commercially. The conductance was measured with two kinds of electrolytes – sodium chloride (NaCl) and potassium chloride (KCl). The experimental results indicate an expected linear trend of ionic conductance with electrolyte concentrations up to 2 M, contrary to that observed in the MD simulation study.

5.1 Materials

The porous glass membranes were purchased from a commercial vendor (VYCOR Brand Porous Glass 7930, Corning, Inc.). The average pore diameter as specified by the vendor was 4 nm and the membrane thickness was 500 μm. Figure 5.1 depicts the microstructure of the porous glass membrane taken in a transmission electron microscope (TEM) (Levitz et al. 1991). Two nanopores have been encircled and labeled

in the figure. Two electrolyte compositions were used for the experiments – NaCl and KCl, with concentrations ranging from 5 mM to 2 M.

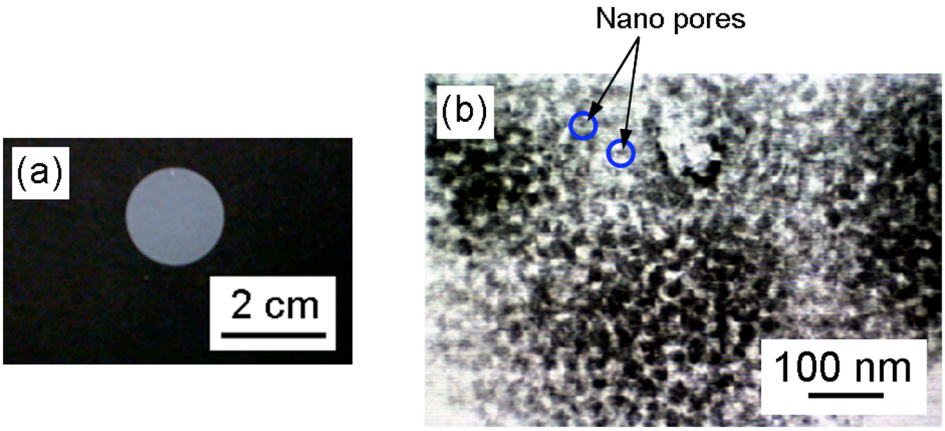

Figure 5.1 (a) Optical image of the nanoporous glass membrane. (b) TEM image of the same membrane. (Levitz et al. 1991)

5.2 Experimental Details – Setup and Procedure

The experimental setup and procedure used for these experiments were similar to the one used earlier for EO pumping with PAA membranes and therefore it will be described only briefly here. The setup consisted of a PDMS fluidic chamber split into two halves by a glass slide, which had a 3.17 mm diameter hole punched into it. The porous glass membrane was mounted onto the glass slide using transparent nail color as glue. Two platinum electrodes were fixed permanently to the chamber, each separated from the glass slide by 1.5 cm on either side. As before, the membrane resistance was isolated by measuring two resistances (resistances were measured from the slopes of I-V curves) – one without the membrane and the other with the membrane mounted in the middle of the

chamber. Subtracting the former from the latter gave the value of the membrane resistance and hence the conductance.

Since these experiments were performed with very high concentration electrolytes (up to 2 M), a power source with the ability to sustain a high current was needed, especially while carrying out resistance measurements without the membrane mounted. For this purpose, three AD621 differential amplifiers (Analog Devices, Inc.) were used in parallel which function as a voltage source and also set the overall system current limit to 45 mA. The differential amplifiers were controlled by a data acquisition card in a computer and operated through a LabWindows program (National Instruments Corporation). A variable resistor ranging from 10 Ω to 10 kΩ was connected in series with the platinum electrodes and another AD621 differential amplifier was used to measure the voltage drop across this variable resistor and thereby calculate the system current. The resistance between the two platinum electrodes can then be calculated using the system current, the voltage drop across the variable resistor and the total applied voltage.

Prior to beginning the measurement for each concentration, the porous glass membrane was primed by placing a small amount of electrolyte of the particular concentration to be used for testing, on one side of the membrane and agitating it over the membrane surface. This was followed by electro-osmotic priming where the PDMS container was filled with electrolyte solution on both sides of the membrane and a small voltage was applied across the electrodes for approximately 30 min. The combination of capillary filling, agitation, and priming ensures that all the channels in the porous glass membrane are free of ionic contaminants and are filled with the testing solution. Three

measurements were recorded for each concentration and the membrane conductance was taken as the average value of the three readings. Figure 5.2 gives the details of the experimental setup used for measurement of ionic conductance.

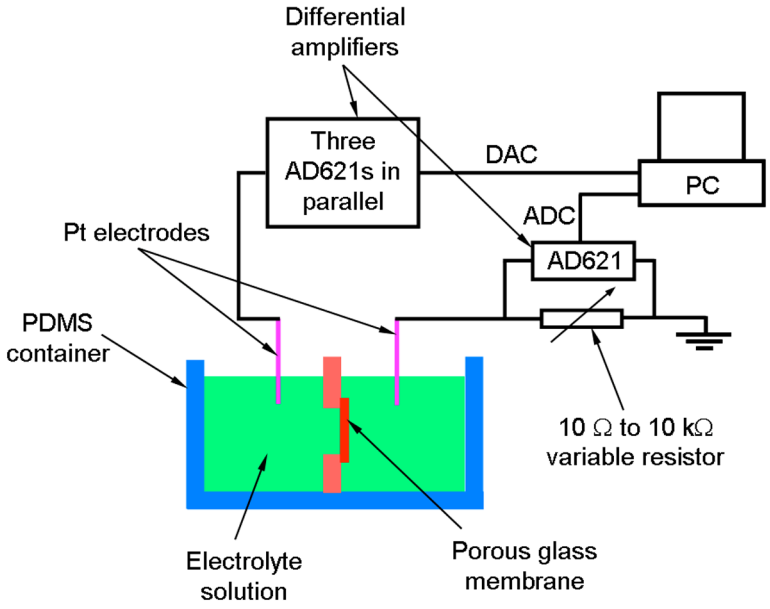

Figure 5.2 Experimental setup for measurements of conductance of a nanoporous glass membrane.

5.3 Results and Discussion

The ionic conductance versus concentration plots for NaCl and KCl electrolytes are depicted in figure 5.3 (a) and (b), respectively. As expected, the ionic conductance begins to deviate from bulk behavior at low electrolyte concentrations – in this case at a concentration of about 10 mM. This effect has been documented and attributed to surface charge dominated ionic transport with overlapped EDL in nanochannels (Karnik *et al*. 2005; Stein *et al*. 2004).

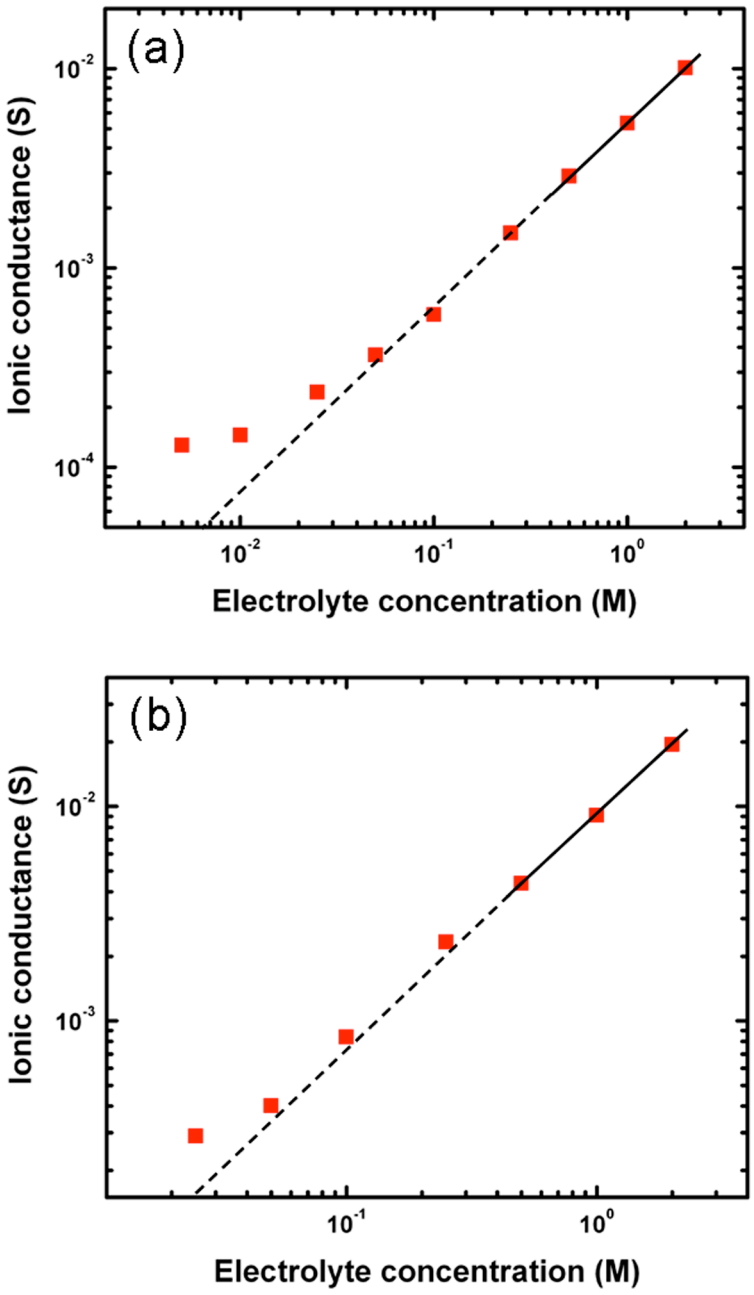

Figure 5.3 Experimental data for ionic conductance versus electrolyte concentration for two different electrolyte compositions: (a) NaCl and (b) KCl. The black solid/dotted line corresponds to bulk behavior. Ionic conductance above 500 mM follows a linear trend whereas at lower concentrations the expected deviation from linearity is observed.

At higher electrolyte concentrations (beyond 1 M), an MD simulation study indicated an unexpected concentration dependence of ionic conductance of a 3 nm diameter pore (Ge *et al*. 2009). The result, shown in figure 5.4, indicates that the ionic current increases linearly with electrolyte concentration up to about 1 M and then deviates from linear behavior as the electrolyte concentration further increases. This non-linear behavior as explained by Ge *et al*. is associated with more counter ions in the near wall region at high electrolyte concentrations and high surface charge densities. For a 3 nm diameter pore, this means the total number of ions in the EDL is comparable to that outside the EDL. The highly packed counter ions in the near wall region experience larger viscous forces, leading to a low mobility, which could justify the slower increase rate at high electrolyte concentrations.

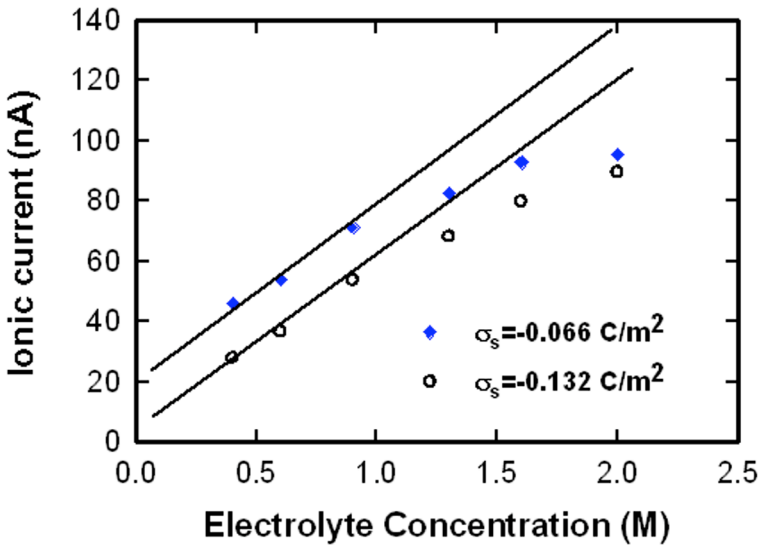

Figure 5.4 The MD simulation result of ionic current as a function of electrolyte concentration. The current is seen to deviate from linear bulk behavior at electrolyte concentrations above 1 M. The electrolyte composition was KCl. (Ge et al. 2009)

The experimental data of ionic conductance at an electrolyte concentration of above 1 M in figure 5.3 (a) and (b), however, demonstrates a linear concentration dependence opposing the MD simulation result. There could be two likely possibilities for this behavior

- The pore size specified by the vendor could be inaccurate or the non-uniform pore size or large tortuosity could have unknown effects on the ionic conductance.
- The surface charge density of the porous glass membrane could be significantly lower than expected.

The pore size of 4 nm for the porous glass membranes as specified by the vendor is an average value and therefore a very likely possibility is that pores with a diameter larger than 4 nm could dominate the ion transport through the membrane. For example, ionic current through a 10 nm diameter pore will be 25 times that of a 2 nm diameter pore. The ionic conductance in such a membrane at high electrolyte concentrations might then be significantly influenced by the several larger diameter pores. The deviation from linear behavior, as stated by Ge *et al*., is truly a nano scale phenomenon requiring that the total number of ions in the EDL be comparable to that outside the EDL. Therefore, for nanochannels of the size on the order of 10 nm, a linear trend as seen in figure 5.3 (a) and (b) will be observed. This however is not true according to Thomas Elmer, a former employee of Corning Inc. He published an article in the Engineered Materials Handbook on porous and reconstructed glasses wherein he studied the pore size distribution in these membranes and concluded that the distribution is generally very narrow with about 96% of the pores falling within ± 0.3 nm from the average radius (Elmer 1992). Figure 5.5

shows the pore size distribution of porous glass membrane having an average pore diameter of 4 nm. However, without the ability to carefully characterize the porous material to obtain the average pore size and uniformity, we cannot totally rule out this possibility at the moment.

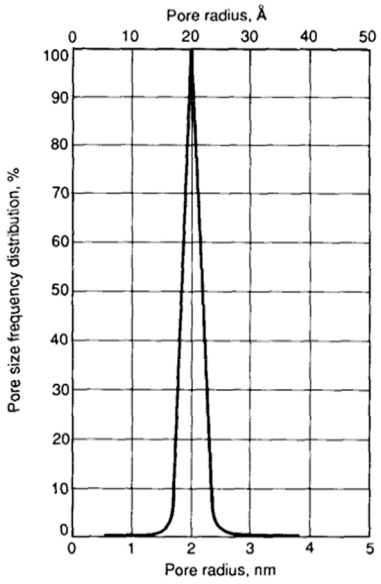

Figure 5.5 Pore size distribution of a porous glass membrane with an average pore diameter of 4 nm. (Elmer 1992)

Another possibility for the observed linear behavior is that the surface charge density of the nanoporous membrane is much lower than that in the simulation (the lowest one is 0.06 C/m^2). To get an estimate of surface charge density for the porous glass membranes, their zeta potential was calculated with each of the two electrolytes at a concentration of 100 mM. To achieve this, an EO pumping experiment was conducted, the procedure for which was identical to that followed for the PAA membranes in Chapter III and hence will not be discussed in detail here. A flowrate of 1.4×10^{-3} ml/min

and 2.4×10^{-3} ml/min for NaCl and KCl, respectively was measured for an electric field of 0.02 V/μm across the membrane. Making use of equation (3.2) and inserting the flowrate values in it the zeta potential of the membranes can be calculated. The porosity of the membranes was determined experimentally from the wet and dry weights, wt_{wet} and wt_{dry}, of the membrane and using the equation (Zeng et al. 2001)

$$\varphi = \frac{wt_{wet} - wt_{dry}}{\rho AL}, \tag{5.1}$$

where ρ is the density of water. The porosity was measured to be around 25% using this method, which was close to the value of 28% specified by the vendor. The tortuosity of the pores was calculated using the Slawinski equation, which is given as (Slawinski 1926)

$$\tau = \frac{1}{(1.3219 - 0.3219\varphi)^2}. \tag{5.2}$$

The tortuosity was estimated to be about 65% indicating that the pores in the porous glass membrane are not perfectly parallel to each other as in the PAA membranes [Here tortuosity is defined as (L/L_e)] . Using these numbers and a value of 0.4 for f in equation (3.2) to account for the EDL thickness effects within a nanochannel (Yao and Santiago 2003), the zeta potential value for the porous glass membrane was measured to be around -3.25 mV and -5.57 mV for NaCl and KCl respectively. These values are far below the zeta potential of glass which is on the order of -100 mV. The equivalent surface charge density can be evaluated using the Gouy equation, which relates the surface charge density to the zeta potential, and is given as (Nollet 2004)

$$\sigma_s = \frac{\sqrt{C}}{A} Sinh\left[\frac{ze\zeta}{2kT}\right], \tag{5.3}$$

where

$$A = \frac{1}{\sqrt{8N_A \varepsilon \varepsilon_0 kT}}. \tag{5.4}$$

Here N_A is the Avogadro's number, k is the Boltzmann's constant, T is the temperature in Kelvin, C is the solution concentration, z is the ion valence, e is the elementary unit charge and σ_s is the surface charge density. The respective surface charge density values for NaCl and KCl solutions then come out to be -2.34 x 10^{-3} C/m^2 and -4.01 x 10^{-3} C/m^2. These values are very low for glass whose surface charge density is about 0.1 C/m^2. It should be noted here that the two electrolytes used for this experiment were not buffered solutions and therefore the pH of these solutions will not stay constant on application of a bias during pumping. Since the zeta potential is a strong function of solution pH, it will therefore fluctuate during pumping and hence the values calculated above are not precise and contain a certain amount of uncertainty in them. The extremely low values, however, do indicate that the zeta potential and hence the surface charge density of the porous glass membranes is on the lower side than should be expected. A very possible reason for this could be the fact that these membranes have been used as organic getters, which means that they have a strong tendency to adsorb organic molecules from the atmosphere (Elmer 1992). Such adsorption would render the pore surface to exhibit a lower surface charge density, contrary to the assumption made in the MD simulation study for the 3 nm pore and thus explaining the linear trend of ionic conductance obtained in figure 5.3 (a) and (b) above 1 M electrolyte concentration.

5.4 Summary

In summary this chapter lays focus on ionic conductance measurements of nanoporous glass membranes at high electrolyte concentrations, motivated by a recent MD simulation disclosing some novel non-linear ion transport phenomena in nanometer scale pores at high electrolyte concentrations. The membranes have an average pore diameter of 4 nm. Though these measurements were conducted for a concentration range of 5 mM to 2 M, the conductance values at higher electrolyte concentrations – above 1 M were of particular interest to compare with the MD simulation results. The experimental data however indicated no such trend of non-linear conductance between 1 M and 2 M electrolyte concentration. Based on measurements of EO pumping flowrate, a theoretical analysis revealed a low surface charge density for the porous glass membrane, most likely due to adsorption of organic molecules over its surface, which could be the reason for the observed linear concentration dependence.

CHAPTER VI

CONCLUSIONS AND FUTURE WORK

This dissertation presents experimental characterization of electro-osmostic pumping using novel micro- and nanoporous materials and field effect flow control on them. In addition, ionic transport through these novel micro- and nanoporous materials have been measured and discussed. Three different porous membranes, SiO_2-coated porous alumina membranes, SiN_x-coated porous silicon membranes, and nanoporous glass membranes, were implemented and tested. Following are the concluding remarks and future work directions for the research carried out on each of the three membranes.

A nano structured, SiO_2-coated PAA membrane has been successfully fabricated utilizing the electrochemical anodization technique and sol-gel conformal coating. Furthermore it was demonstrated that this membrane could be used for EO pumping to achieve record-high flowrates – much greater than those reported in literature, at a low effective applied voltage across the membrane. This can be attributed to the dense array of highly ordered parallel nanopores of the PAA membrane resulting in a high porosity and a tortuosity of unity. The pump performance was characterized experimentally on the basis of flowrate with the maximum normalized flowrate of 0.125 ml/min/V/cm^2 based on the effective voltage for a 2.5 mM buffer solution. Although it is comparable to that reported for the porous silicon EO pump, the low operation voltage and cost-effective fabrication makes the SiO_2-coated PAA membrane more attractive for EO pumping applications. These membranes hold a significant promise for the future and subsequent

work should be directed towards developing a complete microelectronic cooling system incorporating these membranes.

At low concentration buffer solutions, double layer effects were observed to influence the EO flowrate. A decrease in the flowrate was observed at these concentrations due to the comparable double layer thickness and the channel diameter, resulting in a change in the velocity profile within the nanopore. Furthermore at these low concentrations the ionic conductance through these nanopores deviates from its bulk value, because of overlapped EDLs. Additionally uncoated PAA membranes were tested for EO pumping. The pumping flowrate was found to be lower than that of the SiO_2-coated membranes. More interestingly, an unusual trend was observed for buffer concentrations ≤ 2.5 mM and an effective applied field > 0.03 V/μm. The flowrate does not follow the expected linear trend, but follows a non-monotonic increase-decrease profile as the electric field increases, which cannot be explained with the current available information.

Field effect flow control on a porous membrane has been demonstrated with a laboratory-fabricated SiN_x coated porous silicon membrane. A heavily doped silicon within the membrane core functioned as the gate electrode, analogous to a MOSFET, whereas SiN_x conformally deposited over the entire membrane carried out the function of the gate dielectric. An enhancement of EO flow velocity by approximately 15% was observed on the application of -45 V gate bias for a pH 3.6 buffer solution. On reversing the polarity of gate bias to +40 V, a 70% reduction was noted for the same buffer solution. This discrepancy in enhancement-reduction of EO flow velocity has been attributed to electrolytic rectification effect. Whilst electrolytic rectification has been

studied and documented for SiO_2 based EIS systems, this work brings forth the occurrence of this effect in a SiN_x based EIS system for the first time. As a consequence, the rectification effect causes a leakage current to flow through the insulating SiN_x channel wall when the silicon is biased negative with respect to the buffer solution whereas no leakage current was observed on reversing the bias polarity. The leakage current results in hydrogen being evolved at the SiN_x/buffer solution interface, which is responsible for the reduced gating effects under negative gate bias.

Although the expected increase in EO flow velocity through field effect was not highlighted in this work, this research brings to light the occurrence of electrolytic rectification in SiN_x. Though the reasoning behind the rectification effect in SiN_x is not fully confirmed, this work opens up an avenue for researching this dielectric material further from the standpoint of hydrogen diffusion and electron transport through it – especially when SiN_x is in contact with an aqueous solution and under bias. Therefore, future efforts should be put in this direction. Subsequent efforts should also be put in determining the energy level of the hydrogen impurity band that this dissertation hints at being present within the nitride film.

The last section of the dissertation presents the experimental work done on a nanoporous glass membrane to study the ionic conductance of nanochannels at high electrolyte concentrations. The porous membranes in this instance were purchased commercially. This study was stimulated from an MD simulation highlighting a novel effect wherein the ionic current through a 3 nm diameter nanopore with a high surface charge density was observed to deviate from linear behavior at high electrolyte concentrations (> 1 M). The nanoporous glass membranes with an average pore diameter

of 4 nm seemed an ideal choice for proving this effect experimentally since the conductance values were much higher in this case than single nanochannels/pores and therefore less error prone. However the results indicated a linear trend of ionic conductance at electrolyte concentrations between 1 M and 2 M for both NaCl and KCl electrolyte solutions. A theoretical analysis based on EO pumping measurements indicated that the zeta potential of the porous glass membranes could be much lower than that expected for a glass surface, which translates into a very low surface charge density for these membranes. This has been attributed to the fact that these membranes function as organic getters and have a tendency to adsorb organic molecules from the atmosphere, which most likely reduces the surface charge density of these membranes.

REFERENCES

Arulanandam, S. and Li, D. Q. (2000), 'Liquid transport in rectangular microchannels by electroosmotic pumping', *Colloids and Surfaces a-Physicochemical and Engineering Aspects,* 161 (1), 89-102.

Asoh, H., et al. (2001), 'Conditions for fabrication of ideally ordered anodic porous alumina using pretextured Al', *Journal of the Electrochemical Society,* 148 (4), B152-B56.

Ayon, A. A., et al. (1999a), 'Influence of Coil Power on the Etching Characteristics in a High Density Plasma Etcher', *Journal of the Electrochemical Society,* 146 (7), 2730-36.

Ayon, A. A., et al. (1999b), 'Characterization of a Time Multiplexed Inductively Coupled Plasma Etcher', *Journal of the Electrochemical Society,* 146 (1), 339-49.

Bard, A. J. and Faulkner, L. R. (1980), *Electrochemical Methods* (New York: John Wiley & Sons).

Belyi, V. I., et al. (1976), 'Chemical non-uniformity of thin dielectric films produced by ammonolysis of monosilane', *Thin Solid Films,* 37 (2), L39-L42.

Bengough, G. B. and Stuart, J. M. (1923), 'Producing an oxide film by the chromic acid process and dyeing it by immersion in dyestuff solution', (223,994; United Kingdom).

Bhave, R. R. (1991), *Inorganic membranes synthesis, characteristics, and applications* (New York: Van Nostrand Reinhold) xx, 312 p.

Bousse, L. and Mostarshed, S. (1991), 'The zeta-potential of silicon-nitride thin-films', *Journal of Electroanalytical Chemistry,* 302 (1-2), 269-74.

Brown, W. D. and Khaliq, M. A. 'Silicon nitride for application as the gate dielectric in MOS devices', (USA: The University of Arkansas (Little Rock, AR)).

Bu, K. H. and Moudgil, B. M. (2007), 'Selective chemical mechanical polishing using surfactants', *Journal of the Electrochemical Society,* 154 (7), H631-H35.

Buch, J. S., et al. (2001), 'Field-effect flow control in a polydimethylsiloxane-based microfluidic system', *Electrophoresis,* 22 (18), 3902-07.

Buchanan, D. A. (1999), 'Scaling the gate dielectric: Materials, integration, and reliability', *IBM Journal of Research and Development,* 43 (3), 245-64.

Chang, H., et al. (2004), 'DNA-Mediated Fluctuations in Ionic Current through Silicon Oxide Nanopore Channels', *Nano Letters,* 4 (8), 1551-56.

Chen, C. H. and Santiago, J. G. (2002), 'A planar electroosmotic micropump', *Journal of Microelectromechanical Systems,* 11 (6), 672-83.

Chen, K., et al. (1993), 'Effect of total hydrogen content in silicon nitride sensitive film on performance of ISFET', *Sensors and Actuators B: Chemical,* 12 (1), 23-27.

Chen, W., Yuan, J. H., and Xia, X. H. (2005a), 'Characterization and manipulation of the electroosmotic flow in porous anodic alumina membranes', *Analytical Chemistry,* 77 (24), 8102-08.

Chen, Z., Wang, P., and Chang, H. C. (2005b), 'An electro-osmotic micro-pump based on monolithic silica for micro-flow analyses and electro-sprays', *Analytical and Bioanalytical Chemistry,* 382 (3), 817-24.

Csokán, P. and Sc, C. C. (1962), 'Hard anodizing: Studies of the relation between anodizing conditions and the growth and properties of hard anodic oxide coatings.', *Electroplat. Metal Finish. ,* 15, 75-82.

Csokán, P. (1961), 'Beiträge zur kenntnis der anodischen oxydation von aluminium verdunnter, kalter schwefelsaure.', *Metalloberfläche,* 15, B49-B53.

Csokán, P. (1964), 'Some observations on the growth mechanism of hard anodic oxide coatings on aluminium. ', *Transactions of the Institute of Metal Finishing,* 41, 51-56.

Daiguji, H., Yang, P. D., and Majumdar, A. (2004), 'Ion transport in nanofluidic channels', *Nano Letters,* 4 (1), 137-42.

Depas, M., Nigam, T., and Heyns, M. M. (1996), 'Soft breakdown of ultra-thin gate oxide layers', *Electron Devices, IEEE Transactions on,* 43 (9), 1499-504.

Diggle, J. W., Downie, T. C., and Goulding, C. W. (1969), 'Anodic oxide films on aluminum', *Chemical Reviews,* 69 (3), 365-405.

DiMaria, D. J. (1978), 'Defects and Impurities in Thermal SiO2', in S. T. Pantelides (ed.), *Physics of SiO2 and its Interfaces* (New York: Pergamon Press).

Doshi, V. N., Niuya, T., and Yang, M. (2001), 'Silicon nitride dopant diffusion barrier in integrated circuits', (United States: Texas Instruments Incorporated (Dallas, TX)).

Elmer, T. H. (1992), *Porous and Reconstructed Glasses* (Engineered Materials Handbook, 4; Ohio: ASM International) 427-32.

Fain, D. E. (1994), 'Membrane gas separation principles', *MRS Bulletin,* 19 (4), 40-43.

Feng, Z. C. and Tsu, R. (1994), *Porous Silicon* (World Scientific) 465.

Fintschenko, Y. and van den Berg, A. (1998), 'Silicon microtechnology and microstructures in separation science', *Journal of Chromatography A,* 819 (1-2), 3-12.

Föll, H. (1991), 'Properties of silicon-electrolyte junctions and their application to silicon characterization', *Applied Physics A: Materials Science & Processing,* 53 (1), 8-19.

Gan, W. E., et al. (2000), 'Mechanism of porous core electroosmotic pump flow injection system and its application to determination of chromium(VI) in waste-water', *Talanta,* 51 (4), 667-75.

Ge, Y., et al. (2009), 'Ionic current through a nanopore three nanometers in diameter', *submitted to Journal of Applied Physics*.

Ghowsi, K. and Gale, R. J. (1991), 'Field-effect electroosmosis', *Journal of Chromatography,* 559 (1-2), 95-101.

Guenat, O. T., et al. (2001), 'Partial electroosmotic pumping in complex capillary systems - Part 2: Fabrication and application of a micro total analysis system (mu TAS) suited for continuous volumetric nanotitrations', *Sensors and Actuators B-Chemical,* 72 (3), 273-82.

Hayes, M. A. and Ewing, A. G. (1992), 'Electroosmotic flow-control and monitoring with an applied radial voltage for capillary zone electrophoresis', *Analytical Chemistry,* 64 (5), 512-16.

Hayes, M. A., Kheterpal, I., and Ewing, A. G. (1993a), 'Effects of buffer ph on electroosmotic flow-control by an applied radial voltage for capillary zone electrophoresis', *Analytical Chemistry,* 65 (1), 27-31.

Hayes, M. A., Kheterpal, I., and Ewing, A. G. (1993b), 'Electroosmotic flow-control and surface conductance in capillary zone electrophoresis', *Analytical Chemistry,* 65 (15), 2010-13.

Hecker, J. G. (1988), 'Aluminum hard coats.', *Product Finishing,* 53, 88-92.

Hedrick, J. L., et al. (1998), 'Templating nanoporosity in thin-film dielectric insulators', *Advanced Materials,* 10 (13), 1049-+.

Hegde, S. and Babu, S. V. (2004), 'Study of surface charge effects on oxide and nitride planarization using alumina/ceria mixed abrasive slurries', *Electrochemical and Solid State Letters,* 7 (12), G316-G18.

Helmholtz, H. (1879), 'Studien über electrische Grenzschichten', *Annalen der Physik,* 243 (7), 337.

Henriquez, R. R., et al. (2004), 'The resurgence of Coulter counting for analyzing nanoscale objects', *Analyst,* 129, 478-82.

Hjerten, S. (1985), 'High-performance electrophoresis - elimination of electroendosmosis and solute adsorption', *Journal of Chromatography,* 347 (2), 191-98.

Huang, T. L., et al. (1993), 'Mechanistic studies of electroosmotic control at the capillary solution interface', *Analytical Chemistry,* 65 (20), 2887-93.

Hubbell, J. A.; Langer, R. (1995), *Chem.Eng.News*, 42.

Hunter, M. S. and Fowle, P. (1954), 'Determination of Barrier Layer Thickness of Anodic Oxide Coatings', *Journal of the Electrochemical Society,* 101 (9), 481-85.

Hunter, R. J. (1981), *Zeta Potential in Colloidal Science: Principles and Applications* (London: Academic Press).

IBM (2008), *Made in IBM Labs: IBM Cools 3-D Chips with H2O* (Zurich, Switzerland).

Izumi, A., Sato, H., and Matsumura, H. (2001), 'Formation of high moisture and dopant diffusion resistivity silicon nitride films by catalytic-CVD method', *Journal de Physique IV,* 11, 901-06.

Jacobson, S. C., et al. (1994), 'Open channel electrochromatography on a microchip', *Analytical Chemistry,* 66 (14), 2369-73.

Jessensky, O., Muller, F., and Gosele, U. (1998), 'Self-organized formation of hexagonal pore arrays in anodic alumina', *Applied Physics Letters,* 72 (10), 1173-75.

Jiang, L. N., et al. (2002), 'Closed-loop electroosmotic microchannel cooling system for VLSI circuits', *Ieee Transactions on Components and Packaging Technologies,* 25 (3), 347-55.

Joannopoulos, J. D., Villeneuve, P. R., and Fan, S. H. (1997), 'Photonic crystals: Putting a new twist on light', *Nature,* 386 (6621), 143-49.

John, S., Balasubramanian, V. , and Shenoi, B. A. (1984), 'Hard anodizing aluminium and its alloys—AC in sulphuric acid—sodium sulphate bath.', *Met. Finish.,* 82, 33-39.

Jorgenson, J. W. and Lukacs, K. D. (1983), 'Capillary zone electrophoresis', *Science,* 222 (4621), 266-72.

Kang, Y. and Jorne, J. (1993), 'Porous silicon formation: Morphological stability analysis', *Applied Physics Letters,* 62 (18), 2224-26.

Karnik, R., et al. (2005), 'Electrostatic control of ions and molecules in nanofluidic transistors', *Nano Letters,* 5 (5), 943-48.

Kasianowicz, J. J., et al. (1996), 'Characterization of individual polynucleotide molecules using a membrane channel', *Proceedings of the National Academy of Sciences of the United States of America,* 93 (24), 13770-73.

Keizer, K. and Verweij, H. (1996), 'Progress in inorganic membranes', *Chemtech,* 26 (1), 37-41.

Keller, F., Hunter, M. S., and Robinson, D. L. (1953), 'Structural Features of Oxide Coatings on Aluminum', *Journal of the Electrochemical Society,* 100 (9), 411-19.

Kirby, B. J. and Hasselbrink, E. F. (2004), 'Zeta potential of microfluidic substrates: 1. Theory, experimental techniques, and effects on separations', *Electrophoresis,* 25 (2), 187-202.

Kovtyukhova, N. I., Mallouk, T. E., and Mayer, T. S. (2003), 'Templated surface sol-gel synthesis of SiO2 nanotubes and SiO2-insulated metal nanowires', *Advanced Materials,* 15 (10), 780-85.

Kovtyukhova, N. L. and Mallouk, T. E. (2005), 'Nanowire p-n heterojunction diodes made by templated assembly of multilayer carbon-nanotube/polymer/semiconductor-particle shells around metal nanowires', *Advanced Materials,* 17 (2), 187-+.

Kyotani, T., Tsai, L. F., and Tomita, A. (1996), 'Preparation of ultrafine carbon tubes in nanochannels of an anodic aluminum oxide film', *Chemistry of Materials,* 8 (8), 2109-13.

Laermer, F. and Schilp, A. (1996), 'Method of Anistropically Etching Silicon', (Germany: Robert Bosch GmBH).

Lakes, R. (1987), 'Foam Structures with a Negative Poissons Ratio', *Science,* 235 (4792), 1038-40.

Lambert, W. J. and Middleton, D. L. (1990), 'pH hysteresis effect with silica capillaries in capillary zone electrophoresis', *Analytical Chemistry,* 62 (15), 1585-87.

Laser, D. J. and Santiago, J. G. (2004), 'A review of micropumps', *Journal of Micromechanics and Microengineering,* 14 (6), R35-R64.

Laser, D. J., et al. (2001), 'A low-voltage silicon micromachined parallel-plate electrokinetic pump', *Proceedings of the 11th International Conference on Solid-State Sensors and Actuators* (Munich, Germany).

Laser, D. J., et al. (2003), *Proceedings of the 12th International Conference on Solid-State Sensors, Actuators and Microsystems* (Boston, USA).

Lee, C. S., Blanchard, W. C., and Wu, C. T. (1990), 'Direct control of the electroosmosis in capillary zone electrophoresis by using an external electric-field', *Analytical Chemistry,* 62 (14), 1550-52.

Lee, C. S., et al. (1991), 'Factors affecting direct control of electroosmosis using an external electric-field in capillary electrophoresis', *Analytical Chemistry,* 63 (15), 1519-23.

Lee, C. Y., et al. (2004), 'Electrokinetically driven active micro-mixers utilizing zeta potential variation induced by field effect', *Journal of Micromechanics and Microengineering,* 14 (10), 1390-98.

Lee, S. B., et al. (2002), 'Antibody-based bio-nanotube membranes for enantiomeric drug separations', *Science,* 296 (5576), 2198-200.

Lee, W., et al. (2006), 'Fast fabrication of long-range ordered porous alumina membranes by hard anodization', *Nature Materials,* 5 (9), 741-47.

Lehmann, V. (1993), 'The Physics of Macropore Formation in Low Doped n-Type Silicon', *Journal of the Electrochemical Society,* 140 (10), 2836-43.

Lehmann, V. and Föll, H. (1990), 'Formation Mechanism and Properties of Electrochemically Etched Trenches in n-Type Silicon', *Journal of the Electrochemical Society,* 137 (2), 653-59.

Lehmann, V. and Gosele, U. (1991), 'Porous silicon formation: A quantum wire effect', *Applied Physics Letters,* 58 (8), 856-58.

Lehmann, V. and Ronnebeck, S. (1999), 'The Physics of Macropore Formation in Low-Doped p-Type Silicon', *Journal of the Electrochemical Society,* 146 (8), 2968-75.

Levitz, P., et al. (1991), 'Porous vycor glass: The microstructure as probed by electron microscopy, direct energy transfer, small-angle scattering, and molecular adsorption', *The Journal of Chemical Physics,* 95 (8), 6151-61.

Li, A. P., et al. (1998), 'Hexagonal pore arrays with a 50-420 nm interpore distance formed by self-organization in anodic alumina', *Journal of Applied Physics,* 84 (11), 6023-26.

Li, A. P., et al. (1999), 'Polycrystalline nanopore arrays with hexagonal ordering on aluminum', *Journal of Vacuum Science & Technology a-Vacuum Surfaces and Films,* 17 (4), 1428-31.

Li, D. Q. (2004), *Electrokinetics in Microfluidics*, ed. A. Hubbard (Interface Science and Technology, 2; London: Academic Press).

Li, J., et al. (2001), 'Ion-beam sculpting at nanometre length scales', *Nature,* 412 (6843), 166-69.

Lichtenberger-Bajza, E., Domony, A., and Csokán, P. (1960), 'Untersuchung der struktur und anderer eigenschaften von durch anodische oxydation auf aluminium erzeugten hartoxydschichten.', *Werkstoffe. Korros.,* 11, 701-07.

Lin, V. S. Y., et al. (1997), 'A porous silicon-based optical interferometric biosensor', *Science,* 278 (5339), 840-43.

Zhi, L., et al. (2005), 'Carbonization of Disclike Molecules in Porous Alumina Membranes: Toward Carbon Nanotubes with Controlled Graphene-Layer Orientation13', *Angewandte Chemie International Edition,* 44 (14), 2120-23.

Lohrengel, M. M. (1993), 'Thin anodic oxide layers on aluminium and other valve metals: high field regime', *Materials Science and Engineering: R: Reports,* 11 (6), 243-94.

Ma, T. P. (1998), 'Making silicon nitride film a viable gate dielectric', *IEEE Transactions on Electron Devices,* 45 (3), 680-90.

MacNair, J. E., Lewis, K. C., and Jorgenson, J. W. (1997), 'Ultrahigh pressure reversed-phase liquid chromatography in packed capillary columns', *Analytical Chemistry,* 69 (6), 983-89.

Madou, M. J. (2002), *Fundamentals of Microfabrication-The Science of Miniaturization* (2nd ed. edn.; Boca Raton, Florida: CRC Press).

Madou, M. J., Frese, K. W., and Morrison, S. R. (1979), 'Electron Exchange at the Surface of Thermally Grown Silica', *Journal of the Electrochemical Society,* 126 (10), 1827-28.

Madou, M. J., Frese, K. W., and Morrison, S. R. (1980), 'Silicon-Silica Electrode', *Physica Status Solidi a-Applied Research,* 57 (2), 705-12.

Maluf, N. (1999), *An Introduction to Microelectromechanical Systems Engineering* (Second edn.; Boston: Artech House Publishers) 265.

Masuda, H. and Fukuda, K. (1995), 'Ordered metal nanohole arrays made by a 2-step replication of honeycomb structures of anodic alumina', *Science,* 268 (5216), 1466-68.

Masuda, H. and Satoh, M. (1996), 'Fabrication of gold nanodot array using anodic porous alumina as an evaporation mask', *Japanese Journal of Applied Physics,* 35, L126-L29.

Masuda, H., Hasegawa, F., and Ono, S. (1997), 'Self-ordering of cell arrangement of anodic porous alumina formed in sulfuric acid solution', *Journal of the Electrochemical Society,* 144 (5), L127-L30.

Mazur, P. and Overbeek, J. T. G. (1951), 'On electroosmosis and streaming potentials in diaphragms', *Rec. Trav. Chim.,* 70, 83.

McCormick, R. M. (1988), 'Capillary zone electrophoretic separation of peptides and proteins using low pH buffers in modified silica capillaries', *Analytical Chemistry,* 60 (21), 2322-28.

McKnight, T. E., et al. (2001), 'Electroosmotically induced hydraulic pumping with integrated electrodes on microfluidic devices', *Analytical Chemistry,* 73 (16), 4045-49.

Mikulskas, I., et al. (2001), 'Aluminum oxide photonic crystals grown by a new hybrid method', *Advanced Materials,* 13 (20), 1574-+.

Morrison, S. R. (1980), *Electrochemistry at Semiconductor and Oxidized Metal Electrodes* (New York: Plenum Press).

Nielsch, K., et al. (2002), 'Self-ordering regimes of porous alumina: The 10% porosity rule', *Nano Letters,* 2 (7), 677-80.

Nollet, L. M. L. (2004), *Handbook of food analysis*, ed. L. M. L. Nollet (2 edn., 3: CRC Press) 2226.

Olbertz, B. (1988), 'Hartanodisieren eröffnet aluminum vielfältige technische Anwendungs-möglichkeiten.', *Aluminium,* 3, 268-70.

Ono, S., et al. (2004), 'Controlling Factor of Self-Ordering of Anodic Porous Alumina', *Journal of the Electrochemical Society,* 151 (8), B473-B78.

Papirer, E. (2000), *Adsorption on Silica Surfaces*, ed. A. T. Hubbard (Surfactant Science Series, 90; New York: Marcel Dekker, Inc.).

Park, S., et al. (2004), 'Self-assembly of mesoscopic metal-polymer amphiphiles', *Science,* 303 (5656), 348-51.

Parkhutik, V. P. and Shershulsky, V. I. (1992), 'Theoretical modeling of porous oxide-growth on aluminum', *Journal of Physics D-Applied Physics,* 25 (8), 1258-63.

Paul, P. H. and Rakestraw, D. J. (2000), 'Electrokinetic high-pressure hydraulic system', (United States).

Paul, P. H., et al. (2001), 'Electrokinetic high-pressure hydraulic system', (United States).

Polson, N. A. and Hayes, M. A. (2000), 'Electroosmotic flow control of fluids on a capillary electrophoresis microdevice using an applied external voltage', *Analytical Chemistry,* 72 (5), 1088-92.

Poppe, H., Cifuentes, A., and Kok, W. T. (1996), 'Theoretical description of the influence of external radial fields on the electroosmotic flow in capillary electrophoresis', *Analytical Chemistry,* 68 (5), 888-93.

Prakash, S. S., et al. (1995), 'Silica aerogel films prepared at ambient-pressure by using surface derivatization to induce reversible drying shrinkage', *Nature,* 374 (6521), 439-43.

Pretorius, V., Hopkins, B. J., and Schieke, J. D. (1974), 'Electroosmosis-a new concept for high speed liquid chromatography', *Journal of Chromatography,* 99, 23.

Qiao, R. and Aluru, N. R. (2005), 'Scaling of electrokinetic transport in nanometer channels', *Langmuir,* 21 (19), 8972-77.

Quincke, G. (1861), 'Uber die fortführung materieller teilchen durch strömende electricität', *Annalen der Physik,* 189 (8), 513.

Rajendra, A., et al. (2005), 'Hard anodization of aluminium and its application to sensorics.', *Surface Engineering,* 21 (3), 193-97.

Ramsden, E. N. (2000), *A-level Chemistry: Core Text* (Nelson Thornes).

Ramsey, R. S. and Ramsey, J. M. (1997), 'Generating electrospray from microchip devices using electroosmotic pumping', *Analytical Chemistry,* 69 (6), 1174-78.

Reuss, F. F. (1809), 'Sur un nouvel effet de l'électricité galvanique', *Memoires de la Societe Imperiale des Naturalistes de Moscou,* 2, 327.

Rice, C. L. and Whitehead, R. (1965), 'Electrokinetic flow in a narrow cylindrical capillary', *Journal of Physical Chemistry,* 69 (11), 4017-24.

Hurst, S. J., et al. (2006), 'Multisegmented One-Dimensional Nanorods Prepared by Hard-Template Synthetic Methods', *Angewandte Chemie International Edition,* 45 (17), 2672-92.

Scales, P. J., et al. (1992), 'Electrokinetics of the silica solution interface - a flat-plate streaming potential study', *Langmuir,* 8 (3), 965-74.

Schasfoort, R. B. M., et al. (1999), 'Field-effect flow control for microfabricated fluidic networks', *Science,* 286 (5441), 942-45.

Schoch, R. B. and Renaud, P. (2005), 'Ion transport through nanoslits dominated by the effective surface charge', *Applied Physics Letters,* 86 (25), 253111-3.

Schwer, C. and Kenndler, E. (1991), 'Electrophoresis in fused-silica capillaries - the influence of organic-solvents on the electroosmotic velocity and the zeta-potential', *Analytical Chemistry,* 63 (17), 1801-07.

Slawinski, A. (1926), *J. Chim. Phys.,* 23, 710-27.

Smeets, R. M. M., et al. (2005), 'Salt Dependence of Ion Transport and DNA Translocation through Solid-State Nanopores', *Nano Letters,* 6 (1), 89-95.

Smith, R. L. and Collins, S. D. (1992), 'Porous silicon formation mechanisms', *Journal of Applied Physics,* 71 (8), R1-R22.

Smoluchowski, M. (1905), *Phys. Z.,* 6, 529.

Sprycha, R. (1989), 'Electrical double-layer at alumina/electrolyte interface: 1. Surface-charge and zeta potential', *Journal of Colloid and Interface Science,* 127 (1), 1-11.

Stein, D., Kruithof, M., and Dekker, C. (2004), 'Surface-charge-governed ion transport in nanofluidic channels', *Physical Review Letters,* 93 (3).

Sulka, G. D., et al. (2002), 'Synthesis of well-ordered nanopores by anodizing aluminum foils in sulfuric acid', *Journal of the Electrochemical Society,* 149 (7), D97-D103.

Sun, J., et al. (2008), 'Experimental Characterization of Electrical Current Leakage in PDMS Microfluidic Devices', *Microfluidics and Nanofluidics*.

Theeuwes, F. (1975a), 'Electroosmotic pump and fluid dispenser including same', (United States).

Theeuwes, F. (1975b), 'Elementary osmotic pump', *Journal of Pharmaceutical Science,* 64 (12), 1987.

Thompson, G. E. and Wood, G. C. (1981), 'Porous Anodic Film Formation on Aluminum', *Nature,* 290 (5803), 230-32.

Thompson, G. E., et al. (1978), 'Nucleation and growth of porous anodic films on aluminium', *Nature,* 272 (5652), 433-35.

Tripp, J. A., et al. (2004), 'High-pressure electroosmotic pumps based on porous polymer monoliths', *Sensors and Actuators B-Chemical,* 99 (1), 66-73.

Uhlir, A. (1956), 'Electrolytic shaping of germanium and silicon', *Bell Syst. Tech. J.,* 35, 333-47.

Vajandar, S. K., et al. (2007), 'SiO2-coated porous anodic alumina membranes for high flow rate electroosmotic pumping', *Nanotechnology,* 18 (27), 8.

van der Wouden, E. J., et al. (2005), 'Field-effect control of electro-osmotic flow in microfluidic networks', *Colloids and Surfaces a-Physicochemical and Engineering Aspects,* 267 (1-3), 110-16.

Vlasov, Y. G., Tarantov, Y. A., and Bobrov, P. V. (2003), 'Analytical characteristics and sensitivity mechanisms of electrolyte-insulator-semiconductor system-based chemical sensors - a critical review', *Analytical and Bioanalytical Chemistry,* 376 (6), 788-96.

Wang, P., Chen, Z., and Chang, H. (2006), 'A new electroosmotic pump based on silica monoliths', *Sensors and Actuators B,* 113, 500.

Wernick, S., Pinner, R., and Sheasby, P. G. (1987), *The surface treatment and finishing of aluminum and it's alloys*, 2 vols. (Fifth edn., 1: Finishing Publications Ltd.).

Wong, H. and Gritsenko, V. A. (2002), 'Defects in silicon oxynitride gate dielectric films', *Microelectronics Reliability,* 42 (4-5), 597-605.

Lee, W., et al. (2005), 'A Template-Based Electrochemical Method for the Synthesis of Multisegmented Metallic Nanotubes13', *Angewandte Chemie International Edition,* 44 (37), 6050-54.

Wood, G. C. and O'Sullivan, J. P. (1970), 'The anodizing of aluminium in sulphate solutions', *Electrochimica Acta,* 15 (12), 1865-76.

Wright, P. J. and Saraswat, K. C. (1989), 'The effect of fluorine in silicon dioxide gate dielectrics', *Electron Devices, IEEE Transactions on,* 36 (5), 879-89.

Wu, C. T., et al. (1992), 'Effect of direct control of electroosmosis on peptide and protein separations in capillary electrophoresis', *Analytical Chemistry,* 64 (8), 886-91.

Yao, S. H. and Santiago, J. G. (2003), 'Porous glass electroosmotic pumps: theory', *Journal of Colloid and Interface Science,* 268 (1), 133-42.

Yao, S. H., et al. (2003), 'Porous glass electroosmotic pumps: design and experiments', *Journal of Colloid and Interface Science,* 268 (1), 143-53.

Yao, S. H., et al. (2006), 'Electroosmotic pumps fabricated from porous silicon membranes', *Journal of Microelectromechanical Systems,* 15 (3), 717-28.

Yeo, Y. C., et al. (2000), 'Direct tunneling gate leakage current in transistors with ultrathin silicon nitride gate dielectric', *IEEE Electron Device Letters,* 21 (11), 540-42.

Yu, G. T. and Yen, S. K. (2002), 'Hydrogen ion diffusion coefficient of silicon nitride thin films', *Applied Surface Science,* 202 (1-2), 68-72.

Zeng, S. L., et al. (2001), 'Fabrication and characterization of electroosmotic micropumps', *Sensors and Actuators B-Chemical,* 79 (2-3), 107-14.

Zeng, S. L., et al. (2002), 'Electroosmotic flow pumps with polymer frits', *Sensors and Actuators B-Chemical,* 82 (2-3), 209-12.